Two- and three-dimensional nanocomposites containing noble metal nanoparticles functionalized with aminiothioalkyl ligands

Michalina Iwan

Ph.D. Thesis

Scientific supervisor: prof. Marcin Fiałkowski, DSc

This dissertation was prepared in the course of the International Doctorate Studies at the Institute of Physical Chemistry, Polish Academy of Sciences, ul. Kasprzaka 44/52, 01-224, Warsaw

Warsaw, August 2017

This work was supported by the project operated within the Foundation for Polish Science Team Programme co-financed by the EU "European Regional Development Fund" Grant No. TEAM/2010-6/4.

Dziękuję w szczególności

prof. IChF PAN. dr hab. Marcinowi Fiałkowskiemu,

Za nieocenione wsparcie merytoryczne, możliwość czerpania z niezwykle bogatej wiedzy i doświadczenia naukowego oraz stworzenie warunków sprzyjających rozwojowi naukowemu

dr Tomaszowi Andryszewskiemu,

za stworzenie przyjacielskiej atmosfery w pracy, sprawienie, że wykonywanie badań do pracy doktorskiej stało się fascynującą podróżą intelektualną, oraz za inspirujące, wielogodzinne dyskusje, naukowe i nie tylko :)

Dziękuję również **Pani Marzenie Wydryszek, Pani Patrycji Kalińskiej** oraz **Panu Jakubowi Sękowi** za pomoc w pracach laboratoryjnych

Tacie…
Który jest dla mnie inspiracją

Mamie,
Za nieustające wsparcie i wskazywanie właściwiej drogi w momentach zwątpienia

List of publications

Papers presented in this dissertation

1. **Michalina Iwan**, Tomasz Andryszewski, Marzena Wydryszek, and Marcin Fiałkowski *„Fabrication of nanocomposites by covalent bonding between noble nanoparticles and polymer matrix”,* **RSC Adv.,** *2015*, 5, 70127-70138.
2. Tomasz Andryszewski, **Michalina Iwan**, Marcin Hołdyński, and Marcin Fiałkowski *„Synthesis of a Free-Standing Monolayer of Covalently Bonded Gold Nanoparticles”*, **Chemistry of Materials**, *2016*, 28 (15), 5304-5313.

Other papers

1. Joanna Dolińska, Arunraj Chidambaram, Witold Adamkiewicz, Mehdi Estili, Wojciech Lisowski, **Michalina Iwan**, Barbara Palys, Ernst J. R. Sudholter, Frank Marken, Marcin Opallo, and Liza Rassaei *“Synthesis and characterization of porous carbon-MoS2 nanohybrid materials: electrocatalytic performance towards selected biomolecules”*, **Journal of Materials B**, *2016*, 4, 1448-1457.

Patents Granted

1. Tomasz Andryszewski, Michalina Iwan, Marzena Wydryszek, Marcin Fiałkowski, Robert Hołyst *„Sposób wytwarzania amoniowo-merkaptanowych ligandów i ich zastosowanie w funkcjonalizacji powierzchni nanocząstek metali, zwłaszcza złota”* **(P-402057)**, granted exclusive right no. 221220

Patent Applications

1. Tomasz Andryszewski, Michalina Iwan, Patrycja Kalińska, Marcin Fiałkowski, Robert Hołyst *„Spektrofotometryczny sposób oznaczania zawartości złota w roztworach, strukturach porowatych lub na powierzchni ciał stałych, zwłaszcza zawierających złote nanoobiekty”* **(P-409626)**
2. Tomasz Andryszewski, Michalina Iwan, Jakub Sęk, Marcin Fiałkowski, Robert Hołyst *„Sposób odzywskiwania złota z odpadów, zwłaszcza laboratoryjnych, oraz zastosowanie tego sposobu”* **(P-413843)**

3. Tomasz Andryszewski, Michalina Iwan, Marcin Fiałkowski „Nowa metoda wytwarzania usieciowanych monowarstw nanometalicznych (membran) na granicy faz ciecz-ciecz oraz stosowane w tym sposobie urządzenia do redukcji powierzchni granicy faz ciecz-ciecz” **(P-4116049)**

"I am among those who think that science has great beauty.
A Scientist in his laboratory is not only a mere technician:
he is also a child confronting natural phenomena
which impress him like a fairy tale."

- Maria Skłodowska – Curie

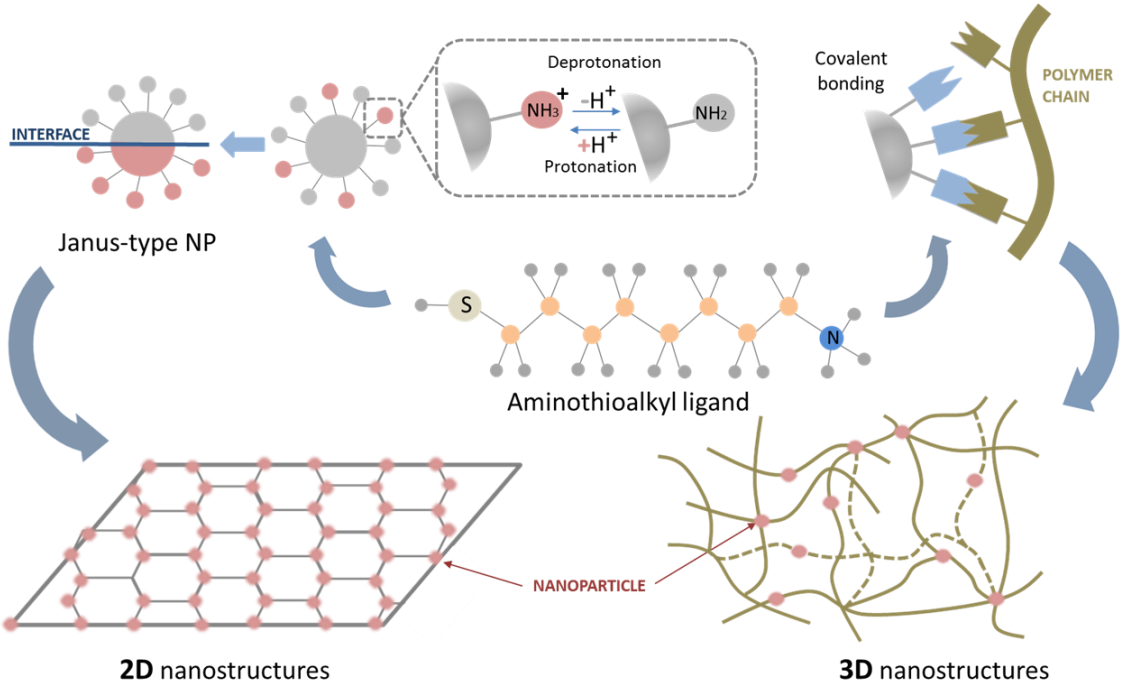

Table of Contents

List of abbreviations

0D – zero dimensional

1D – one dimensional

2D – two dimensional

3D – three dimensional

NP(s) – nanoparticle(s)

AuNP(s) – gold nanoparticle(s)

AgNP(s) – silver nanoparticle(s)

PtNP(s) – Platinum nanoparticle(s)

C4 – 4-mercaptobutan-1-aminium chloride

C8 – 8-mercaptooctan-1-aminium chloride

C12 – 12-mercaptododecan-1-aminium chloride

Au@C8 – gold nanoparticle functionalized wit 8-mercaptooctan-1-aminium chloride

Au@C12 – gold nanoparticle functionalized with 12-mercaptododecan-1-aminium chloride

Ag@C8 – silver nanoparticle functionalized with 8- mercaptooctan-1-aminium chloride

Pt@C8 – Platinum nanoparticle functionalized with 8-mercaptooctan-1-aminium chloride

CMC – carboxylmethylcelullose

PVA – polyvinyl alcohol

P[MA-co-S] – poly[maleic anhydride-co-styrene]

PVA – Au@C8 – PVA functionalized with gold nanoparticles coated with C8 ligand

PVA – C8 - PVA functionalized with C8 ligand

PVA – Pt@C8 - PVA functionalized with platinum nanoparticles coated with C8 ligand

AFM – Atomic Force Microscopy

DLS – Dynamic Light Scattering

FTIR – Fourier Transformation Infra-Red spectroscopy

IR – Infra-Red spectroscopy

NMR – Nuclear Magnetic Resonance Spectroscopy

SEM – Scanning Electron Microscopy

STEM – Scanning Transmission Electron Microscopy

TEM – Tunneling Electron Microscopy

UV-Vis – Ultraviolet Visible spectroscopy

LSP – localized surface plasmon

LSPR – localized surface plasmon resonance

ppm – parts per minion

rpm – rounds per minute

Research Background and Motivation

There has been a great deal of interest in the topic of nanoscale objects and their organization into ordered structures within the scientific community, since its conceptual origins often associated with Richard Feynman's lecture entitled "There's Plenty of Room at the Bottom". Nanosciences hold great promise for the synthesis of materials with unique properties. However, so far despite the large contribution of numerous research groups the full potential of nanotechnology and nanomaterials has not yet been fully exploited. Theoretical predictions concerning functional materials' properties and performance parameters still exceed significantly the results obtained in practice. This is caused either by preparation methods deficiencies or the lack thereof. Especially, the fabrication of highly organized, durable nanostructures and nanocomposites pose an important challenge. Widespread use of such materials requires the development of efficient and undemanding manufacture methods. Precise control of the synthetic procedure is imperative for the manipulation of the nanomaterial properties. As predicted, the occurrence of some unique properties is limited to a restricted variety of structure organizations. Thin films composed of nanoparticles (NPs) are an example of such structures. It has been predicted that films with a thickness of one nanoparticle's diameter will exhibit unusual characteristics. Large-scale commercialization of such materials demands not only impeccable functioning but, perhaps above all, profitable fabrication methods. The obtained materials must be characterized by considerable stability for their use to be economically justified. Such nanofilms, characterized by durability in air conditions are rare, whereas reports of free-standing, unsupported monolayer films are nonexistent. As can be seen improvement in the area of 2D and 3D nanocomposite synthesis is still needed. For these reasons I found this fascinating topic compelling and sought to contribute to this area of science during my research as a Ph.D. student.

THESES

- NPs functionalized with the aminothioalkyl ligand may be successfully used to obtain the first free-standing 2D monolayer film, where NPs are covalently cross-linked. The synthesis is carried out at the oil-water interface where the NPs form a monolayer.

- The interfacial synthesis of the 2D film is facilitated by the following three properties of the system: (1) The presence of charged amine groups in the aqueous phase prevents the tendency of NPs to aggregate at the interface. (2) The NPs are firmly anchored to the interface, impeding their escape into the bulk phases. (3) At the same time, the uncharged amine groups facing the oleic phase are reactive and can form chemical bonding with the linker molecules.

- The unique properties of the aminothioalkyl-coated NPs exhibited at the oil-water interface follow from their ability of protonation/deprotonation that is controlled by the pH of the aqueous phase. This allows for the formation of amphiphilic structures, the so-called “Janus” structures, upon reorganization of the ligands on the NP surface.

- The aminothioalkyl ligand provides NPs with the ability of spontaneous covalent bond formation with reactive functional groups of polymeric matrices, including the aldehyde, anhydride, carboxylic groups, and hydroxyl group provided oxidation to carbonyl derivatives occurs in the reaction conditions. This allows for the synthesis of durable 3D nanocomposites in which the NPs are covalently bound to the polymeric matrix.

Goal and Scope of the Dissertation

The goal of this dissertation is the development of synthetic platforms for fabrication of durable 2D nanocomposites with noble metal NPs strongly linked with each other, and 3D nanocomposite materials with metallic NPs chemically bound to a polymeric matrix. The 2D nanocomposite will consist of a single monolayer of NPs, chemically cross-linked via covalent bonds, forming a free-standing 2D nanofilm. This monolayer film should be durable in air conditions, and maintain its integrity even when unsupported. To achieve these goals, design of appropriate synthetic platforms, for both 2D and 3D nanocomposites, is required.

The liquid-liquid interface between two immiscible phases is investigated as a synthetic platform for the 2D film preparation. Utilization of this kind of platform for the fabrication of nanofilms requires establishment of optimal conditions leading to successful formation of a self-assembled NP monolayer at the liquid-liquid interface. The selection of best suited solvents to make up the biphasic system is a prime requirement. These solvents must sustain NP stability in the system and warrant the formation of a well-defined interphase boundary. Moreover, a reliable method of interfacial organization of NPs must be developed. Repeatability and controllability of the bulk solution-to-interface transferal process, leading to the organization of NPs, are imperative for a reproducible nanocomposite fabrication process. To ensure this high level of control the migration of NPs from the bulk phase to the interphase must be explained. Furthermore, production of a robust 2D nanomembrane involves strong cross-linking of NPs within the NP monolayer. An appropriate cross-linking agent must be selected for this reaction. Thus, the scope includes design and synthesis of a cross-linking molecule as a prerequisite for achieving the intended goals.

The 3D nanocomposite preparation requires fine-tuning of the synthesis parameters to guarantee homogeneous distribution of NPs within the matrix. Optimal conditions of the 3D nanocomposite fabrication process will be assured by appropriate selection of the polymer and NP surface ligands. Chemical structure of these components influence greatly the bonding manner of NPs within the nanocomposite. Presence of reactive groups in both, the polymer and ligands, is a way to make formation of strong chemical bonds possible. Covalent bonding between the polymeric matrix and NPs will provide resistance against aggregation of the nanoadditives. To ensure high repeatability of the nanocomposite, synthetic procedure the

mechanism of bond formation between the NP surface ligands and polymeric matrix have to be elucidated with an emphasis on the role of NPs in this reaction.

The design and synthesis of a versatile ligand has a crucial meaning for the successful obtaining of the desired 2D and 3D nanocomposites. Such NP surface passivating molecules should provide NPs with stability and reactivity. The structure of the cross-linking agent is equally important in case of the 2D nanomembranes. Design and synthesis of this ligand and cross-linking molecules is one of the principle objectives of the presented research. Structure confirmation requires execution of NMR experiments, whereas identification of the bonds formed within nanocomposites may be done via NMR and IR analysis. Properties of the designed ligand should be verified in case of a number of metallic NPs, such as AuNPs, PtNPs, and AgNPs. Therefore, the development of Ag and Pt NP synthesis methods, as well as Au, Ag and Pt NP functionalization methods is required. The as-prepared NPs should be characterized, via UV-Vis spectrometry and DLS technique, to determine their basic features, such as size and dispersancy. Furthermore, the obtained composites will be characterized using a wide range of methods – for example SEM and TEM imaging for determination of nanoadditives's distribution within the composites and thickness of the 2D nanomembranes, IR analysis for identification of chemical bonds within their structure.

1. Introduction

1.1. Nanoscale objects

In the metric system the prefix ‘nano’ is used to describe one billionth part of a unit of measure. Hence a nanometer is one billionth part or 10^{-9} of a meter. When dealing with small objects in the size range of 1-100 nm the nanoscopic scale is utilized. Crossing the boundary between the macroscopic and nanoscopic scales is coupled with a significant change of the materials’ properties.

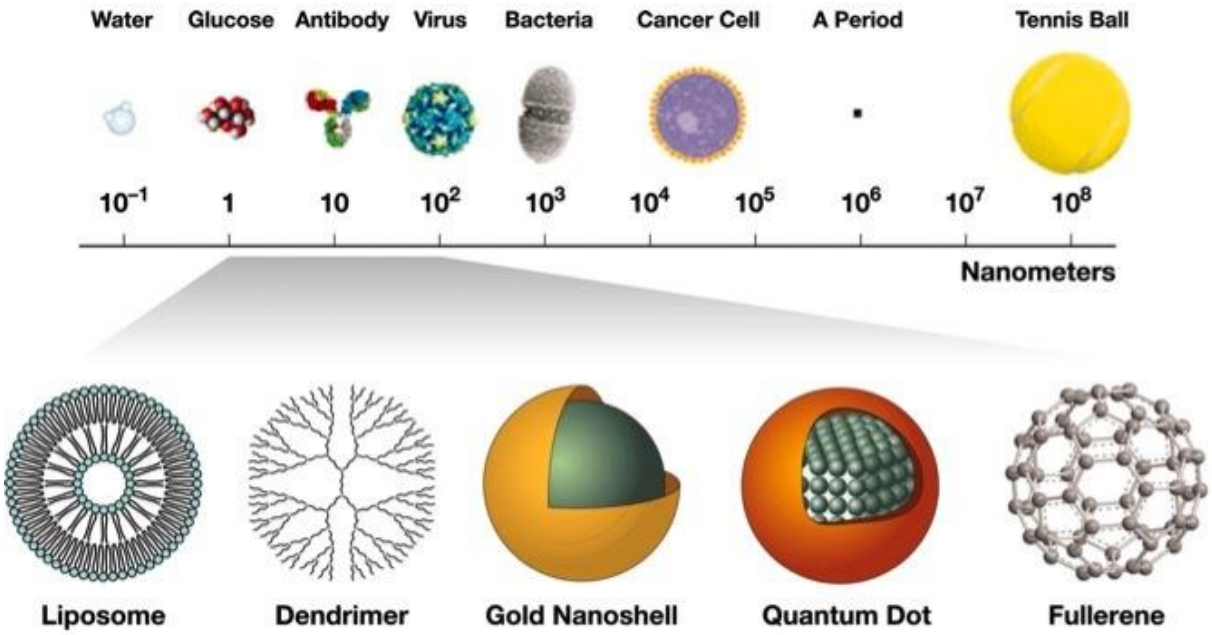

Fig 1. Scheme depicting the nanometer scale. A comparison of the size of different objects, including nanoparticles and quantum dots.[1]

At the nanometer scale properties of materials are known to be size-dependent and therefore differ substantially from those of bulk materials. Two specific effects responsible for this dependency can be identified. As the dimensions of objects are decreased, the so-called ‘quantum size effect’ and ‘surface effects’ become dominant. An example of materials exhibiting the described properties are metallic or semiconducting nanoparticles, which are clusters containing up to 10^7 atoms.[2] Clusters containing a number of atoms corresponding to the magic numbers possess high stability. Characteristic numbers referred to as the ‘magic numbers’ result from specific packing of atoms within a cluster, governed by successive

filling of electronic or atomic shells. These nanometer-scale inorganic particles are typically functionalized with a single layer of organic capping ligands to ensure their stability. Such particles are an intermediate state of matter between unbound atoms and bulk solids. The quantum confinement effect becomes relevant when the particle size is comparable to the de Broglie wavelength of its valance electrons.[3] Unlike in bulk metals, a gap between the valance and conduction band is present in metallic NPs. Decreasing the particles' size leads to conversion of the continuous density of electronic states into discrete electronic energy levels.[3] Strong confinement of electrons causes particles to behave electronically like zero-dimensional quantum dots. The surface effects on the other hand are linked to the increasing fraction of atoms at the surface when decreasing the size of an object. Surface atoms form fewer bonds, as compared to the ones hidden within the NPs, which influences the stability of nanoobjects. This in turn is strongly related to their chemical reactivity, with atoms at the surface being substantially more reactive. A lower mean coordination number of the surface atoms results from a single atom having less directly neighboring atoms than bulk atoms.[4] The surface effects have significant influence on the materials' properties. As a consequence a size dependence of thermodynamic properties such as the melting point or latent heat is prevalent. Both, the quantum size and surface effects, become more prominent as the size of particles is reduced.

It was the unique properties of NPs that drew vast attention to them within the scientific community in the 21st century. The possibility of obtaining materials with distinctive properties otherwise unattainable gives great promise for fabrication of novel functional devices. However, the history of NPs dates back much further. Naturally occurring NPs have been present long before the first reported syntheses. Such particles take on many forms, from organic particles (viruses, peptides) to various inorganic clusters.[5, 6] First signs of their use for utility purposes are known to come from the Ancient times. Gold nanoparticles AuNPs were first used around the 4th and 5th century B.C. as a ceramics dye, as well as a medical remedy for several diseases. The first accurate reference about their actual form, where it was recognized that AuNPs are essentially extremely subdivided elemental gold, was made in 1676 in a book written by chemist J. Knuckels.[7] The first publication describing the synthesis of AuNPs from a chemical point of view was published in 1857. In it M. Faraday reported on the reduction of chloroaurate ($AuCl_4^-$) with phosphorus in carbon disulfide.[8] Since the late 20th century a rapid growth of the number of publications concerning

nanoscience was observed. In modern science NPs are appreciated for their exceptional properties, of interest to both, fundamental and applied researchers.

1.1.1. Nanoobject shape

Nanoobjects come in many different shapes and sizes. Extensive research has been devoted towards elucidation of the shape-dependent properties of various nanocrystals. However, for correct interpretation of such dependencies a high degree control of the nanoparticulates' shape during synthesis is required. Apart from the most commonly known spherical NPs various other forms of nanostructured objects have been synthesized. Obtaining of differently shaped nanoobjects and precise control of their topological characteristics is achieved via judicious choice of experimental conditions and additives. Additives may trigger the growth of non-spherical nanostructures. Surface binding of appropriate molecules, such as surfactants, adsorbates, ligands, passivants, chelating agents or polymers, to the nanoobject is necessary for achieving appropriate shape control.[9] Commonly used additives utilized for directing the growth of NPs (particularly AuNPs), leading to differently shaped nanoobjects, are halides and silver ions.[10] Shape evolution of NPs may be governed via kinetic control, surface passivation, or a combination of both these mechanisms, depending on the types of additives. When the chosen additive reduces the rate of reaction the formation of lower-energy surface facets may be allowed in a kinetically-controlled reaction. When surface effects are dominating during NP synthesis, higher-index surfaces may be obtained during NP synthesis.

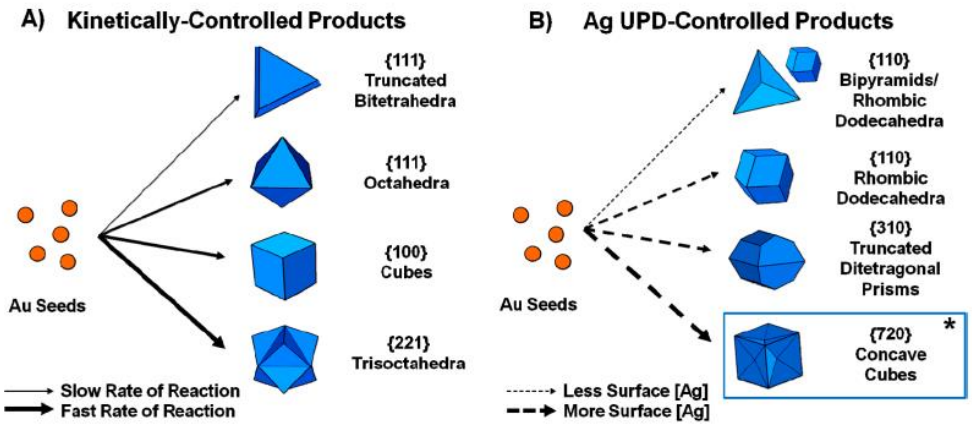

Fig. 2. Scheme illustrating the influence of halides and silver ions on the growth pathways of Au seeds leading to differently shaped NPs.[10]

Spherical NPs can be divided into nanowheels, nanoballs, core-shell type structures such as nanoeggs, nanoshells, nanocups, nanograins, and the already mentioned nanospheres.[14] The spherical shape of nanoobjects can be elongated in one direction to form nanorods. As a consequence of their protracted shape, the plasmon mode peak position of nanorods is varied with the change of their aspect ratio.[9] A comparison of rod-shaped NPs and spherical particles reveals an appearance of a surface plasmon band at lower energies.[12] Potent changes of nanorod solution color are observed as a result of minute changes in the nanorods' mean aspect ratio. (Fig. 3 – [12]). Generally, during the synthesis of rod-shaped NPs rigid templates or surfactants can be utilized.

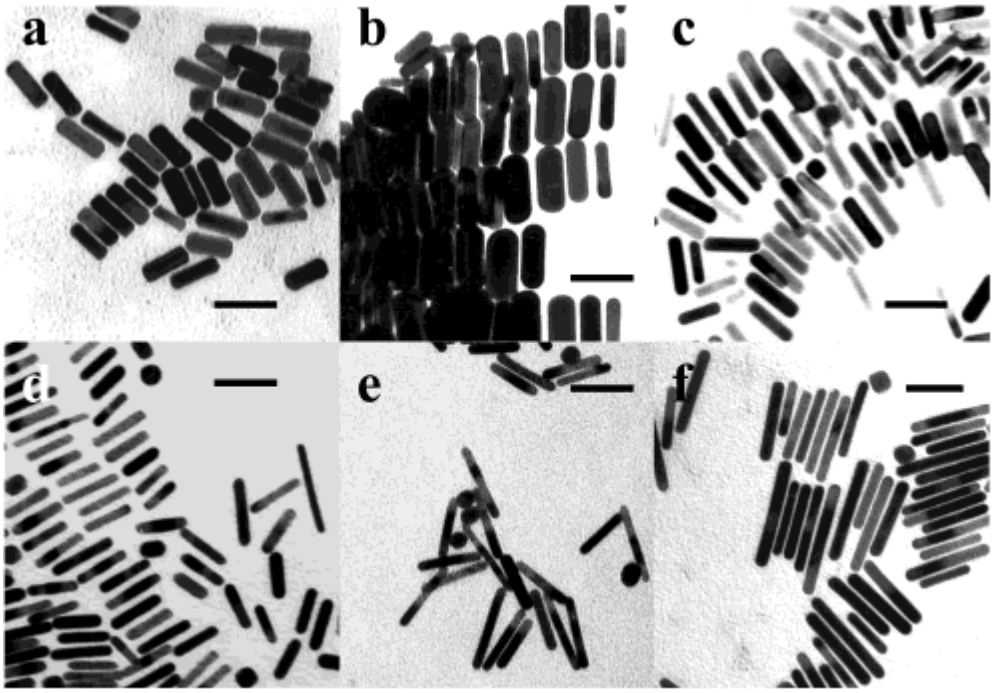

Fig. 3. TEM images of gold NPs with plasmon band energies at (a) 700 (b) 760 (c) 790 (d) 880 (e) 1130 (f) 1250. Scale bar is 50 nm.[12]

Other strongly elongated structures include nanowires, nanotubes, nanofibers, and nanoribbons/nanobelts. The morphology of the nanomaterials depend strongly on the synthesis process parameters. In general, the synthesis of one-dimensional (1D) nanostructures occurs by promoting the crystallization of solid state structures along one direction.[13] Unique properties of such 1D structures are closely related to their inherent anisotropy.[14] Such structures are characterized by an increasing bending modulus occurring with the reduction of nanostructure diameter. In case of nanowires with diameters smaller than 8 nm values of such mechanical parameters may be equivalent to those of diamond.[14]

This dependency is closely related to the effect of volume defect on the mechanical properties, where the increase of growth defects causes a degradation of the bending modulus. Nanobelt structures have been synthesized using semiconductive oxide substrates, such as ZnO, SnO_2, In_2O_3, CdO, Ga_2O_3, and PbO_2.[15] Such materials are characterized by a rectangular-like cross-section, and typically possess a width-to-thickness ratio of 5-10. Their length may reach up to a few millimeters [Fig. 4.]. These nanobelts are composed of a single crystal, not having any dislocations.

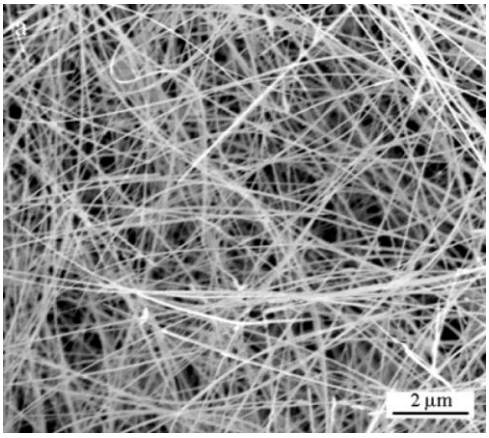

Fig. 4. SEM image of In_2O_3 nanobelts.[14]

Carbon may form nanotubes, which are seamless cylinders composed of graphitic layers, with diameters typically in the range of 0.8 – 20 nm. Single-wall nanotubes (SWNTs), having one graphene layer, and multiwall nanotubes (MWNTs), having more layers, can be distinguished.[16] Depending on the orientation of graphene lattice with respect to the tube axis, carbon nanotube walls can be either metallic or semiconducting. Carbon nanotubes are commonly used as additives in various materials for their enhancement or as a means of percolation network formation at small concentrations of additives.[17]

Nanocubes represent another form of nanostructures. When hollow inside (so-called nanoboxes) these nanoobjects may exhibit strong catalytic properties,[18] which may be important in the development of facet-specific catalysts. Such catalytic species often offer maximum available selectivity and activity.[11] Apart from cubic forms advances in the synthesis of various other polyhedral nanocrystals have also been made. Nanoprticulates with well-defined shapes, such as octahedral, rhombic, dodecahedral, and icosahedral have been reported.[19-26]

Nanostars can serve as an example of nanostructures studied to a lesser extent. A nanostar can be defined as a branched nanostructure with a central core and several protruding arms with sharp tips.[27-29] Application-imposed requirement for nanostars with defined shapes and uniform branches urges extensive research designed to provide better control of the symmetry and uniformity of nanostars. The presence of sharp tips in the structure of nanostars allows for a strong enhancement of the local field strength of the incident light. This dependence is the basis of plasmon-enhanced spectroscopy.[20] Moreover, the sharpness of the nanostars can be fine-tuned. Minor shape modifications enable manipulation of their optical properties,[30] hence it is possible to tune the LSPR of nanostars into the Near-Infrared (NIR) region, opening up the possibility of various biological applications.[31]

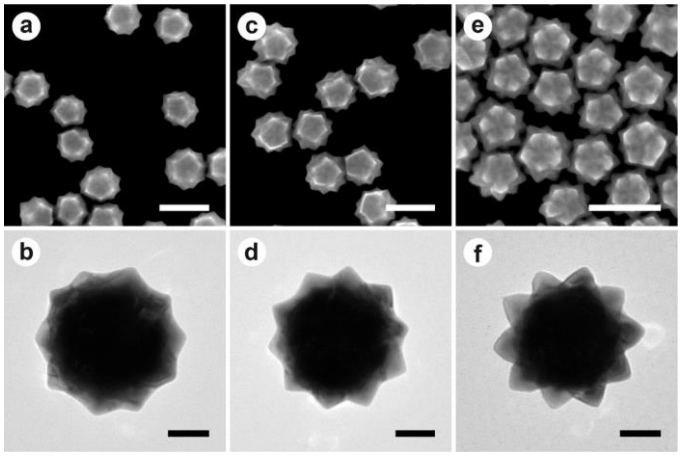

Fig. 5. Exemplary SEM and TEM images of Au nanostars. Scale bars: (a, c, e) 200 nm, (b, d, f) 50 nm.[31]

1.1.2. Chemical composition of nanoparticles

NPs exhibit great chemical diversity, as the composition of NPs may stretch across a wide variety of materials. Both inorganic and organic NPs can be distinguished. Organic NPs, being assemblies of organic molecules capable of forming a diverse assortment of different structures,[32] are usually stabilized via noncovalent intermolecular interactions. Amid the wide variety of inorganic NPs, NPs composed of metallic, semiconducting and nonmetallic elements, as well as their combinations, can be discriminated. The properties of the obtained NPs are closely related to the composition of the core.[33] Some inorganic NPs may exhibit more than one phase within their structure, which may considerably influence their physical

properties.[33] Amongst most commonly used metals for NP synthesis gold, silver, iron, platinum should be mentioned. Both single component, as well as heterogeneous NPs can be discerned. A common approach includes the formation of bimetallic NPs, where two elements form alloy NPs, even if bulk alloy formation is restricted.[34] Similarly the formation of heterogeneous zero-dimensional nanostructures consisting of both metal oxides and noble metals, is fairly common. Moreover, the core/shell structure is often achieved in heterogeneous quantum dots, where the composition of both layers (i.e. the core and the shell) differs.[33] In semiconductor NPs the band gap energies can be engineered via composition change, achieved through adjusting the constituent stoichiometries of the alloyed elements.[35] Carbon NPs pose a good example of nonmetallic inorganic NPs. Such nanostructures may exhibit beneficial characteristics, such as fluorescence.[36] Various structures of nonmetallic NPs are observed, from amorphous to nearly crystalline ones, including hollow well-organized spheres, where carbon atoms are sp^2 hybridized (i.e. fullerene NPs). As only metallic NPs were utilized during experiments conducted in the preparation of this dissertation, the focus of the following sections of this introduction will be directed solely towards metallic NPs and their nanostructures.

1.1.3. Synthesis of nanoparticles

Due to the extensive research a wide variety of NP synthesis protocols is available today, allowing precise control of both, size and shape of the obtained nanoobjects. The methods for the synthesis of NPs can be broadly divided into three categories: physical, chemical and bio-assisted methods.

Physical synthesis

The physical methods rely on the application of mechanical pressure, high energy radiations, thermal or electrical energy during NP generation.[37] The mechanical methods usually afford monodisperse NPs as a result of processes including melting, abrasion, evaporation or condensation. An example of a mechanical method is the High Energy Ball Milling (HEBM), where bulk materials are broken up into smaller particles by the moving balls, which transfer their kinetic energy to the milled material.[38] Other examples include the Inert Gas Condensation (IGC) and Physical Vapor Deposition (PVD). The former is an approach where

evaporated materials are transported with inert gases and condensed on a liquid nitrogen cooled substrate holder,[39] whereas the latter is a vacuum deposition technique, commonly used to obtain NPs, as well as thin layers of materials on the order of several nanometers. As an example of a vapor phase synthesis process the laser pyrolysis technique can be indicated, which is utilized for the synthesis of NPs.[40, 41] In this method a laser-induced chemical reaction at the interface between the laser beam and the molecular flow of gaseous/vapor phase reactants occurs. Sequential absorption of IR photons by the reactant, via resonant vibrational mode of the IR laser reaction leads to a rapid temperature increase in the gas. Excitement of molecules leads to molecular decomposition, followed by chemical reactions.

Chemical synthesis

Amid the chemical methods, there exists a great abundance of liquid phase routes. Fine-tuning of the morphology, and thereby properties of NPs is possible through the use of different reaction environments, capping and reducing agents.[42] Amongst different liquid-phase synthetic approaches such as syntheses by coprecipitation, hydrothermal/solvothermal processing, syntheses with the use of microemulsions as nanoreactors, via sol-gel processing, polyol synthesis and chemical vapor synthesis can be distinguished.[43] Each of these methods is described briefly below.

Microemulsion technique

Microemulsions are thermodynamically stable isotropic dispersions containing minimum three components: a hydrophilic phase, a hydrophobic phase and an appropriately chosen surfactant. The dispersed phase is formed by monodispersed droplets with sizes of 5-100 nm.[44] The surfactant type is the determining factor influencing the microemulsion structure, by establishing which of the components will form the continuous phase. Depending on this water-in-oil (w/o) and oil-in-water (o/w) emulsions can be distinguished. The role of the surfactant molecules is the reduction of surface tension between the microemulsion and the excess phase. This is achieved thru the formation of a sterically repulsive layer on the microdroplets' surface inhibiting their coalescence.[37]

Sol-Gel processing

The sol-gel process may be used for NP synthesis. The process begins with the formation of a stable solution of the solvated metal precursor, called the sol. In the next step the solution's viscosity is strongly increased, as a result of polycondensation or polyestrification reaction, leading to the formation of a gel. The gel is aged until solidification occurs. Simultaneously to this process Oswald ripening and phase transformations may take place. During the drying of the gel changes of its internal structure take place. The following dehydration occurring during calcination at temperatures of c.a. 800 °C, stabilizes the gel against rehydration, by removing of the surface bound hydroxyl groups. Further increasing of the temperature leads to densification and decomposition of the gels, as the pores of the gel network collapse and any present organic species volatize.

Hydrothermal synthesis

Hydrothermal synthesis is defined as synthesis occurring under high temperature and high pressure water conditions from substrates which are insoluble in ordinary conditions (<100 °C, < 1 atm).[45] This process is utilized for the synthesis of metal and metal oxide NPs.[46] Hydrothermal synthesis may be performed in supercritical water. This approach holds an important advantage as the rate of reaction is strongly enhanced. Control of the crystal phase, morphology, and particle size can be gained thru the use of supercritical water. Variation of temperature and pressure influences the solvent's properties (e.g. density), affecting the supersaturation and nucleation.[45] The described method is used to produce large amounts of NPs, having an optimized composition and surface chemistry, and adjustable size, morphology, and crystal structure.[47] Other advantages of this method include notable simplicity and enhancement of reaction rate.[45] The synthesis of TiO_2 NPs reported by Hayashi et al.[48] can serve as an example of utilization of this method.

Polyol synthesis

The polyol synthesis is a chemical process used for the synthesis of a wide range of metallic NPs (Cu, Pt, Pd, Pr, Ag), metal oxide NPs (ZnO, ITO), as well as magnetic NPs. In this process poly(ethylene glycol)s are used as the reaction medium, the reducing agent and the complexing agent, at the same time. An addition of stabilizing/protecting agents is required for successful synthesis of NPs. Amongst the factors influencing the NP characteristics the

type of polyol used during the reaction and the manner of precursor addition [49] should be pointed out.

Chemical vapor synthesis (CVS)

In this process, precursors in all three phases (solid, liquid, gas) are produced in the form of vapor, and in the vapor phase are brought into a hot-wall reactor. The conditions of the process are selected so that particle nucleation in the vapor phase occurs preferentially, instead of film deposition, as it is in case of chemical vapor deposition.[50] Notably, it is possible to obtain multi-component or doped NPs in this method, when a variety of precursors are used. The synthesis performed by Senter *et al*., whereby erbium was incorporated into silicon NPs,[51] can serve as an example of such a process.

Bio-assisted synthesis

Another approach for the NP synthesis is the bio-assisted methods for nanoparticle synthesis. This group of methods possesses several important advantages, such as low toxicity, cost-effectiveness and environmental friendliness. This approach encompasses the employment of various biological systems, such as microorganisms, plant extracts, or biomolecules as templates, for the synthesis of metallic and metal oxide NPs.

Biogenic synthesis using microorganisms

Microorganisms, such as bacteria and fungi, are extensively used as NP synthesis bio-reactors. In this method metal ions are captured and reduced by the microorganisms. The reduction occurs in the presence of cellular originated enzymes. This process may take place intracellularly (within the microbial cell) or extracellularly (on the surface of the cell). Bacteria perform the reduction reaction with the aid of anionic functional groups, proteins, enzymes and reducing sugars. Fungi, such as yeast, on the other hand, reportedly utilize the carboxyl, hydroxyl and amide groups on the cell surface during NP synthesis.[52, 53] The fungi mediated approach is characterized by economic viability, high bioaccumulation and, importantly, it can be easily scaled up, as a consequence of easy biomass handling.[37]

Biogenic synthesis using biomolecules as templates

For NP synthesis various biomolecules can be used as templates. Some examples include nucleic acids, viruses, and membranes. An example of a commonly used template is the

DNA molecule. Shape-sensitive ZnO NPs with various morphologies have been synthesized via this strategy in the presence of DNA as a bio-template.[54] Biological membranes also serve as beneficial templates [55] in NP synthesis due to the presence of ultra-fine pores within their structure. Utilization of viruses affords NPs uniform in size and morphology.[56] In this case the hollow spaces within the virus' structure are used as templates for NP fabrication.

Plant extracts for NP synthesis

Plant biomass assisted NP synthesis is a highly effective, eco-friendly and rapid method. This strategy is predominantly used for the synthesis of noble metallic, metal oxide, and bi-metallic alloy NPs.[57] The plant extracts provide components serving as reducing agents and capping agents necessary during the NP synthesis. The kinetics of NP photosynthesis is much higher compared to other biosynthesis methods. Approximately the rate of the synthesis reaction is in the order of magnitude of chemical routes rates.

For each of the above described methods extensive literature reports are available, however the conventional methods involving synthesis of NPs by reduction of soluble metallic derivatives are still most widespread. Most commonly utilized method of AuNP synthesis are summarized below.

Liquid-phase procedures for synthesis of gold nanoparticles

- *Citrate reduction*

A method developed by Turkevitch in 1951, consisting of the reduction of $HAuCl_4$ in aqueous environment, with the aid of citrate. This method results in NPs of ca. 20 nm diameter, with the surface stabilized by citrate molecules.[58] Numerous modification of this method have been reported. Simple variation of the ratio between the reducing/stabilizing agents and gold may result in better size scalability.[59]

- *Brust-Shiffrin method*

Method of synthesis of alkanethiol stabilized NPs in a two-phase system. The chloroaurate salt is initially transferred into the organic solvent using tetraoctylammonium bromide, where it is reduced with sodium borohydride in the presence of thiol molecules.[60, 61] In this method control of the NP polydispersity and size can be achieved by change of reaction conditions. Factors such as thiol/gold ratios, temperature and speed of reductant addition have a dominant effect on the resulting NPs. The described procedure was later modified by Brust.[61] The introduced modification allowed for single-phase syntheses of NPs using different thiol capping agents.

- *Martin method*

Martin reported the synthesis of negatively charged, soluble in water AuNPs, which can later be functionalized with organic ligands to ensure their stability in the hydrophobic phase.[62] In this method acid stabilized solution of $AuCl_4^-$ was reduced by a base stabilized $NaBH_4$ solution. The diameter of the NPs is regulated by changing the gold/BH_4^- ratio during the synthesis. The obtained NPs are then transferred into the organic phase by vigorous shaking with 1-dodecanethiol in the presence of acetone. During this process the NPs are coated with the organic ligands.

1.2. Nanoparticle characteristics

1.2.1 Ligand stabilization

Appropriate surface modification of NPs provides them with sufficient stability and determines their properties. Surface functionalization regulates NPs' interaction with the surrounding environment, influencing their behavior, such as tendency towards self-organization and agglomeration.[63] Sufficient dispersion of NPs within a given matrix is guaranteed by appropriate compatibilization of particle surface to the surrounding medium. Therefore, surface modification serves as an unswerving route towards development of stable dispersions.[64] Organic ligand coatings form stable protective layers against irreversible aggregation of NPs in hydrophobic solutions, while charged or polar capping agents afford stability to NPs in polar environments. In both cases stronger stabilization is observed when capping agent molecules form dense, strongly bound layers. An optimal coverage of the

surface by a given ligand corresponds to the minimum free energy. Therefore the ratio of the surface modifier to the nanoobject feed can be used as a means of tailoring the particle size.[64] The ligands can be thus considered as size controlling agents.

Overall, stabilization of NPs may occur due to electrostatic repulsion, interaction of the hydration layer on the NP surface or steric exclusion. In the latter case steric interaction caused by the overlapping of the coordinating species' chains is unfavorable and may lead to a rise of the repulsive forces. Due to the steric repulsion of hydrocarbon molecules anchored on the NPs' surface stability is maintained even during drying of NPs.[60]

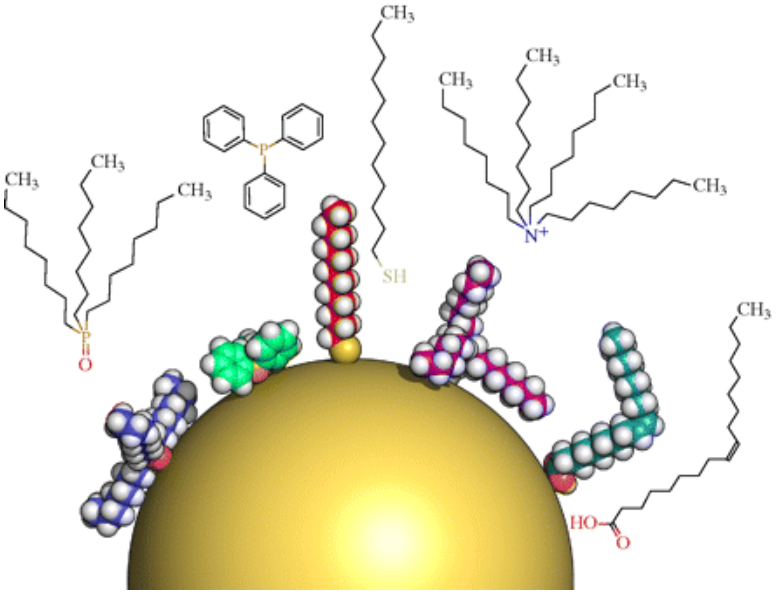

Fig. 6. A nanoparticle with different hydrophobic ligand molecules on its surface: trioctylphosphine oxide (TOPO), triphenylphosphine (TPP), dodecanethiol (DDT), tetraoctylammonium bromide (TOAB) and oleic acid (OA), respectively.[63]

Binding of ligands to the surface of NPs may occur in particular in the existence of attractive forces between the ligand molecules and the NP surface. These interactions include chemisorption, electrostatic attraction or hydrophobic interaction.[63] When chemical bonds are formed the mean coordination number of surface atoms should be considered, since the ability of NPs' surface atoms to interact with ligand molecules is derived from their incomplete valance. Therefore, atoms on the edges, terraces and vertices of a NP will not necessarily all form equivalent bonds with a given capping agent. The nature of these surface

atoms may be compared to metal complexes which selectively bond with appropriate ligands.[65] Moreover, as the affinity between each type of ligand and a given NP is dissimilar exchange of weaker bound ligands by stronger binding ones may occur. To determine whether such ligand switching will take place ligand binding strength must be considered. For example it can be predicted that thiol compounds make excellent stabilizing agents of AuNPs due to high affinity of sulphur and gold. The Pearson's Hard Soft Acid Base (HSAB) theory imparts that both elements have soft character making them prone towards strong bond formation. However, as the above discussion implies, although some general predictions can be made affinity between nanoobjects and organic ligands should be considered individually in each case.

1.2.2. Nanoparticles' physiochemical properties

Properties of NPs are size-, as well as shape-dependent. The shape and structure of NPs are strongly dependent on the number of atoms forming them.[66, 67] The stability of NPs of a given shape and structure is determined by its surface energy. However, the geometric shape of NPs of the same size may differ, with the most densely packed structure being formed preferentially.[68] NPs often adopt a spherical shape in order to minimize the surface energy. For NPs of a small size, in the range of 1-100 nm, both chemical [69] and physical properties [70, 71] strongly differ from those of their corresponding bulk materials. This is caused by large surface-to-volume ratio, which greatly impacts the physical properties, such as the thermodynamic behavior, of such entities.[68]

1.2.3. Mechanical properties

The basic mechanical properties of NPs can be described by their hardness and elastic modulus. Size-dependent behavior is often observed when considering the NPs' mechanical properties. Quantities such as the elastic modulus and hardness can be calculated by measuring the particles' deformation via Atomic Force Microscopy (AFM). It has been indicated that dislocations or stacking faults within the NPs' crystalline structure are responsible for the change of their mechanical properties as compared to the bulk material.[72, 73] Direct proof of this concept was provided by *in situ* TEM nanoindentation

measurements.[74] In the experiment presence of dislocations in the NPs under stress was evidenced.

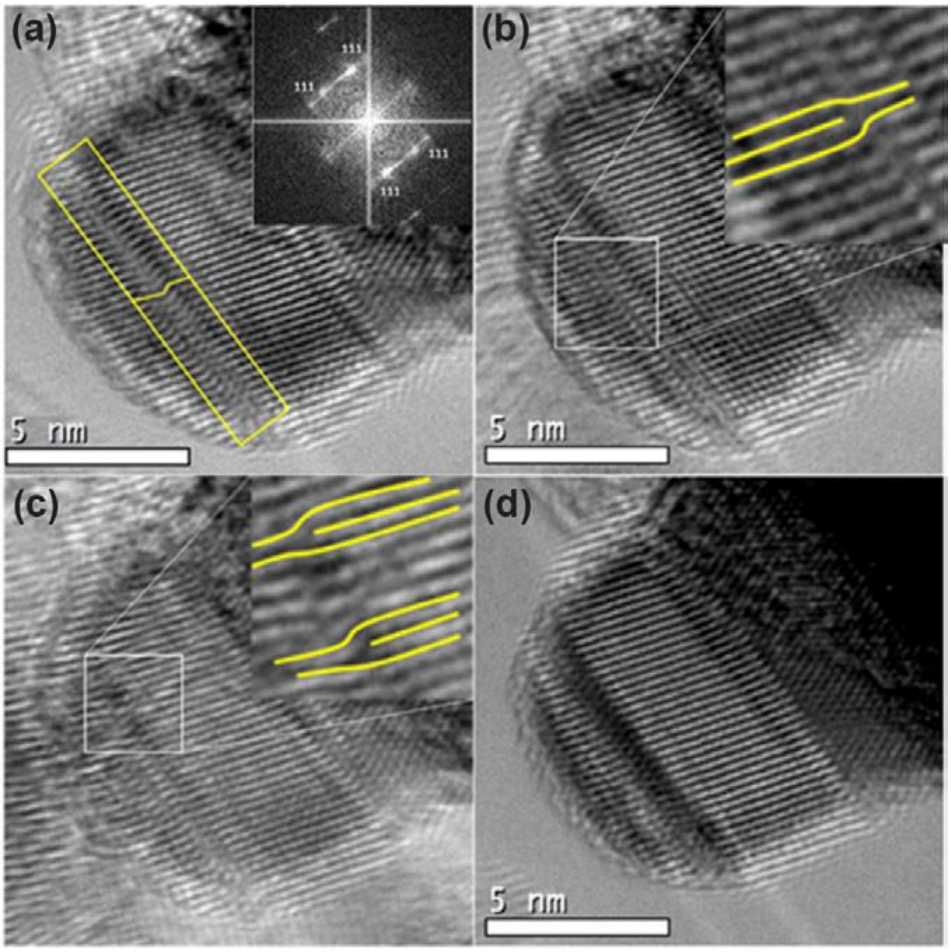

Fig. 7. High-resolution TEM images of a silver NP before and after compression: (a) before compression (twin highlighted); (b) at the initial stage of compression (an edge dislocation highlighted); (c) at a stage of further compression (two additional dislocations shown in the inset); (d) after the removal of the compression (no dislocation observed).[72]

It was shown that such structural defects disappear during the unloading process. The existence of stacking faults which could nucleate, migrate and annihilate under mechanical loading were also demonstrated with *in situ* TEM.[75] Furthermore, shape-dependence of the particle strength may exist due to the competition between generation of dislocations and their drainage from the NP.[76] Other sources indicate the alternation of the NP bond energies and lattice strain as the origin of the modification of mechanical characteristics.[77]

Other important mechanical properties, such as the adhesion and friction of NPs, can also be determined with the aid of the AFM technique. NP – solid surface adhesion and friction can be obtained from the deflection of the cantilever using two different approaches. By approximating the AFM tip to a NP or by factually attaching a NP of known size, shape and composition to the microscope's force sensor prior to the measurement.[78] NP – solid surface adhesion and friction forces for NPs of different sizes were measured by Guo *et al.*[79] A dependence of the friction forces proportional to the 2/3 power of the radius was shown. Other studies revealed a linear dependence of the adhesion force on the reduced radius.[80]

1.2.4. Thermal properties

A prominent alternation of thermal properties occurs when the size of particles approaches the nanoscopic scale. The cohesive energy of a material decreases with the reduction of its size, making it less stable.[68] This leads to a strong melting-point depression, which occurs with a decrease in particle dimensions.[81] The observed changes are closely related to the large surface-to-volume ratio of the NPs.

The thermal conductivity (k_b) of a solid material is also size-dependent below a critical particle size, since the thermal conductivity of a bulk material is directly proportional to the mean path of an electron in the material.[82] When the size of the particle is of the same order as the electron mean path, boundary or interface scattering becomes significant. This leads to a decrease of the particle's k_b with decreasing size.[82] A similar relationship has been observed for thermal conductivity of a thin film of metallic NPs. A decrease of its k_b value with thinning of the film was evidenced.[83]

1.2.5. Optical properties

Interaction of the incident light wave's electric field with matter may excite oscillation of electric charges. When the size of the particles is much smaller than the incident wavelength the induced electric field may be approximated as constant. Subjecting NPs to such external electromagnetic radiation may induce coherent oscillations of surface atoms' free electrons, giving rise to the so-called localized surface plasmons (LSP).[84] LSP can be described as plasmons that oscillate locally around the NP with a frequency known as the localized surface

plasmon resonance (LSPR). As the nuclei's position is stationary in the presence of light periodic charge separation is observed as the electrons oscillate, leading to generation of oscillating dipoles.

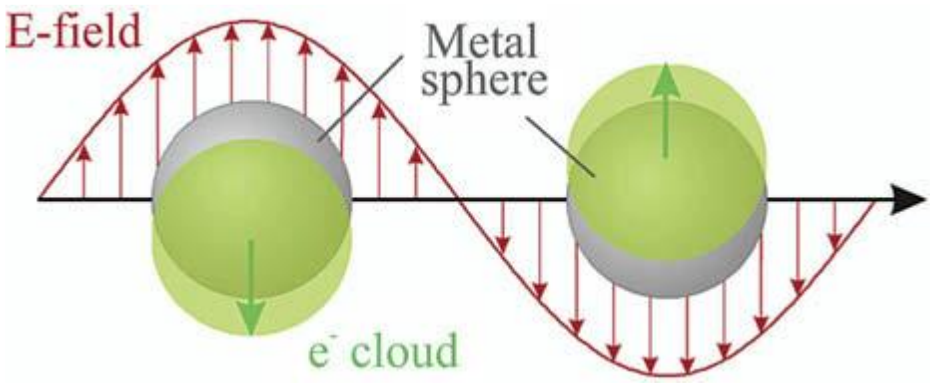

Fig. 8. Schematic depiction of plasmon oscillation of a nanoparticle, showing the displacement of the conduction electron charge cloud relative to the nuclei.[85]

A reasonable prediction of the scattering of electromagnetic waves by spherical particles is given by Mie's theory, offering a solution to Maxwell's equations.[86] Since LSPR is strongly dependent on both size and shape, its' prediction for non-spherical particles required an introduction of a modification to the Mie theory. The introduced change incorporated the input of both, longitudinal and transverse dipole polarization modes into the LSPR calculations. Moreover, the description of the optical behavior of NP assemblies requires a different approach, as the Mie's theory is not applicable to NP agglomerates. In this case the properties of both individual NPs and their aggregates must be taken into consideration for accurate optical properties description. This was first done by Maxwell and Garnett in 1904.[87]

The frequency of the collective oscillations of conduction electrons is coupled with the incident light wave, and depends on the local dielectric environment. This means that the NPs' absorption at the SPR wavelength is dictated by the interaction of individual particles with the surrounding environment, as well as by the NP-NP interactions.[88] Hence, an LSPR wavelength shift indicates a change in the local environment, making plasmons suitable for exploitation in sensing platforms. A representative example of the high LSPR environmental sensitivity is the change of surface plasmon oscillation during NP aggregation. In this process electromagnetic coupling of plasmon modes of adjacent NPs occurs. This leads to the

formation of a new band in the NPs' extinction spectrum, resulting from the interparticle plasmon coupling.

1.2.6. Catalytic properties and chemical reactivity

Nanocatalysis is an area of catalyst science that offers significantly enhanced reactivities and selectivities as compared to conventional heterogeneous catalysis. The catalytic performance of NPs is known to be highly size-dependent, wherein an increase in the activity is observed with the enlargement of surface-to-volume ratio. However, the range of parameters actually influencing the functioning of nanoscale catalysts is very broad. Factors such as geometry, oxidation state and composition must be taken into consideration.[89] The high reactivity of NPs in catalysis is thought to be a sum of contributions of size-dependent qualities and NP-support interactions.[90] Properties related to the small size of NPs include the quantum size effect, the abundance of low coordinated atoms, as well as the presence of excess electronic charge.

The presence of undercoordinated atoms, associated with surface roughness is important for the nanocatalyst's activity.[91] Smaller sized clusters possess higher step site densities, with low-coordinated atoms available.[92] Due to large discrepancies in the adsorption activation energies when considering step versus terrace sites, the size of clusters affects the strength of adsorption of reagents.[93, 94] Individual electronic properties of sites, determined by the NP composition and chemical state, may also have a stabilizing effect on the reagents and intermediate products. These effects will have direct influence on the reaction rate, and thus the chemical reactivity of NPs.

Another important factor that should be taken into account when considering NP reactivity is the shape of the stable cluster. NPs of different shapes exhibit various crystallographic facets. Specific facets are characterized by their own distinct reactivities and selectivities,[95] affecting the chemical reactivity of the NP. Some authors indicate the number of sharp corners and edges (i.e. the number of low coordinated sites) as the factor determining the reactivity,[96, 97] rather than the facet type. Nonetheless, weather it is the facet kind or the undercoordinated sites the influence of NP shape has been observed in numerous studies.[95, 98]

1.2.7. Magnetic properties

Materials can be classified based on the response of their intrinsic magnetic dipoles and magnetization when in the presence and absence of an external magnetic field.[99] This response is dependent on the susceptibility and permeability of a material. The susceptibility is identified by the ratio of induced magnetization (M) to the applied magnetic field (H),[100] whereas the permeability is defined by the ratio of magnetic induction (B) to this field (H).[101] The so-called ferromagnetic material possesses a net magnetic moment derived from the presence of spinning electric-charged particles, i.e. unpaired electrons. Due to parallel orientation of adjacent dipole moments even in the absence of an applied magnetic field a net magnetic dipole moment subsists.[102] Reduction of the size of a bulk material to the nanoscopic regime alters its magnetic properties, such as the magnetic moment per atom or the magnetic anisotropy.[103] The magnetic properties of NPs depend on a variety of physical parameters, such as their size, shape, composition and microstructural details of shell and core architecture.[102] Alternation of these factors will cause a change of the NPs' magnetic qualities, such as the saturation magnetization (maximal induced magnetization), the remanent magnetization (induced magnetization that persists after the removal of the external field) or the anisotropy energy (the energy preserving a particular orientation of the magnetic moments).

A bulk ferromagnetic material consists of small magnetic domains having uniformly aligned magnetic moments of all atoms within the domain. This results in a net magnetization of each domain.[104] Since such domains have a critical size of c.a. 10-100 nm NPs may possess a single magnetic domain within their volume, due to their small size.[105, 106] The particles are then uniformly magnetized and all spins are aligned homogeneously. Moreover, above the so-called blocking temperature the NPs may display superparamagnetic behavior,[107] manifested as zero coercivity (intensity of an external coercive field needed to force the magnetization to zero), and the absence of hysteresis of the sample's magnetization as a function of field exposure. In this case spontaneous demagnetization may occur as a consequence of thermal fluctuations,[108] since values of moment reversal energy barrier are comparable to these fluctuations and may be rather easily exceeded.[102] In case of superparamagnetic NPs a rapid increase of magnetic moment in the direction of the field is

observed under the influence of an external field. This is caused by the coupling interactions in single-domain magnetic materials, resulting in high magnetic susceptibilities.[100]

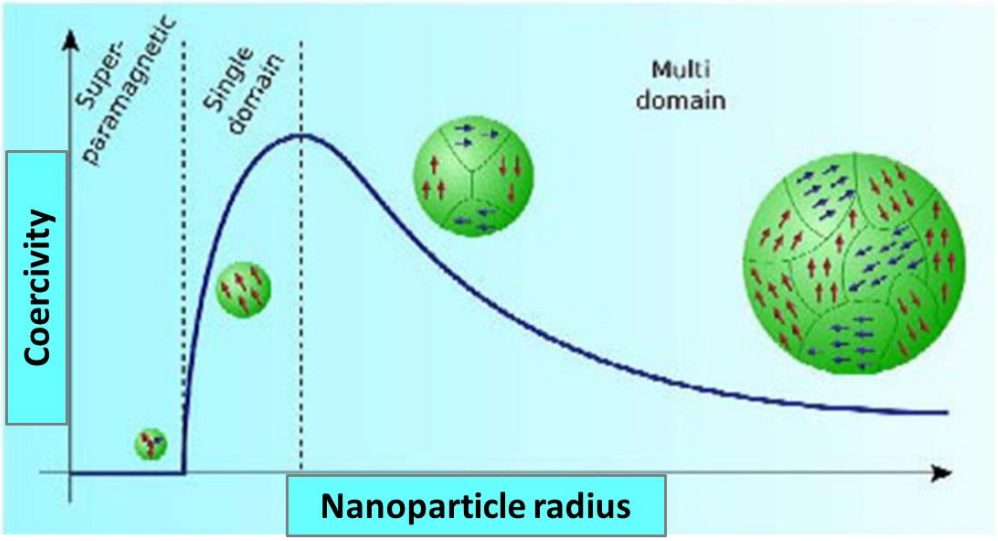

Fig. 9. Schematic presentation of the coercivity-size relations of nanoparticles.[108]

1.3. Nanoparticle self-assembly

1.3.1. Supramolecular self-assembly

The focus of supramolecular chemistry is the study of the structure, property and change of matter with special emphasis on non-covalent bonding of particles.[109] Non-covalent interactions notably influence the hierarchical structure of assemblies of molecules. This in turn is reflected strongly on their properties. The particles' intrinsic properties (charge, polarity, shape, size, structure) determine their manner of interaction with other entities in a given system.[110] An averaged interaction, being the sum of all attractive and repulsive forces between the components emerges. The interplay between these individual interactions may lead to the self-assembly process. Self-assembly can be defined as the autonomous organization of components producing patterns or structures at any scale.[111] Some authors limit the term 'self-assembly' further only to processes that involve the reversible organization of pre-existing components, controlled by their appropriate design.[111] This process may occur through the system's equilibration. An energetically favorable balance is reached between the aggregated states and separated particles or through the adjustment of

particles' positions within an aggregate. Acquiring this energetically advantageous organization is the result of an interplay of various supramolecular interactions, such as ionic, hydrogen, Van der Waals or coordination bonds.[112] Profound understanding of the mechanisms governing the self-assembly process should provide a means of controlling it. Then, cost- and energy-effective fabrication of functional materials with tailored properties (i.e. nanostructured materials) would be feasible.

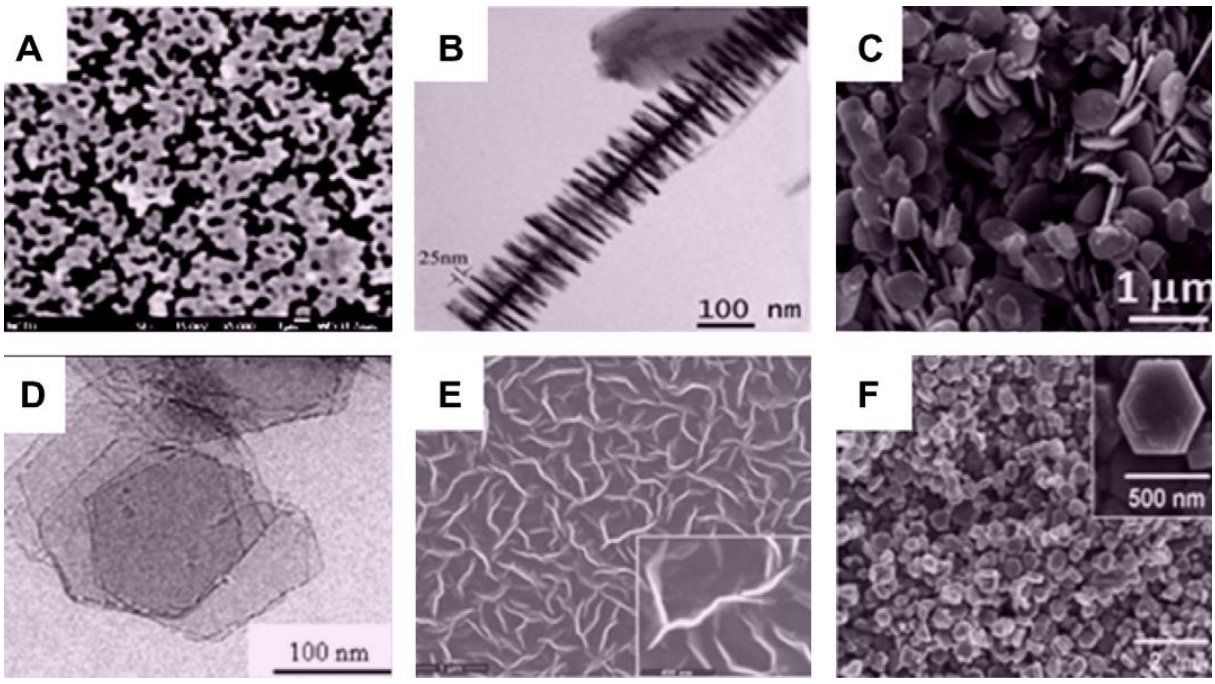

Fig. 10. Typical SEM and TEM images of 2D nanostructures: junctions (continuous islands) (a), branched structures (b), nanoplates (c), nanosheets (d), nanowalls (e), and nanodisks (f).[113]

When considering fabrication of nanostructured materials two main strategies can be distinguished: the 'top-down' and the 'bottom-up' strategy. The 'top-down' approach comprises processing of bulk materials to obtain nanostructured systems. Patterning of the starting mother material may occur by various chemical, physical and mechanical methods, such as X-ray, electron beam or optical light lithography and chemical etching to name a few.[114] These methods lead to the removal of access material from the bulk sample, leaving nanoscopic structures of choice. The complexity of the obtained nanostructure stems from the capabilities of the devices used for the assembly. Usually the resolution of the obtained nanopatterned structures is relatively low. The 'bottom-up' approach on the other hand offers substantially higher resolution. It involves the formation of nanostructures with the aid of

nanometer-sized building blocks as the starting material. Controlled assembly of such moieties, impelled by the adoption of the lowest-energy configuration, affords the desired materials. In this case the complexity of the assembled nanostructure is determined by the properties of the building blocks.

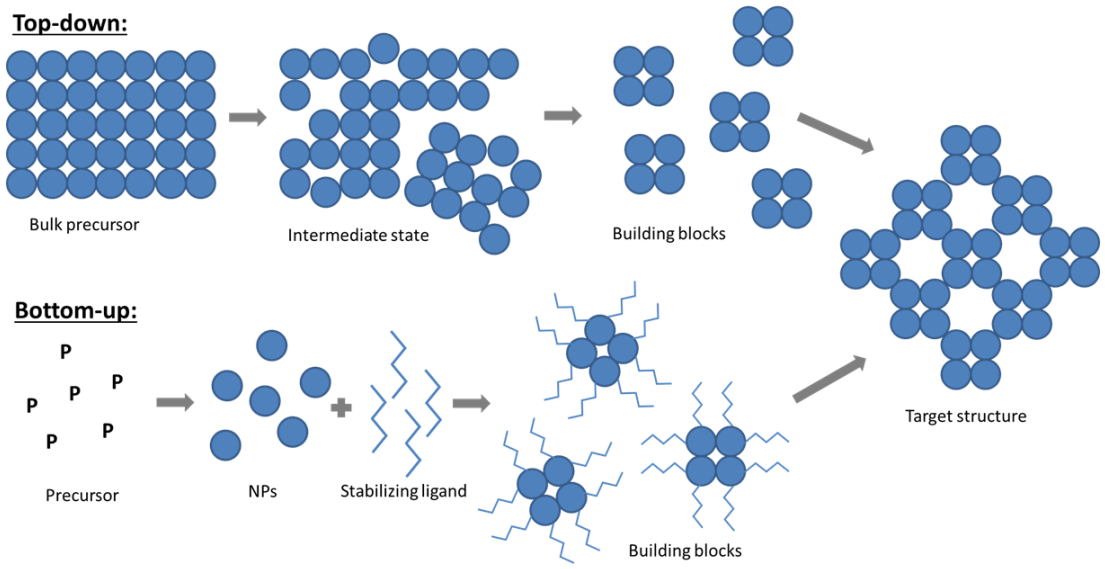

Fig. 11. Comparison of the top-down and bottom-up methods of nanostructure fabrication strategies.

Combining the long-range high order of nanostructures produced in the top-down approach with the high-level resolution of bottom-up nanostructures is a desirable direction pursued in material sciences. Successful bridging of these prerequisites may be achieved through the self-assembly processes.[115]

The self-assembly process is governed by short- and long-range interactions prevailing within the system. The existing interactions depend on the composition, atomic structure, surfaces, as well as shape and size of the constituents. Through the appropriate choice of these properties information regarding their assembly may be encoded,[116] allowing for the so-called programmed assembly. Programmed assembly of nanostructures is a concept that relies on the utilization of encoded information, which specifies the building blocks' position and connectivity within an assembled structure. In line with this strategy the formation of various arbitrary structures, that are currently obtainable only via three dimensional (3D) printing, is possible by means of self-assembly. Two theoretical approaches have been distinguished for the realization of this concept – the puzzle and the folding approach. The former relies on highly selective, directional interactions as a means of encoding the assembly data, whereas

the later relies on specific one dimensional (1D) sequences that program the 3D spatial arrangement of structure constituents, using relatively non-specific interactions.

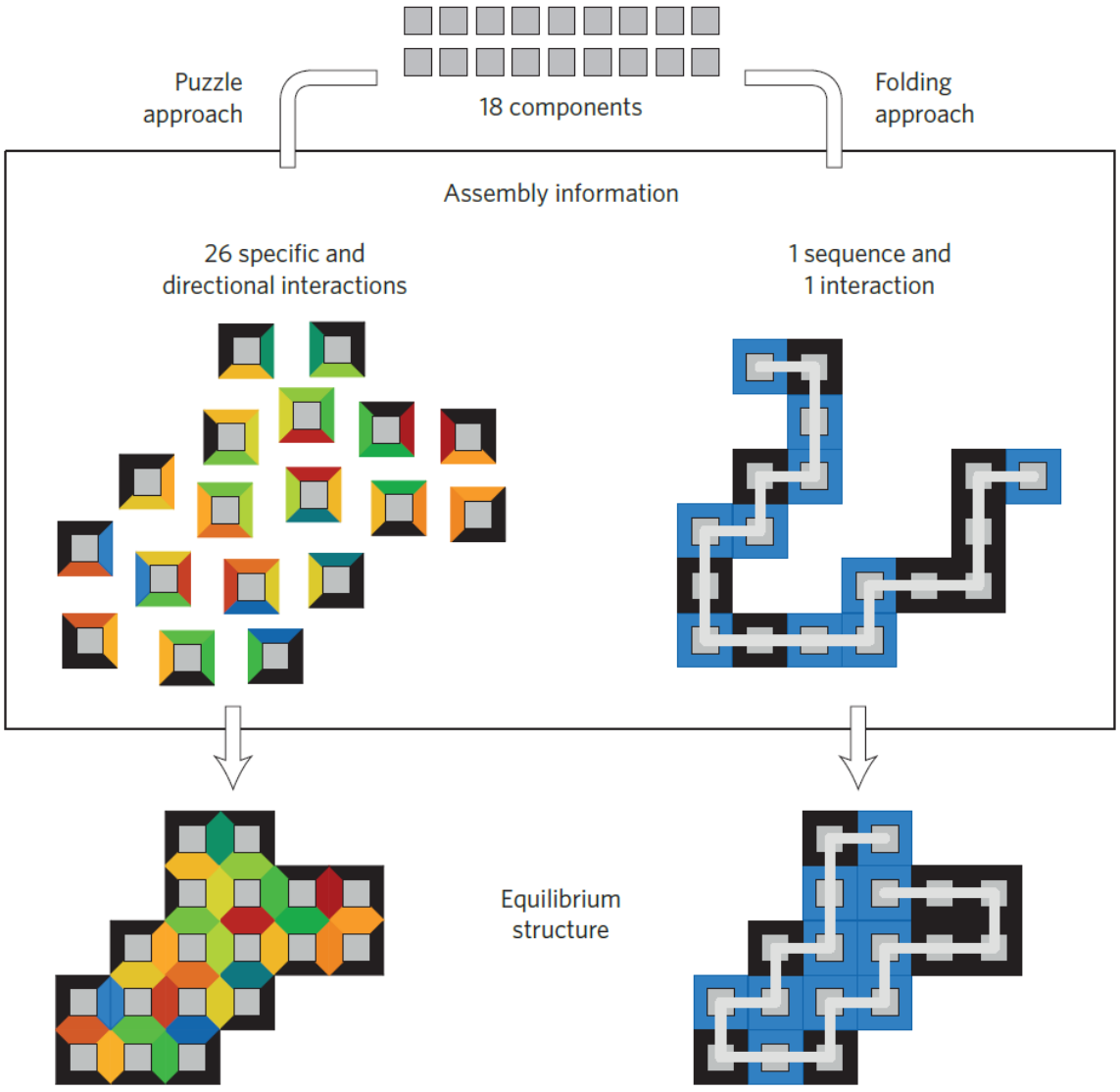

Fig. 12. Schematic representation of the puzzle and folding strategies for information-driven self-assembly.[116]

Despite a well-described body of conceptual work the practical use of these approaches is still limited. The currently employed self-assembly strategies are restricted to structures of high symmetry,[116] such as periodic superlattices [116-123] or linear chains.[124] Periodic structures are exhaustively defined by their unit cell, hence the number of specific interactions needed for their self-assembly is fairly small. Complex arbitrary structures, on the other hand,

are currently unattainable via self-assembly, since a large number of specific interactions is required in this process. Due to synthetic limitations colloidal components do not yet contain the necessary information for spontaneous formation of highly complex structures.[116] At present, strategies that combine the selective interactions of the puzzle approach with different forms of cooperativity distinctive for the folding approach hold the most promise for successful formation of complex assemblies.

The dependency of the self-assembly process on relatively weak chemical bonding allows the component particles to retain some mobility within the system. This means that a system can respond dynamically to changes in its environment. Hence, upon a shift of the system's equilibrium state due to a change of the conditions, straightforward adjustment of the particles' assembly is possible. Exciting material properties are derived from this feature, such as rapid response to external stimuli or the self-healing ability.[125]

The nature of the self-assembly process can be twofold from a kinetic point of view. Static and dynamic self-assembly can be distinguished,[111] where the static process takes place in globally or locally equilibrated systems and leads to the formation of stable ordered structures, that do not dissipate energy. Dynamic self-assembly on the other hand occurs in non-equilibrated systems. The formation of nanostructures is related to energy dissipation. Some authors distinguish also a third type of self-assembly – the 'templated self-assembly',[111] templates being entities containing active sites for selective NP deposition.[126] The foundation for this classification is the occurrence of two types of interactions within the self-assembling systems – the direct and indirect interactions.[126] The latter kind encompass interaction of particles with distinctive elements of the environment, such as templates. Templates are regarded as a form of external stimulus, leading to directed self-assembly (DSA). DSA offers improved control of intrinsically self-assembling systems as a result of employing additional incentives.[126] Apart from templates these can also include directing agents and external fields.

1.3.2. Strategies for NP self-assembly

Self-assembly in solution

This approach exploits specific interactions between distinct surface ligands on chemically heterogeneous NPs.[124, 127] Through the appropriate choice of ligands these interactions can be precisely tuned to afford the anticipated ordering. The resultant structure is a consequence of a balance between the existing attractive and repulsive forces.

Templated self-assembly

The alignment of NPs is defined by the colocation of NP binding sites on the template. Soft (synthetic polymers,[128] DNA molecules[129]) and hard (carbon nanotubes [130]) templates can be distinguished, with the former being more suited for control of NP spacing.

Self-assembly at interfaces

The interface, being a common boundary between two separate phases of matter, has been used successfully as a platform for NP self-assembly. Interfaces between immiscible phases, such as the liquid-gas, liquid-liquid and liquid-solid interface may be used for NP organization. Common techniques used in this process are evaporation induced self-assembly,[131] sedimentation, or the Langmuir-Blodgett technique.[132]

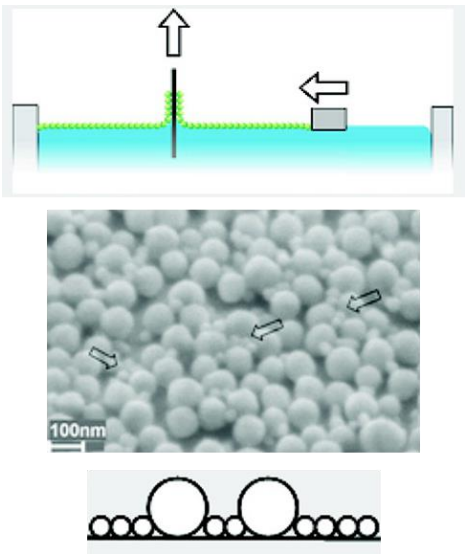

Fig. 13. Schematic illustration of the deposition of NPs using the Langmuir-Blodgett approach, resulting in a 2D nanomaterial.[133]

In the Langmuir-Blodgett technique the NP array is formed at a liquid-gas interface, and is later transferred onto a solid substrate without loss of the attained NP arrangement. Control of the NP surface density in the obtained array can be executed through modification of the substrate's wetting and retracting speed. High-order nanostructures deposited on solid surfaces can be fabricated using the evaporation-mediated approach. During the evaporation of the solvent the interaction between NPs becomes more pronounced, since the screening effect of the solvent is diminished.[134]

The self-assembly of NPs at liquid interfaces is driven by the reduction of interfacial energy.[135] A gain in free energy as a result of the reduction of direct contact between NPs and the two bulk phases follows the interfacial adsorption of NPs.[136] Moreover, the overall effective interfacial tension of the system decreases with increasing NP coverage of the interface.[136] As argued by Pieranski [137] the decrease of interfacial energy occurring upon the placement of a single spherical particle at the interface is given by the following equation:

$$\Delta E = -\frac{\pi R^2}{\gamma_{o/w}}\left(\gamma_{o/w} - \gamma_{p/w} + \gamma_{p/o}\right)^2,$$

where $\gamma_{o/w}$ – oil/water interfacial energy; $\gamma_{p/w}$ – particle/water interfacial energy; $\gamma_{p/o}$ – particle/oil interfacial energy and R – radius of NP. A necessary condition that must be met for the adsorption of NPs at the interface can be described accordingly: $\gamma_{o/w} > \left|\gamma_{p/w} - \gamma_{p/o}\right|$. As the energy reduction, ΔE, is proportional to the square of NPs' radius, a clear size-dependency of NP self-assembly is manifested. Particles in the nanoscopic size regime are confined to the interface by an energy reduction comparable to thermal energy.[138] Therefore, once adsorbed at the interface a thermally activated escape of NPs may occur, whereby the escape of smaller particles requires a smaller input of energy. Larger particles are therefore adsorbed at the interface preferentially. The desorption energy depends on the interplay of several different interactions within the system. In addition to the particle-water and particle-oil interactions, particle-particle interactions are significant here.[138] Furthermore, particle surface wettability impacts strongly the desorption energy,[139] as this parameter influences the interfacial tension. Wettability is described by the contact angle, Θ, between the solid particle and the oil/water interface.

Fig. 14. Changes in wettability of solid particles at the oil/water interface at contact angles < 90° and > 90°.[138]

As the contact angle increases from 0 to 90° the desorption energy rises, reaching a maximum value at 90°. Further growth of Θ causes gradual fall of this energy. This variation is depicted in Fig. 15.

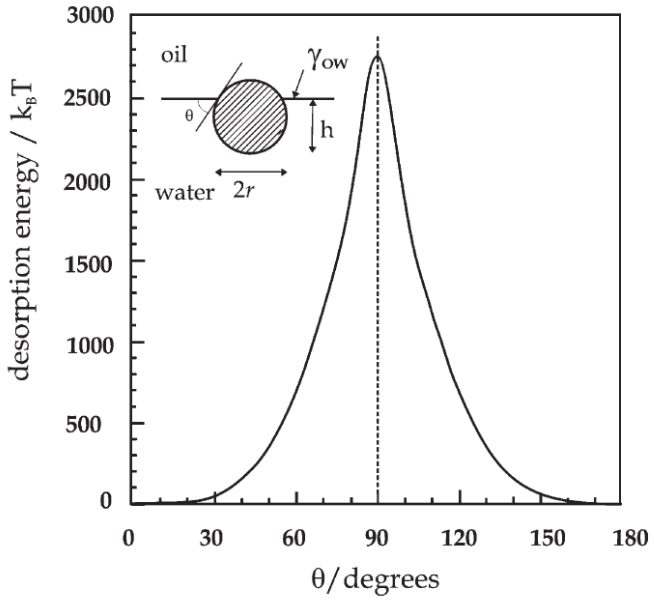

Fig. 15. Dependence of the desorption energy of a spherical particle at a planar oil/water interface as a function of the contact angle Θ, where h – depth of the particle's immersion into water, r – particle radius (10 nm), $\gamma_{o/w}$ – interfacial tension (36 mN/m).[137]

This dependency has been practically utilized for NP interfacial assembly, whereby the appropriate contact angle was achieved by appropriate functionalization of NP surface [140] or addition of a solvent changing the hydrophobicity of the NPs.[141]

Assisted self-assembly

Self-assembly may occur under the influence of external forces, such as electric [142] and magnetic fields,[143] light [144] or shear force. High-speed and precise control of the NP arrangement is achievable through this strategy.

Magnetic field is used for ferromagnetic and superparamagnetic NP organization. Dipole-dipole association leads to the formation of organized structures in the case of NPs with sufficiently high magnetic moments. NP alignment in the presence of an electric field can occur in case of polarizable NPs through dipole-dipole interactions. Organization in accordance with the field direction occurs. Light-assisted assembly commonly involves irradiation-induced structural changes in photoswitchable NPs, which trigger NP organization.

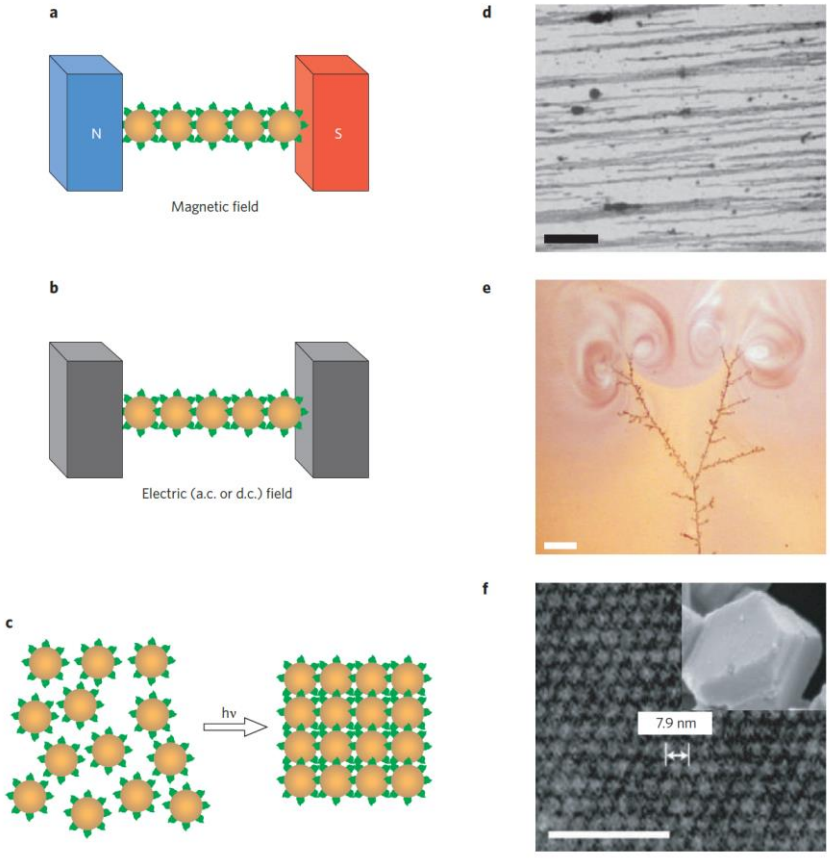

Fig. 16. Schematic illustration of assisted assembly of NPs under the action of a magnetic field (a), electric field (b), and light (c). (d-f) images of structures assembled using the methods depicted on panels (a-c), respectively.[145]

1.4. Ordered nanostructures

Controlled clustering as a means of achieving well-organized NP arrays is a topic of extensive research in materials science. Formation of secondary structures is desirable owing to the potential of obtaining unique materials. Such novel composites may exhibit both, properties derived from the individual constituents of the system, as well as original collective qualities resulting from the NP-NP interactions.[146] Unprecedented optic, magnetic and electronic properties can emerge in NP arrays, as a consequence of the interaction between the NPs' surface plasmons, magnetic moments or excitons.[145] Exploitation of such features in functional devices should be possible provided sufficient control over the interparticle spacing (periodicity of the nanostructure) and NP arrangement is assured.

The arrangement of NPs within an ordered nanostructure is determined by both external parameters, such as fabrication conditions (temperature, humidity), as well as the intrinsic properties of NPs. In particular, the NP size distribution along with NP-substrate and NP-NP interactions have a dominant influence on the organization.[147]

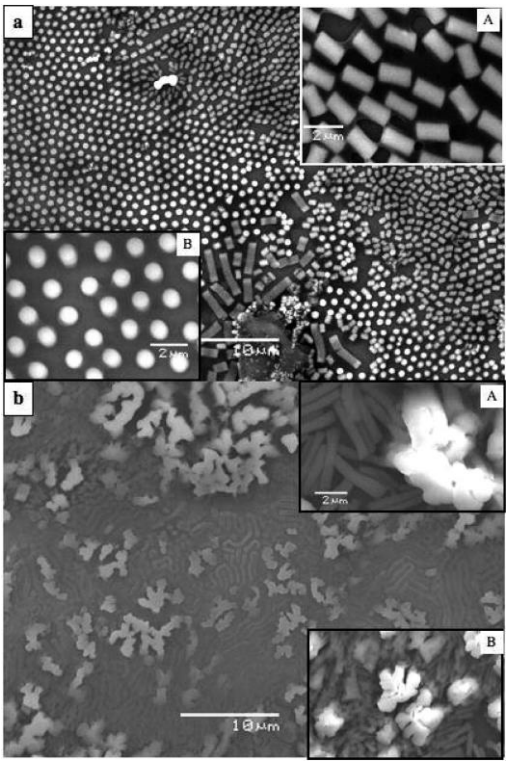

Fig. 17. SEM patterns of mesostructures of 5.7 nm cobalt nanocrystals having 13% (a) and 18% (b) size distributions.[147]

Ordered structures are formed in case of sufficiently narrow size distribution and attractive interaction between the constituents of the structure. In case of high size distribution structural defects appear. The cohesive forces within the array are not potent enough to guarantee long-range homogeneous ordering. The obtained shape of the assembled mesostructured in turn dictates the physical properties of the lattice.[147] Since a directional dependence of dipolar forces exists the arrangement of NPs within the assemble will influence the dipolar interactions, and in consequence the properties of the structure.

Organized nanostructures

It is known that properties of NP–based materials depend not only on their size, shape and composition, but also to a large extent on the spatial organization of NPs building blocks with respect to one another.[148] Therefore, well-defined nanostructures are of high interest in materials science, as structures with novel, unprecedented features. Depending on the number of dimensions below 100 nm of a nanostructure it may be categorized as zero-dimensional (0D, e.g. NPs), one-dimensional (1D, e.g. nanotubes), two-dimensional (2D, e.g. nanofilms), three-dimensional (3D, polymer-based nanocomposites). The 0D nanostrucutres were discussed briefly in section 1.2. Below, a concise description of structures of higher dimensionality is presented.

1.4.1. One-dimensional nanostructures

1D nanostructures possess both dimensions perpendicular to the longitudinal direction confined below 100 nm. In the third direction the structure may have much larger dimensions, providing the material with certain bulk properties.[149] Such structures include nanowires, nanofibers, nanorods, nanobelts, and nanotubes.

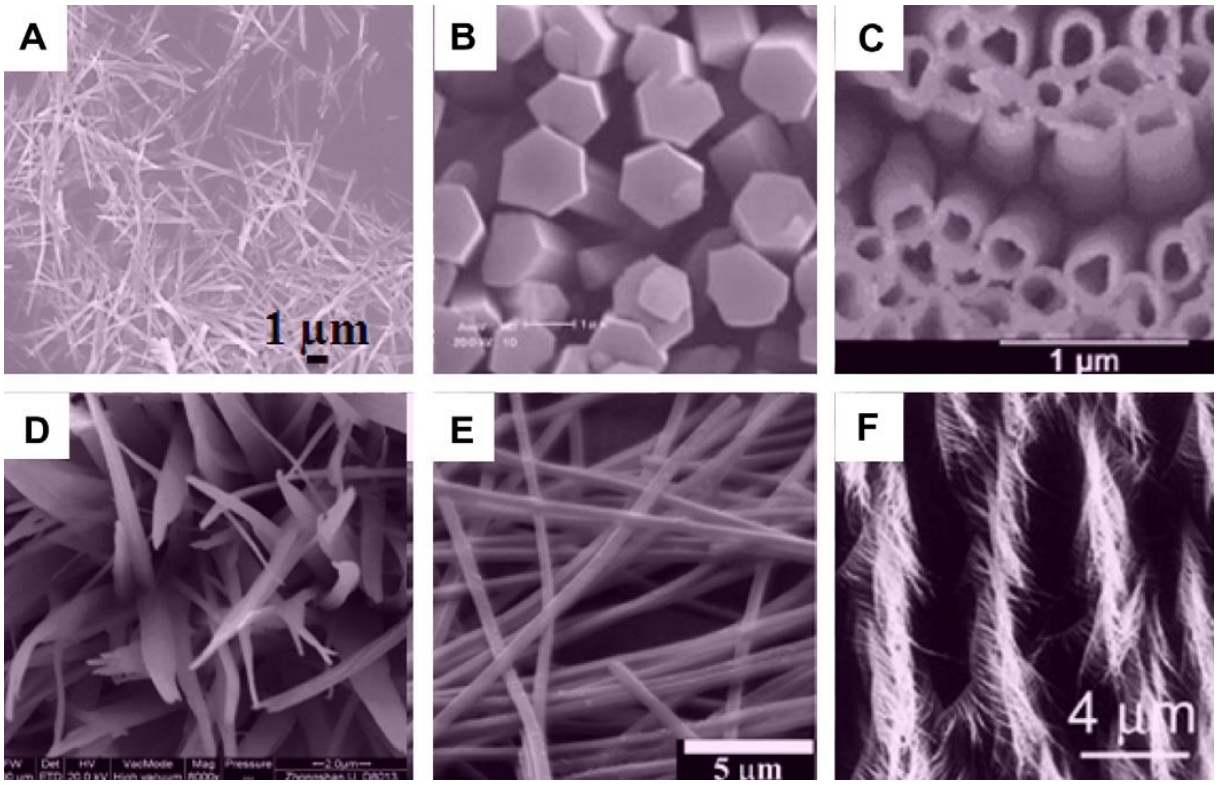

Fig. 18. Typical SEM and TEM images of 1D nanostructures: nanowires (a), nanorods (b), nanotubes (c), nanobelts (d), nanoribbons (e), and hierarchical nanostructures (f).[113]

1D nanostrucutres possess several advantages, potentially significant in practical applications. These include good dispersion, size and shape uniformity, predefined electrical conductivity, as well as high impact resistance.[150, 151] Unique properties of 1D nanostructures are derived from their high aspect ratios, large specific surface areas and structural confinement in two dimensions. These features influence their mechanical, chemical, optic and electric properties. Extraordinary mechanical properties are often observed in single crystalline 1D nanostructures, where the strength, stiffness and toughness may approximate the values predicted for perfect crystals.[17] The reduction of the defect number per unit length is accountable for the described superior properties. Due to their specific geometry 1D nanostructures may be considered as electron transport channels or interconnects. For example carbon nanotubes exhibit excellent conductivity, attributed to the ballistic transport of electrons over long tube length. In metallic nanowires on the other hand a metal-to-semiconductor transition may be observed when decreasing the nanowire's diameter. This is attributed to the opening-up of the band-gap as a result of the quantum confinement.[152] The quantum confinement effect also influences strongly the optical properties of 1D

nanostructures. For example a substantial blue-shift of absorption and band-edge emission peaks is observed as the diameter of semiconducting nanowires approaches the Bohr radius of the corresponding materials.[153, 154] Finally, the magnetic properties of 1D nanostructures are affected by the reduction of their size. Enhancement of magnetic properties or their induction in non-magnetic materials has been observed.[155, 156] High coercivity fields that are inversely proportional to the nanowire diameter can be noted.

Although the 1D nanostructures possess unique properties, their potential cannot be fully utilized until their uniform orientation is achieved. Controlled organization of 1D units is a desired route towards fabrication of 2D and 3D ordered networks.[157] Alignment of 1D nanoobjects can lead to superior properties, not found in disordered structures.[158] Moreover, covalent connection of the 1D building blocks can greatly alter the mechanical, electronic and porosity properties of the isolated 1D units.[157] As a result hierarchical organized 1D nanostructures that form networks of higher dimensionality may be potentially suitable for such applications as field-effect transistors (FETs),[159] light-emitting diodes (LEDs),[160] solar cells (SCs) [161] or sensors.[162]

1.4.2. Two-dimensional nanostructures

Two-dimensional nanostructures are assemblies of nanoobjects where two dimensions are not within the nanometric size range.[113] Due to their unique geometry 2D nanostructures may exhibit noteworthy shape-dependent properties. A single layer of graphene may serve as a fine example of a 2D monolayer structure. This structure, made up of a continuous hexagonal network of linked sp^2 carbon atoms, displays extraordinary electronic transport properties.[163] Similarly, thin-film nanoparticle (NP) membranes are promising nanostructured materials that may find numerous applications including electric, magnetic, and photonic sensors and devices,[164, 165] due to their unique characteristics. Extensive effort is nowadays put in to developing new methods of organizing nanoscopic objects into controlled architectures.[166] Such nanostructures are typically formed in solution, at liquid-liquid interfaces or on solid supports via specific adsorption or self-assembly techniques.[166] Self-assembled monolayers (SAMs) made of NPs can serve as an demonstrative example of a 2D nanostructure. Such structures are assembled at liquid-air interfaces, and later transferred onto solid substrates.[167] Tuning of the spatial organization of NPs within an array allows

for fine control of the produced materials' properties, which are different from both, those of individual NPs, as well as bulk materials.[167]

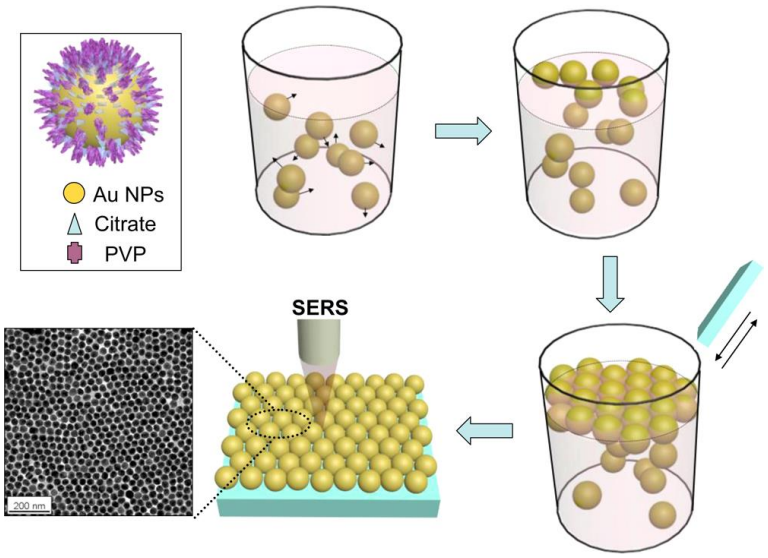

Fig. 19. Scheme illustrating the self-assembly of AuNPs at the air/water interface and the TEM image of the monolayer film, after its transferal onto a solid substrate.[167]

The collective properties of an NP 2D lattice can be altered by changing of the physical parameters, such as NP size, interparticle spacing. Importantly, the possibility of independent tuning of the metallic cores and organic capping agents broadens considerably the scope of adjustable film properties.[168]

Supported and free-standing films can be distinguished amongst both, monolayer and multilayer NP membranes. The supported NP arrays have been previously fabricated via adsorption on surface-modified solids, having an increased affinity for NP binding. Importantly, in this case some properties of the NPs may be altered after their deposition on substrates. The influence of a dielectric support in the vicinity of an individual metallic NP on its properties has been previously demonstrated experimentally.[169] The substrate modifies the energies of the NP's plasmon modes, inducing a significant energy splitting. In free-standing films on the other hand the influence of supports is nonexistent.

A commonly used technique for multilayer NP film fabrication is the Layer-by-Layer deposition method, reported first for inorganic colloidal particles by Iler.[170] Multilayer nanostructures assembled by successive deposition of single layers may possess a high degree of order. The properties of nanostructures are altered when the number of NP layers increases

within the 2D structure. The evolution of a 2D nanomaterial's properties has been studied [171] during gradual stacking of surplus NP monolayers to afford finally a material made of 15 layers. It was observed that initially the conductance of the material increases, from monolayer to multilayers. However, at 4-5 layers, when the transition of dimensionality from 2D to 3D occurs, the conductance starts to level off. This example illustrates the influence of the presence of multiple layers within a 2D structure. The properties of the nanostructure may be altered significantly as a result of the addition of extra layers. Another example of this phenomenon is the variation of mechanical characteristics observed upon crossing over from mono- to multilayers of NPs. The effective net fracture strength, being the stress at which a material fails via fracture, decreases with increasing of the NP layer number.[168] This has been explained by the uneven distribution of stress amongst individual layers within a multilayer material. Subsequent layers take up proportionally less stress than the first layer upon fracture.[168]

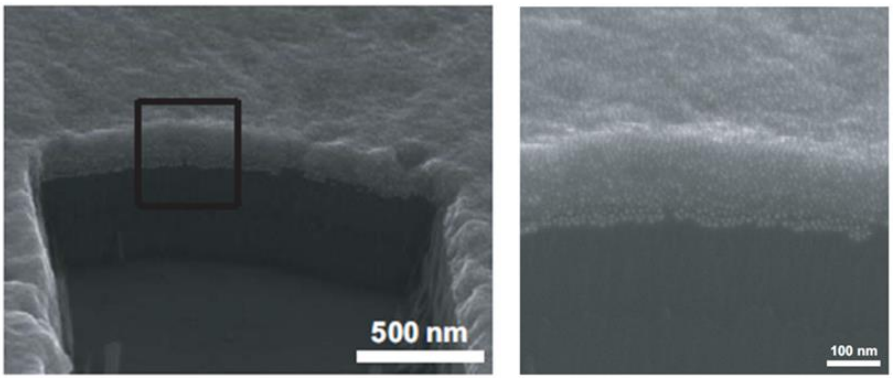

Fig. 20. Example of a multilayer nanostructure, obtained by gradual addition of surplus NP layers, one monolayer at a time.[171]

Monolayers of NPs are of particular interest in such fields as nanoelectronics [166, 172, 173] and catalysis.[174] Such monolayer films may display extraordinary features, such as an elevated mechanical resistance, manifested by a Young's moduli of up to several GPa.[168] They are also the object of fundamental studies[175] because in ordered arrays of NPs coupling interactions between the adjacent NPs affect the electric, magnetic, and optical properties of the formed nanostructures.[176, 177] Free-standing membranes consisting of covalently bound nanoparticle multilayers have been reported previously.[178, 179]

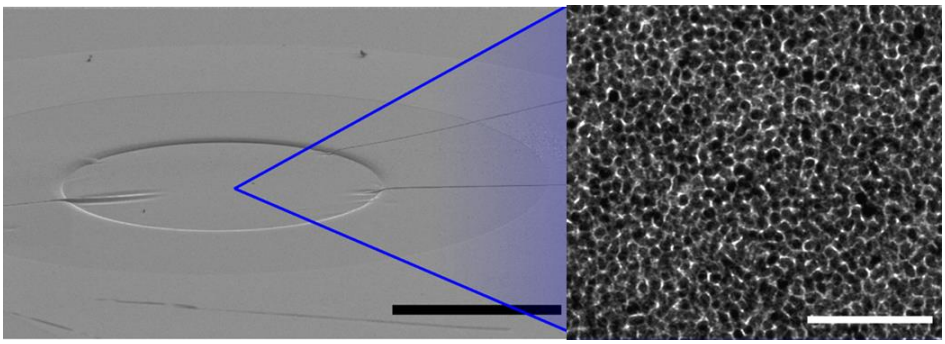

Fig. 21. SEM and TEM images of a free-standing cross-linked AuNP multilayer membrane spanning the cylindrical cavity of an electrostatic actuator. Scale bars: 100 μm and 50 nm, respectively.[178]

Although such membranes are characterized by excellent mechanical properties they possess important disadvantages compared to monolayer structures. Namely, it is expected, in contrary to thick multilayer films,[180] that in nanoscopic monolayers much control over the NP assembly and interparticle spacing can be achieved. It means that covalently bound monolayer NP films can form a flat structure of well-defined thickness. Also, within the monolayer, the NPs can be linked with molecules possessing tailored properties. That is, the monolayer films have the form of two-dimensional networks composed of well-defined NP-linker-NP building blocks. In such systems interactions between the NPs (including transfer of electrical charge) are mediated by the linker molecules. This makes the free-standing monolayer film an excellent system for investigating fundamental phenomena in the nanoscale and a promising material for a variety of applications. For this reason, fabrication of monolayers of interconnected NPs has attracted much attention in the scientific community in recent years.[181-189] However, difficulties in obtaining stable films, in which the NPs are permanently connected to one another, has hindered their widespread applications. Fabrication of membranes stabilized by noncovalent interactions like the ligand-core or ligand-ligand attraction has been reported in literature.[180, 190-192] Examples include application of host-guest chemistry [193] and non-specific DNA-DNA interactions.[194] Such membranes, however, neither have been cross-linked nor embedded in a polymer matrix, hence are rather unstable and could be easily disrupted, since the existing interactions are quite weak (electrostatic and Van der Waals forces, hydrogen bonds). Other methods lead to a fusion of the neighboring NPs and formation of aggregates within the monolayer,[195, 196] giving rise to semi-continuous networks instead of arrays of separated NPs. NP aggregation strongly hinders the NP film formation process due to the occurrence of

hampering of NP spontaneous ordering in case of NPs with a broad size distribution.[167] Moreover, aggregation hinders NP sorption at interfaces, which may significantly obscure the fabrication of films.[167] Chemical cross-linking of the membranes is the way to stabilize the NP assemblies and prevent their aggregation. Two reports on chemically cross-linked membranes have been published to date. Russell and co-workers have synthesized free-floating cross-linked CdSe NP films, which possessed the morphology of crumpled sheets.[197]

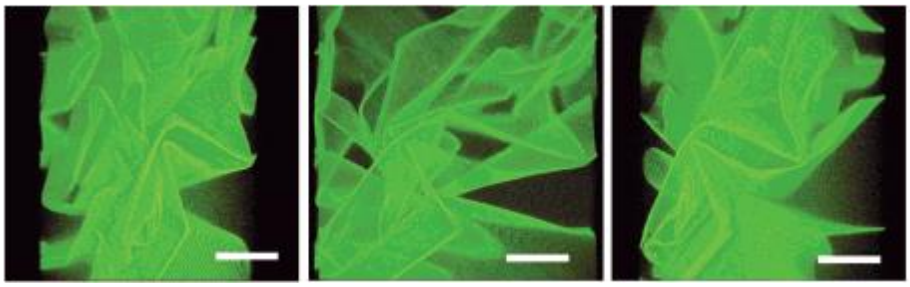

Fig. 22. Confocal microscope image of a cross-linked NP sheet. Scale bar: 50 μm.[197]

The obtained membranes were suspended in toluene, and the authors did not make an attempt to remove the film out of the liquid phase to obtain a free-standing film. Sanders *et al.* has prepared a cross-linked NP network at the liquid-air interface using the Langmuir-Blodgett trough by employing dithiol molecules as the cross-linking agent.[198] Although the obtained films could be easily transferred onto solid substrates, free-standing films in air have not been reported prior to the findings of the research presented herein.[199]

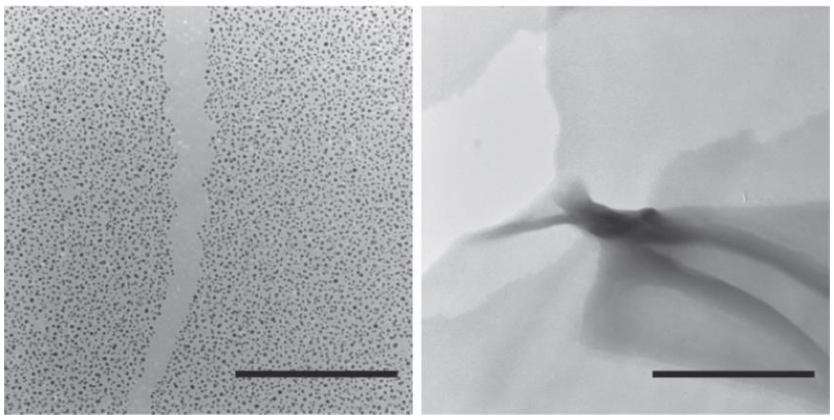

Fig. 23. Images of cross-linked film, made of hexanethiol-capped AuNPs. Symmetric tears and folding of the film indicate membrane-like quality.[198] Scale bars: 300nm and 1μm, respectively.

An interface between two liquid phases provides a suitable template for the fabrication of ordered NP structures. This is because NPs adsorbed at the fluid-fluid interface are highly mobile and can readily arrange into various equilibrium assemblies.[200] As a result, a fairly good control over the nanostructures synthesized in such a way is attainable.[135, 138, 141, 190, 197, 201-205] What is also important, chemical compounds, like cross-linking agents, can be easily introduced into the system thorough either phase. Interfacial fabrication seems thus to be a technique that holds great promise for the synthesis of the monolayer film of NPs.

1.4.3. Three-dimenasional nanostructures

Many important applications of 3D nanostructured materials require exact organization of their components into well-defined hierarchical architectures.[206] The relative position of individual constituents within the nanomaterials' structure is one of the factors determining the properties of the material. Through appropriate selection of component chemical structure, material synthesis parameters and fabrication method the required control may be achieved, affording materials with precisely programmed structures and properties.

Combining NPs with natural or synthetic polymer matrix opens a path to obtaining novel nanocomposite materials that possess advantageous qualities. Properties of such materials – obtained either via incorporation of the NPs into the matrix or in situ synthesis of the NPs within the matrix – are determined by a combination of many factors, such as the chemical composition, density, shape, arrangement of the inclusions, as well as the constitutive properties of the host material.[207] Incorporation of NPs into polymeric matrices often gives rise to substantial improvement in the mechanical,[208] thermal,[209] and electrical [210] properties of the host material. Strategies employed currently for the incorporation of the NPs into polymer matrix involve either in-situ or ex-situ synthesis of the NPs.[211, 212] The NPs can be embedded in the bulk of the polymer matrix, which is a typical situation when the NPs are formed in-situ simultaneously with the matrix, or bound on or near the surface, which occurs when the NPs are synthesized ex-situ or in-situ after the formation of the matrix.

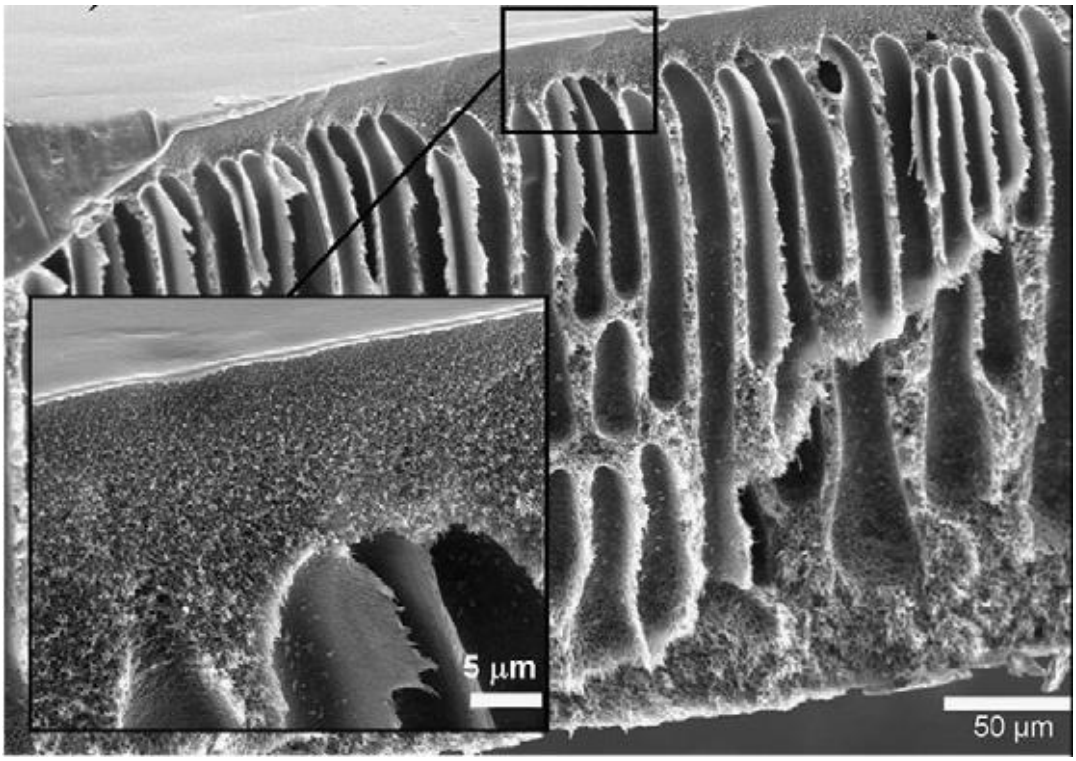

Fig. 24. Cross-section SEM image of a polysulfone composite with silver NPs incorporated. A representative example showing the distribution of NPs within the matrix.[211]

The main drawback of the in-situ method is the possible influence of byproducts or unreacted substrates, which are not removed after the synthesis, on the nanocomposite properties.[213] Moreover, the unique properties of the NPs strongly depend on their size, shape, and surface chemistry.[85, 214, 215] Thus, preparation of monodispersed NPs of well-defined properties is crucial for the fabrication of nanocomposites with tailored characteristics. This issue is of extreme importance in applications such as catalysis, where the shape and size of the NPs determine their catalytic activity.[216, 217] In this respect, the ex-situ approach provides a better control over the synthesis of the NPs and allows for the transfer of the size dependent features of the NPs into the nanocomposite property profile.

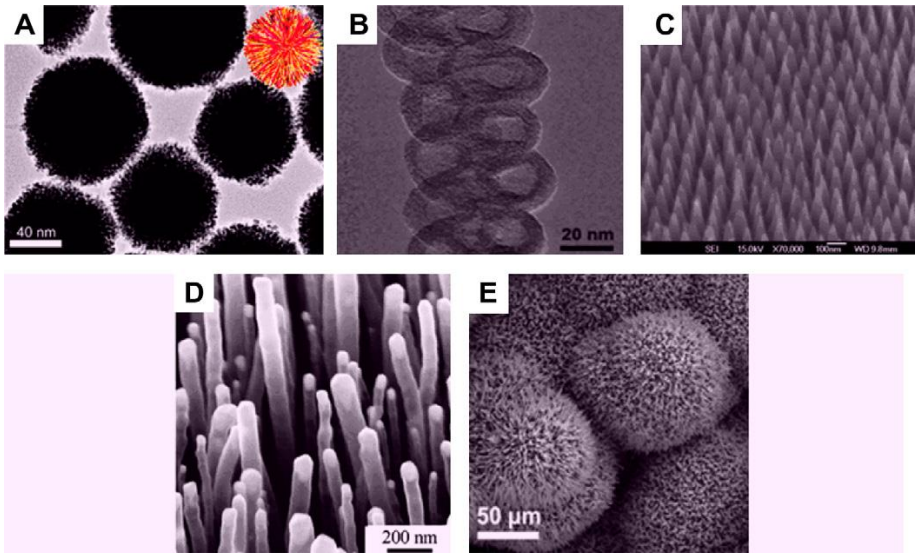

Fig. 25. Typical SEM and TEM images of 3D nanostrucutres: nanoballs (dendritic strucutres) (a), nanocoils (b), nanocoils (c), nanopillers (d), and nanoflowers (e).[113]

The binding manner of the NPs to the matrix also has a significant impact on the properties of the composite material. Strong chemical bonding of the NPs is highly advantageous over weak linkage, since it provides means for permanent attachment of the NPs to the polymer, which prevents their leaching from the composite. The immobilization of the NPs within the host is important not only because it makes the material far more resistant and durable, but also due to the raising concerns about the influence of the NPs on the environment, and the health risks associated with their release.[218] Better fixation of the NPs within nanocomposites is one of the approaches employed to the reduction of hazards associated with the release of NPs.[219] Robust bonding, that prevents the NP leaching, is of high importance in some of the new applications of the nanocomposites in medicine, like for example, the fabrication of bactericidal materials,[220, 221] surgical equipment, medical implants,[222] and biosensors. Such composites are designed to have contact with living organisms making low cytotoxicity a crucial requirement. The reduced cytotoxicity is achieved by the immobilization of the NPs on a substrate, which strongly hinders their uptake by the cells.

In typical fabrication strategies, the NPs are weakly bound to the matrix via hydrogen[223] or coordination bonds,[224] electronic,[225] or electrostatic attraction between the polymer and the functionalized NPs.[226] So far, there are very few reports on methods allowing chemical (covalent) bonding of the NPs to the host.[227, 228] These methods utilize chemically

modified matrices, where the surface of the matrix contains functional groups of high affinity that act as anchors for the in-situ synthesized NPs.[227] However, the above approach is not robust because it relies on specific chemical reaction and requires selection of the reaction conditions for each type of the polymer host employed. Recently, a novel approach to the fabrication of nanocomposite containing covalently bonded ex-situ synthesized NPs has been reported.[228] In the work cited, the reaction of formation of the covalent bonds proceeds through radical generation, and is initiated by the UV irradiation. Radical reactions are, however, known to proceed rapidly, in a way that is difficult to control. Grafting polymers from the surface of NPs is also an interesting approach, in which surface-modification of NPs with groups capable of initiating polymerization is employed.[229] Nonetheless, this process may be difficult to control if two reactive radicals are formed from one initiating molecule. The polymerization may then proceed both on the surface of the NPs and in the bulk. Controlled radical polymerization is a solution, but high concentrations of transition-metal catalysts are required in this case. These metals contaminate the final product and their recovery is difficult. The so-called "grafting from" methods of covalent attachment include grafting the surface of nanofillers with polymerizable groups, which may be used to obtain both linear and cross-linked composites.[229] However, due to the interaction of the polymerizing agents with other molecules that may be present in the system control over the final product is difficult. A more common approach is the "grafting to" method, where already synthesized polymers with appropriate reactive end groups are chemically attached to the surface of nanofillers.

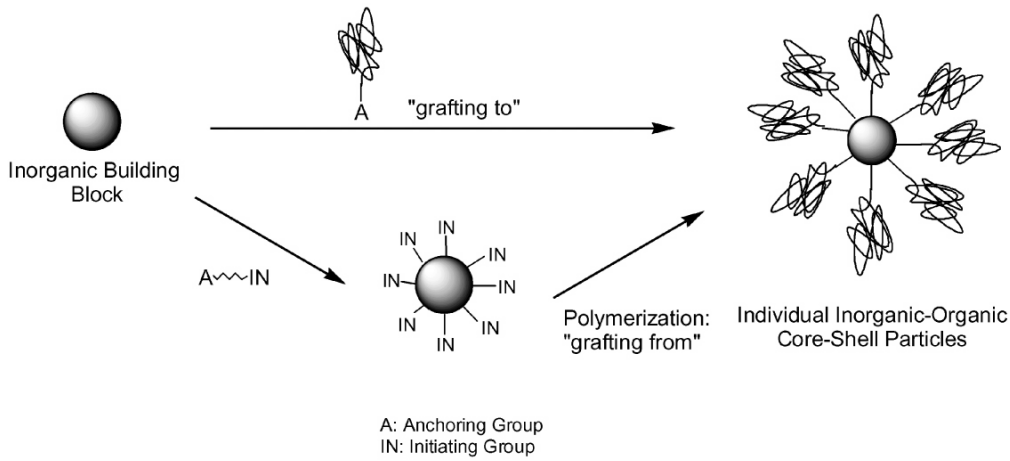

Fig. 26. Scheme comparing the concept of "grafting from" and "grafting to" between polymers and the surface of inorganic fillers.[229]

A significant advantage of the chemically bound NPs is their lack of tendency towards aggregation in the immobilized state, which may occur due to low compatibility between the NPs and the polymer matrix.[230] The aggregation of the NPs is undesired because it can impair functionality of the composite.[220, 230, 231] The high surface area of nanoobjects makes them prone to aggregation at high concentrations,[232] which may influence significantly the material properties.[233] Above a certain amount of nanometer-sized additives the advantageous influence derived from their presence is no longer observed, as a result of the aggregation process. Since the key to utilizing the advantageous effects of nanofillers on the properties of nanocomposites is their uniform dispersion in matrices, the development of a method allowing for the synthesis of materials with homogeneous dispersion of the NPs is highly desirable. Functionalization of NP surface with ligands that enhance the compatibility between the NPs and matrix is a recently reported strategy that inhibits agglomeration of NPs.[234] However, the weak character of the interaction between the NPs and polymeric matrix does not guarantee durability of the obtained nanocomposite. Thus, strong enough attractive interaction between the NPs and polymer must be provided to prevent the aggregation. For this reason, covalent bond formation between the NPs and the polymer matrix are desirable[235] for fabrication of highly-loaded nanocomposites. The formation of strong covalent bonds allows for a much better control over the loading of the NPs into the obtained composites, which may influence significantly the material properties.[104]

Nanocomposites are also widely utilized in thin film production. Thin polymer films are important in many applications, such as electronic packaging[102] and nonlinear optical devices.[236] It has been reported that the addition of nanofillers to polymers may prevent or significantly retard the dewetting of substrates, making fabrication of stable and homogeneous polymer films possible. Though compatibility of the polymer and NPs is key in this process. The attractive interaction between the two components must be strong enough to prevent the aggregation of the NPs.

Another promising strategy for complex 3D nanostructure construction is the use of 2D materials as building blocks. This strategy encompasses combining the 2D materials with other functional materials to form hybrid nanocomposites. New properties often emerge in such hybrid nanostructures aside from the characteristics of individual components.[237]

Three main strategies for such 3D hybrid materials fabrication can be distinguished. Either separate 2D materials are stacked together or the 2D component is combined with materials of a different dimensionality (1D or 3D). In the latter case the 2D materials may be used as both the templating structure or as the material deposited on a template formed by the partner material.[237] The formation of hierarchical 3D architectures requires the organization of 2D materials into spatially well-defined configurations.[238] Preserving the unique properties of 2D structures within the 3D architectures remains a challenge. Inhibition of the 2D material Layer-by-Layer restacking is essential. Such 3D structures possess hierarchical order with structural features at different length scales. These features impart specific characteristics of these materials.[238]

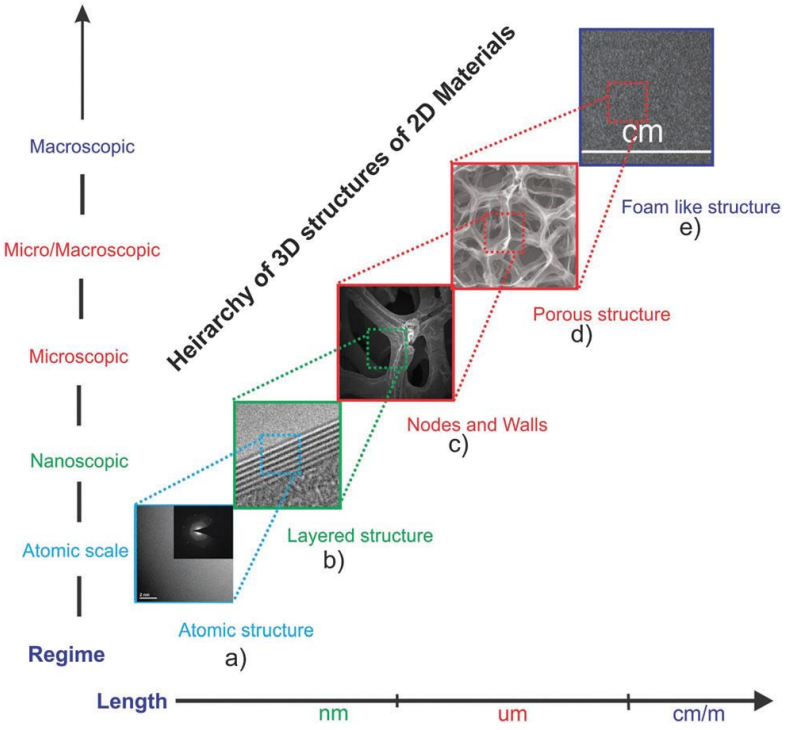

Fig. 27. Hierarchy of a 3D structure of 2D materials (with the example of graphene).[238]

1.4.4. Properties of self-assembled nanostructures

Plasmon coupling derived properties

Coupling between surface plasmons of adjacent NPs may occur when the NPs are in close proximity. The strength of this electromagnetic coupling is determined by the NP spacing and medium dielectric constant. Hence, spatial arrangement of NPs within the nanostructure

affects strongly its interaction with light. The geometry of the NP assembly determines the assemblies' plasmon band position. Red-shifting of the resonant wavelength peak is observed in closely-packed nanostructures due to near-field coupling.[239] For instance plasmonic coupling observed as a red-shift and broadening of the extinction spectra peak was reported in a honeycomb NP structure once the NPs were positioned so as to form a spatially crowded array.[240] In another study tailoring of the plasmon coupling was executed in a 1D NP array by controlled variation of the interparticle gap width.[241] A nonlocal or quantum-mechanical mechanism of coupling is suggested due to the observed decrease of coupling strength at NP separations below 0.5 nm. It was determined that the magnitude of the shift is related to the particle spacing and is correlated by a inversely proportional exponential dependency [239].

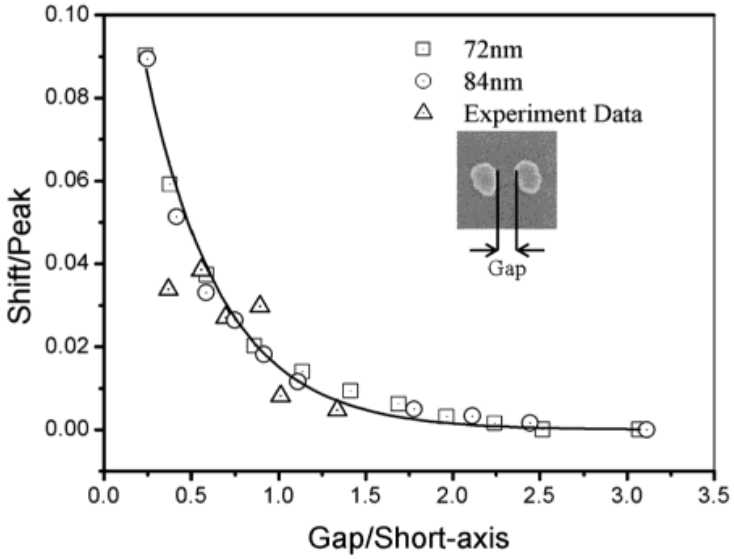

Fig. 28. Comparison of computer-simulated (○ and □) and experimentally measured resonant wavelength shifts as a function of the gap between two particles.[239]

This shift is relevant at distances smaller than 2.5 times the particle short-axis length. Further control over the optical properties of nanostructures is accessible in assemblies of anisotropic in shape nanoobjects.[242] The existence of two distinct assembly manners (i.e. end-to-end and side-by-side) offers the possibility of optical response alternation depending on the orientation mode.

Exciton coupling derived properties

When considering semiconducting NPs two coupling mechanisms can be distinguished – the Dexter transfer (where electron exchange transfer occurs) and the Förster resonance energy transfer (FRET). Dexter transfer is predominantly observed in case of NPs with small sizes packed in a dense manner. This mechanism of coupling results in a photoluminescence emission and adsorption bands redshift.[243]

The efficiency of the FRET mechanism is strongly distance dependent, hence the transfer of energy from an excited donor to an acceptor occurs at distances smaller than the critical Förster radius [244] (usually between 2-10 nm). The excitation energy of an electron is transferred via an induced-dipole movement interaction,[245] from a smaller NP to a larger one, in the direction of the reduced energy gap.[246] A prerequisite for this process is the spectral overlap of donor emission and acceptor absorption bands,[247] as well as appropriate band gap energy difference. The Förster energy can be cascaded in the targeted direction, as depicted in Fig. 29., from smaller NPs in the outer layer to the larger ones in the inner layer, and finally to nanowires.[145]

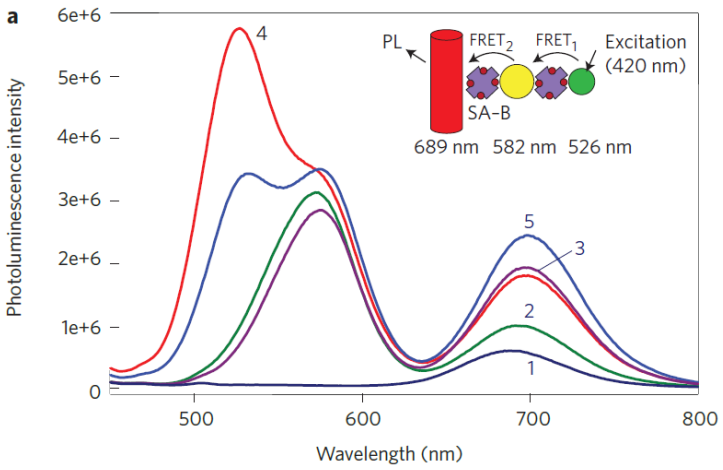

Fig. 29. Illustration of coupling between NPs. Variation in the intensity of photoluminescence from a CdSe nanowire in self-assembled nanostructures comprising of CdSe nanowires, 3.2 nm and 4.1 nm CdSe NPs, at different times. 1) immediately after adding the 4.1 nm CdSe NPs 2) 21 min after adding the 4.1 nm CdSe NPs 3) immediately after adding the 3.2 nm CdSe NPs 4) 30 min after adding the 3.2 nm CdSe NPs.[145]

The FRET process may cause a redshift of the photoluminescence band, quenching of luminescence quantum yield of the donor coupled with an enhancement of luminescence quantum yield of the acceptor,[248] and an accelerated decay of photoluminescence emission.[145]

Magnetic coupling derived properties

Collective magnetic properties of NP arrays are dependent on the ordering within the nanostructure. When NPs form densely packed arrangements an increase in their magnetic interactions can be observed. A structure-dependent magnetization curve was observed in dense films of assembled maghemite nanocrystals due to dipolar interactions between particles. For large coupling considerable changes in the hysteresis loop and coercivity were noted.[249] These changes were assigned to the variation in the anisotropy of the organized structure. Similarly the coercivity field, H_c, being the field at which all spins within the sample become disordered, depends on the arrangement of the structure. Values of H_c are larger in case of well-defined structures, as compared to disordered ones.[147] Other magnetic properties, such as the remaining spin organization of the sample after the external field removal, i.e. remanence, can display a strong reliance on the structure arrangement. A clear dependency between the value of remanence and the structure ordering was observed in case of γ-Fe_2O_3 NP 1D (wires) and two dimensional (2-D) assemblies (films). A distinct directional dependence was observed only in case of the 1D structure, where a change of the registered magnetization curves occurs depending on the direction of the applied field. A directional effect of structure has been theoretically predicted previously in linear chains of NPs, when the magnetization is measured along the chains direction.[250]

Plasmon-exciton interaction derived properties

Interaction between excitons and plasmons occurs between semiconductor and metal NPs assembled into superstructures. The semiconductor component is the quantum emitter, whereas the metallic one is the amplifier or damper. Emission of semiconductor NPs is increased in the presence of metallic NPs in two cases – when the optical adsorption is enhanced, and when the emission process is amplified. The amplification of the electric field inside a complex leads to an increase of semiconductor NPs emission in the presence of metallic NPs.[251] The presence of a metal can modify strongly the light-emission and

adsorption properties of semiconductor NPs. Hence, the optical properties of superstructures comprising of both, semiconductor and metallic NPs, are strongly altered as compared to single NPs. The intensity of photoluminescence of the semiconducting NPs depends on the emission, adsorption and energy dissipation rates in the complex,[251] which in turn depend on the structure assembly. The optical response of such structures are highly sensitive to both the size and the interparticle spacing of metallic NPs.

2. Experimental section

2.1. Structure analysis techniques

2.1.1. Nuclear Magnetic Resonance

The Nuclear Magnetic Resonance (NMR) spectroscopy is a useful tool in structure analysis of chemical compounds. This technique provides detailed information concerning the structure, reaction state, dynamics, as well as chemical environment of the studied molecules. It relies on the phenomenon of nuclear magnetic resonance, being a physical occurrence involving the adsorption and re-emission of electromagnetic radiation. A prerequisite for the application of this method is the presence of nuclei that manifest magnetic dipoles within the investigated structure.[252] An external magnetic field will cause the nuclei's magnetic dipole alignment relative to the field in quantum mechanically limited spin states (orientations). Spin states have identical potential energy in the absence of the external magnetic field, but will differentiate when a field is applied. The difference in energy between these spin states increases with the increase of the strength of the field. For the necessary magnetic field generation superconducting magnets immersed in liquid helium are utilized. Electromagnetic radiation may interact with the described entities possessing a series of states of different energy.[253] Photons of a frequency in the radio region will cause bridging of the adjacent levels, provided that their energy matches exactly the frequency at which the nuclei precesses (this is the so-called resonance frequency). Excitation of the nuclei will then occur through the promotion of spin states. The excited nuclei relax back to the lower spin states by re-emission of the excess energy or via its transferal to an appropriate acceptor, such as polar solvent molecule.[252] Importantly, the resonance frequency is altered by the intramolecular magnetic field prevailing around an atom in a molecule. This field, derived from the presence of electrons in a molecule, influences the magnetic field acting on the nucleus, making it inequivalent to the applied field. Thus the applied field is perturbed by a secondary magnetic field, arising in the presence of the external magnetic field. The secondary field strength depends on the structure of the molecule having the analyzed nucleus, and it originates from the motion of the molecule's electron cloud. The existence of this field causes the reduction of the nuclear frequency. Therefore screening of the nucleus from the applied field by its

electrons occurs.[253] This dependence provides information about the electronic structure of a molecule and its individual functional groups, as atoms with identical magnetic moments will have resonant signals at different frequency values, due to differing electronic environments of each nucleus within the studied molecule. Identification of structural properties of compounds is therefore possible.

2.1.2. UV-Vis absorption spectroscopy

Optical spectroscopy is based on the relationship between discrete atomic or molecular energy states E_i and the frequency ν of electromagnetic radiation, which can be written in the following form: $\Delta E = h\nu$, where ΔE is the energy difference of energy states of an atom or molecule. UV-vis spectroscopy is of special interest as the frequencies of electromagnetic radiation in the ultraviolet and visible regions correspond to the energy differences of atomic and molecular electronic states.[254] The theoretical basis of measurements in the UV-vis region is derived from the Bouguer-Lambert-Beer law, which states that the absorbance A_ν is directly proportional to the concentration of the light-absorbing substance, c, and the path length of the sample, d, where the molar extinction coefficient, ε_ν, is the proportionality coefficient: $A_\nu = \varepsilon_\nu\, c\, d$. The amount of absorbed light is the difference between the incident radiation (I_0) and the transmitted radiation (I) during passing of the light through a sample. The mentioned relation can be applied only to dilute solutions, as in such conditions ε is constant. In concentrated mixtures ε depends on the solution's refractive index,[255] making this law inadequate. When a photon with an energy matched to the energy difference of the molecule energetic levels, is absorbed a transition between the molecule's energy levels is triggered.

To obtain a UV-vis spectrum the amount of absorbed radiation is measured at each wavelength during sample irradiation, and the intensity of absorption is plotted against the wavelength or frequency of the absorbed light. Concentration of the absorbing species is indicated by the absorbance intensity, whereas the position of the absorption band maximum is a measure of the energy levels difference involved in the transition.

On the metal boundary quantized oscillations of surface charge, called surface plasmons, occur in the presence of an external electric field. In case of metallic NPs a resonance mode with an optically active dipole field configuration exists. When the frequency of a photon of

the incident light is in approximation equal to the frequency of the collective oscillation of conduction electrons at the surface then resonant absorption may occur.[88] Due to this a strong absorption band in the UV-vis region is observed in case of metallic NPs, as opposed to bulk metals. The value of the resonance frequency is dependent on the surrounding medium and adsorbed solutes, as well as such NP parameters as size and shape.

As a consequence of this dependence, UV-vis absorption spectroscopy is also commonly employed to calculate the size distributions of NPs. In case of spherical particles, this spectroscopic method allows for the calculation of size distribution and concentration of the nanoobjects, such as AuNPs.[134, 145, 240] This spectroscopic approach is based on the Mie theory [241] and its modifications [256] that require detailed information about dielectric properties of the solvent, structure of the AuNPs surface coating, surface charge, and interparticle interactions. The lack of this information may lead to unreliable results. Establishing of the correlation between the particle diameter and the extinction efficiency allows for the determination of NP concentration, where the extinction efficiency is closely related to the extinction cross section of a spherical particle with a radius *R* in a dielectric medium.[256] Particles with fairly large sizes may be measured using the UV-vis spectroscopy.[145] For objects with a radius less than ~10 nm it allows only for a rough estimation of their sizes. Moreover, when the AuNPs possess non-spherical shapes application of the Mie theory becomes problematic and a reliable calculation of the total volume of gold clusters in the sample is impossible.

2.1.3. Infra-Red absorption spectroscopy

Electronic transitions are not induced by Infra-Red (IR) radiation, as the energy in this region is lower than the electronic level differences. IR radiation may cause excitation of the vibrational and rotational states. Infrared spectroscopy involves the analysis of the IR radiation interaction with molecules, wherein the photon energy causes a change of the molecules' vibrational state.[257] Vibrations are construed as stretching and bending movements of atoms within the structure relatively to one another, whereas rotations involve spinning around a given axis. Symmetrical and asymmetric bond stretching can be observed, however only vibrations causing a change in the molecule's dipole moment will give rise to the absorption of IR radiation.[258] Radiation absorption induced transitions between

molecular vibrational energy levels are measured in IR spectroscopy. The IR spectrum allows for a "fingerprint" identification of a sample since the vibrational energy levels are characteristic for a given molecule.[257] This arises from the dependency of vibrational frequencies of the analyzed molecule on the masses of atoms, their geometric arrangements, as well as bond strengths. The Lambert-Beer law describes the relationship between the intensities of the incident and transmitted IR radiation and the analyte concentration. An IR spectrum is the absorbance (or transmittance) intensity plotted as a function of the wavelength, λ, which is proportional to the energy difference of the ground and excited vibrational states. A resonance condition exists for the absorbance of IR radiation. Absorbance of radiation occurs provided its frequency matches the frequency of a particular normal mode of vibration. Moreover, the transferal of photon energy to the molecule takes place only on condition that a net change in the molecule's dipole moment occurs as a result of its vibrations or rotations.[258] Only molecules fulfilling this requirement are IR active. This condition may be mathematically formulated as

$$\left(\frac{\delta\mu}{\delta Q}\right) \neq 0\,,$$

where the change in the dipole moment μ, with respect to a change in the vibrational amplitude, Q, is greater than zero. The dipole moment of a molecule, μ, is defined as the sum of ratios of the magnitude of the atomic changes (e_i) and their positions (r_i): $\mu = \Sigma\, e_i \cdot r_i$. The interpretation of the obtained IR spectra is greatly simplified since vibrations of certain groups of atoms, such as those in functional groups, are mechanically independent from the rest of the structure. Hence, these group vibrations possess a characteristic frequency, independent of the molecule's structure.

2.1.4. Dynamic Light Scattering

The dynamic light scattering (DLS) technique involves measurement of Brownian motion of particles for the determination of their size. Brownian motions of particles suspended in a liquid result from the constantly occurring random collisions with other molecules within the solution. The principle of operation of the DLS technique relies on the analysis of fluctuations intensity of scattered light, during sample laser illumination. The determination of particle size using this technique is based on the Stokes-Einstein equation, which correlates the size of

particles with their speed using the translational diffusion coefficient. The speed of particle diffusion is measured, by determining the rate at which the intensity of the scattered light fluctuates. The fluctuation of the light intensity will be more rapid in case of small particles, as compared to larger ones. A component of the DLS instrument called the digital correlator is used during the measurement for ascertaining the degree of correlation of the measured signals, allowing for the determination of size, as well as size distribution of particles in the measured sample. In other words, the correlator measures the degree of similarity of signals at different time intervals. This correlation of two signals reduces in time. A point in the correlation graph (the function of the correlation value versus time), at which a significant decay of correlation is observed indicates the mean size of the samples' particles, as well as its polydispersion.

2.1.5. Transmission Electron Microscopy

Transmission electron microscope (TEM) analysis is possible due to the wave nature of electrons. Electrons being an ionizing radiation are capable of ionizing atoms within the examined sample. Transmission electron microscopy comprises several different instruments, that utilize the characteristic features of electrons. The electrons are focused into a thin beam using electromagnetic lenses, after being emitted from the source. The resolution of an TEM microscope exceeds by many times the resolution of a light microscope. This is caused by the small value of the electrons' de Broglie wavelength, which is inversely proportional to its energy. Electrons forming the electron beam are scattered due to electrostatic interaction with the samples' electrons. In the TEM technique forward scattering is usually utilized for signal gathering. Most important factors influencing scattering are the electron energy, sample density, thickness and crystallinity, as well as the atomic number of the scattered atom. The probability of an electron interacting with an atom via scattering is determined by the interaction *cross-section*. This factor depends on the electron beam energy. It is noteworthy that in this method the whole sample remains in focus provided it is electron transparent. This feature is independent of the sample's topography.[259]

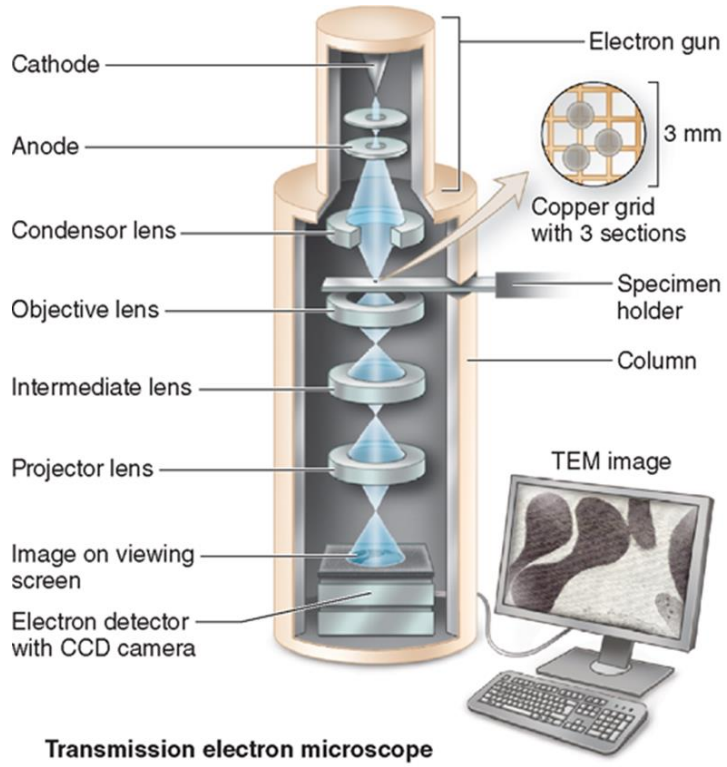

Fig. 30. Diagram of TEM microscope.[260]

Another closely related technique is Scanning Transmission Electron Microscopy (STEM). In this method a finely focused beam of electrons is scanned across the specimen. Transmission modes of imaging are usually utilized since detecting transmitted electrons affords higher signal levels and better special resolution.[261] Increasing the accelerating voltages results in increased specimen penetration. Moreover, due to a decreased electron wavelength higher spatial resolution is then available.

2.1.6. Scanning Electron Microscopy

Scanning electron microscopy (SEM) is a technique widely utilized for the examination and analysis of microstructural characteristics of solid objects.[262] The examined specimen is irradiated with a focused electron beam, producing signals derived from secondary electrons, backscattered electrons, Auger electrons, characteristic X-rays, and photons of different energies[262] (Fig. 31. – [263]). The specimen sample is scanned by the finely focused electron beam, where electrons are accelerated in the direction of the specimen by a voltage in the range of 200 V – 30 kV.[263] A characteristic feature of SEM is the large depth of field,

being a measure of the sample scope remaining simultaneously in focus. This enables acquisition of good quality, in-focus micrographs of rough surfaces at high magnifications.[263] This feature is used to obtain 3D-like images of the specimens' surface. The primary electron beam enters into the sample, where interaction between the beam and sample occurs. For high-resolution imaging secondary electrons originated at the primary beam's point of impact are most desirable. Secondary electrons occurring at other sites as a result of electron scattering within the sample are less significant.

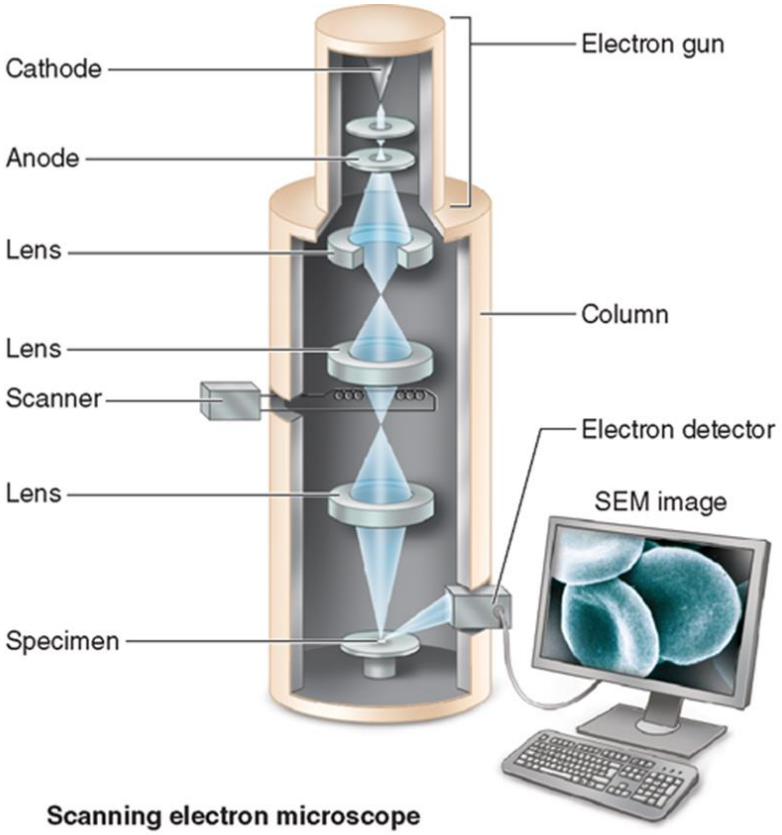

Fig. 31. Diagram of SEM microscope.[260]

Secondary electrons carry surface-specific information about the area interacting with the electron beam. Typically, a depth of roughly 2 – 10 nm for metals, and 5 – 50 nm for insulators beneath the surface is analyzed via this method, since the secondary electrons possess a relatively low energy, hindering their escape from deeper regions of the sample.[263] This escape depth varies with the primary beam accelerating voltage and the atomic number of the specimen.

An important advantage of the SEM method is the attainable high resolution during examination of bulk objects. Resolution values are of the order of 1 – 5 nm. The best obtainable image resolution is limited by the final electron beam diameter. At the same time the intensity of the emitted signals is determined by the current of the electron beam, which is inversely proportional to the beam diameter size.[264] Therefore, a balance between these two parameters must be found.

2.2. Instrumentation and sample preparation

2.2.1. SEM

SEM micrographs of 2D and 3D nanocomposites were recorded on a scanning electron microscope Nova NanoSEM 450 after being deposited onto a silicon substrate. To record images of the 2D nanocomposite film's cross-section the AuNP monolayer was first deposited on the silicon substrate. Next, the sample was immersed in liquid nitrogen for 30 s and then broken in half. The sample was analyzed using SEM microscopy at approximately a 90° angle. STEM images were recorded using Nova NanoSEM 450 after being deposited on a TEM grid (Quantifoil R2/2, 300 Cu mesh).

2.2.2. FTIR

Fourier Transform Infrared Spectroscopy (FTIR) spectra were recorded with a FTIR Jasco 6200 spectrometer. All nanocomposites were dried after synthesis, under vacuum conditions at room temperature, before the registration of the FTIR spectra. Some of the nanocomposites were additionally heated at 80 °C in an oven (as indicated in the name of the composite, by the addition of the word 'sintered'), and kept in that temperature for 12 h.

2.2.3. NMR

^{1}H and ^{13}C NMR spectra were recorded on a Varian Gemini spectrometer (200 MHz) and Varian Mercury 400 MHz. The samples were prepared by drying of the product precipitates at room temperature and their subsequent dissolving in an appropriate deuterated solvent.

2.2.4. DLS

The DLS measurements were done using the Zetasizer Nano ZS instrument. The samples were placed in plastic disposable cuvettes with 1 cm optical path.

2.2.4. UV-vis

UV-vis absorption spectra were recorded on an Evolution 220 by Thermo Scientific company. The samples were placed in plastic disposable cuvettes with 1 cm optical path.

2.3. Gold nanoparticle synthesis

The gold nanoparticles were synthesized in the water phase according to the protocol of Martin method.[62] In the first step a basic solution of sodium borohydride and an acidic aqueous solution of chloroauric acid in water, were prepared. For the preparation of sodium borohydride solution 9.5 mL of distilled water and 1.58 mL of aqueous solution of NaOH (0.4 mmol/mL) were added into a flask containing $NaBH_4$ (0.0248 g; 0.653 mmol). The chloroauric acid solution was prepared by mixing the chloroauric acid precipitate (0.2033 g; 0,516 mmol) with distilled water (10.2 mL) and hydrochloric acid (0.598 mL; 0.8 mmol/mL). To obtain AuNPs, 200 mL of distilled water and 2 mL of auric acid solution (48 mmol/L) were added into an Erlenmeyer flask. The solution was stirred for 5 min, and subsequently 6 mL of the $NaBH_4$(aq) solution (59 mmol/L) was injected into the reaction mixture. A change of color from yellow to dark red was observed, indicating the formation of AuNPs. The obtained solution was allowed to stir for 15 min at room temperature (r.t.). It was then heated to 100 °C in an oil bath for 3 min. Next the solution was stirred at r.t. for 1.5 h.

3. Results

The presentation of my results starts with the description of the developed synthetic procedures of novel organic compounds (surface ligands for the functionalization of NPs, cross-linking agent), as well as spectral analysis of their structure, including ^{1}H and ^{13}C NMR experiments. These synthetic protocols are included into the Results section due to their novel character – they were developed specifically with the synthesis of 2D- and 3D-nanocomposites in mind. Next, the synthesis protocol of metallic NPs (Ag and Pt), as well as their structural analysis is reported. In the next section (3.7), I focus on the description of 2D nanocomposite materials. I describe the conditions of monolayer NP film fabrication, which occurs at the liquid-liquid interface, being a synthetic platform for this fabrication process. The synthesis of a stable monolayer nanofilm requires construction of a customized vessel guaranteeing a controlled change of interfacial area and isolation from the external environment. The Results section of this dissertation includes the details of construction of such a compression-reaction device used during the fabrication process along with the monolayer cross-linking procedure. Later, in section 3.7.2, the mechanism of NP migration to the liquid-liquid interface is explained, including the dependence of NPs' susceptibility towards migration on the pH level (section 3.7.3). The importance of emulsion microdroplets, acting as NP carriers is elucidated. Finally, structural and mechanical properties of the obtained 2D film are analyzed (sections 3.7.5 – 3.7.7). The subsequent section 3.8 describes synthesis and characterization of 3D nanocomposite materials. The synthetic details of 3D nanocomposite production processes are given for nanocomposites having structures based on natural (cellulose, starch) and synthetic polymers. SEM microscopy experiments are described, during which NP distribution within the nanomaterial matrix is analyzed. In this section, the nature of the NP–polymer matrix bonding is investigated, providing evidence of the formation of durable chemical bonds. The analysis includes FTIR and NMR experimental evidence. Finally, I propose a plausible explanation of the role of nanoparticles in the process of covalent bond formation between nanoadditives and nanocomposite matrices.

3.1. Synthesis of aminothioalkyl ligands

Three different aminothiolate ligands were synthesized, with four, eight, and twelve carbon atoms in the alkyl chain referred to as C4, C8, and C12, respectively. These ligands possess a thiol group at one terminal end and an amino group in the opposite terminal position. The synthesis of these ligand consisted of only three steps. In the first step, one of the bromine atoms of dibromoalkane (e.g. 1,8-dibromooctane) was substituted by the phthalimide group. Then, the second bromine atom was replaced by the thioacetate group. Finally, the terminal protective phthalimide and acetate groups were removed in a deprotection reaction (hydrazinolysis and hydrolysis with hydrazine and hydrochloric acid, respectively).

Ligand synthetic procedure

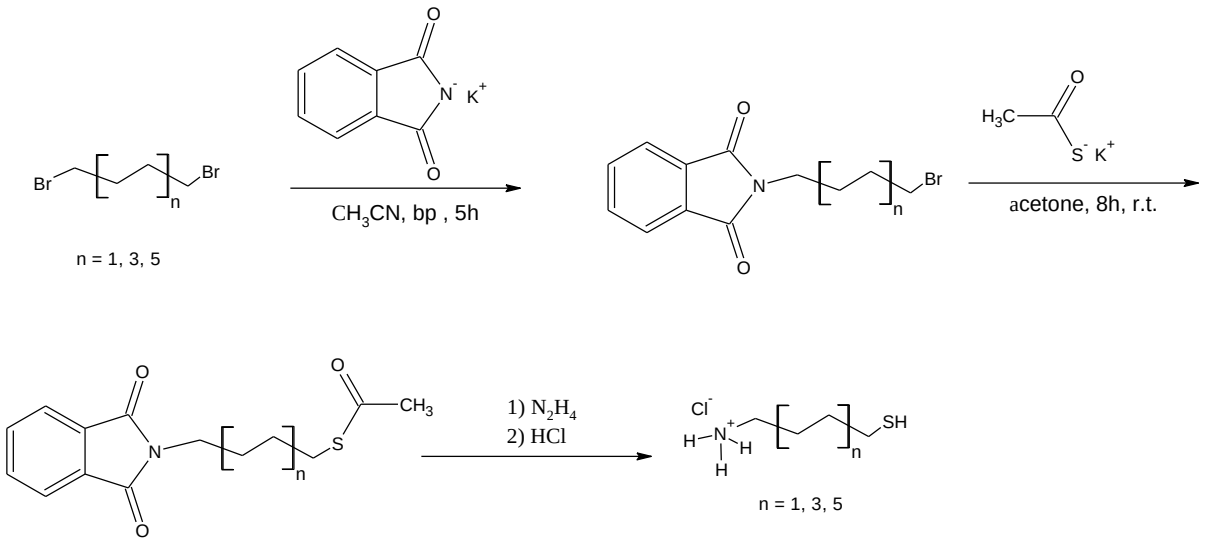

Scheme 1. Synthetic routes for the aminothioalkyl ligands. Structures of the ligands used for functionalization of the NPs: n=1: H_3^+N-CH_2-$(CH_2)_2$-CH_2-SH (C4), n=3: H_3^+N-CH_2-$(CH_2)_6$-CH_2-SH (C8), and n=5: H_3^+N-CH_2-$(CH_2)_{10}$-CH_2-SH (C12).

3.1.1. Synthesis of 8-mercaptooctan-1-aminium chloride

The following procedure is given for an exemplary ligand – 8-aminooctane-1-thiol.

Stage 1 – Synthesis of Synthesis of (8-bromooctyl)phthalimide

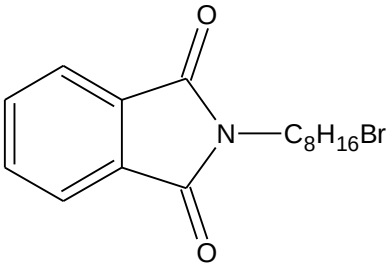

Acetonitrile (80 mL) and 1,8-dibromooctane (1.00 g, 2.688 mmol) were added into a 100-mL flask equipped with a stirring bar, under a reflux condenser. The reaction mixture was heated to boiling point and potassium phthalimide (0.550 g, 2.969 mmol) was added. The mixture was kept at the boiling temperature for 6 hours. Next the solvent was distillated from the reaction mixture. Chloroform (70 mL) was added to the residue and the crystalized potassium bromide was filtered off. The transparent solution was condensed under reduced pressure and the product was isolated by silica-gel flash column chromatography (n-hexane : chloroform = 1:1).

Stage 2 – Synthesis of (8-phthalimideoctyl)thioacetate

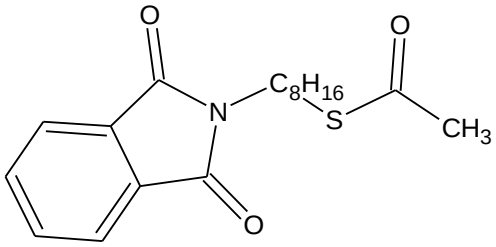

Acetone (150 mL) and 8-bromooctylphthalimide (0.660 g, 1.950 mmol) were added into a 250-mL flask equipped with a stirring bar. Next potassium thioacetate (0.223 g, 1.953 mmol) was added, and the reaction mixture was mixed at room temperature for 12 h. Afterwards the mixture was condensed under reduced pressure. Chloroform (70 mL) was added and the crystallized potassium bromide was filtered off and the transparent liquid was condensed.

Stage 3 – Removal of the terminal protecting groups – synthesis of 8-merkaptooctan-1-aminium chloride

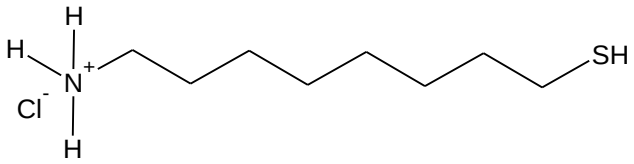

Ethanol (60 mL) and thioacetate ester of octane phthalimide (0.864 g; 2.591 mmol) were added into a 250-mL flask equipped with a stirring bar under a reflux condenser. The reaction mixture was heated to 75 °C and a 40% aqueous solution of hydrazine (0.84 mL) was added. The mixture was kept at this temperature for 5 hours. In the next step the mixture was condensed under reduced pressure, until dry. To the remaining residue methanol (60 mL) was added, the solution was heated to 75 °C and 1 M hydrochloric acid solution in methanol (10 mL) was added. The reaction was kept at the elevated temperature for another 7 hours. After this time the mixture was cooled to room temperature upon which a white precipitate formed. The precipitate was filtered off and washed with methanol three times. The filtrate was condensed to approximately 10 mL volume. Methanol (40 mL) was added to the remaining solution. The product was isolated by precipitation from acetone (MeOH : Acetone 1:18).

3.1.2. Synthesis of 4-aminobutan-1-aminum chloride and 12-aminododecan-1-aminium chloride

Analogous synthesis protocol to the one described for 8-aminooctan-1aminium chloride applies to:

- 4-aminobutan-1-aminium chloride, wherein the following amounts of reagents were used:

In the first stage, 14.5 g (67.25 mmol) of 1,4-dibromobutane, 50 mL of acetonitrile, and 6.28 g (33.90 mmol) of potassium phthalimide. To isolate the main product the acetonitrile was distilled off, and a mixture of chloroform and distilled water was added in order to extract the product into the organic phase. The organic phase was then dried over anhydrous $MgSO_4$. Next 50 mL of ethanol was added and the mixture was heated below the boiling point. After the crystallization of the main product, it was filtered on a paper filter.

In the second stage 2.49 g (8.836 mmol) of 4-bromobutylphthalimide, 150 mL of acetone, and 1.01 g (8.807 mmol) of potassium thioacetate were used. To isolate the main product the solvent was distilled off, and subsequently 30 mL of distilled water were added. The precipitate was then filtered and recrystallization in ethanol was done. The obtained product was washed several times with ethanol.

In the third stage 1.94 g (6.700 mmol) of thioacetate ester of butane phthalimide, 100 mL of ethanol, 0.78 mL of 40% aqueous solution of hydrazine and 10 mL of 0.8M HCl aqueous solution were used. To isolate the main product the solvent and acid were distilled off and subsequently 150 mL of distilled water was added. The solution was heated below the boiling point, and crystallization occurred once the solution was cooled. The precipitate was filtered and the remaining solution was condensed. The main product was isolated by precipitation from acetone.

- 12-aminododecan-1-aminium chloride, wherein the following amounts of reagents were used:

In the first stage 2.00 g (6.095 mmol) of 1,12-dibromododecane, 100 mL acetonitryl and 1.00 g (5.399 mmol) of potassium phthalimide. The main product of the reaction was isolated using column chromatography, with a chloroform: n-hexane (1:1) mixture as the eluent.

In the second stage 1.02 g (2.597 mmol) 12-bromododecylphtalimide, 100 mL of acetone and 0.312 g (2.679 mmol) of potassium thioacetate were used.

In the third stage 0.550 g (1.412 mmol) of thioacetate ester of dodecane phthalimide, 60mL of ethanol, 0.37 mL of 40% aqueous solution of hydrazine and 10 mL of 0.8 M aqueous solution of HCl dissolved in 60mL of methanol were utilized.

A collective presentation of the reagent and product quantities along with the reaction yields of each synthetic stage is shown in Table 1.

Stage No.	Ligand	Substrate				Yield		
1		**Dibromoalkane [g]**	**Dibromoalkane [mmol]**	**Potassium phthalimide [g]**	**Potassium phthalimide [mmol]**	**[g]**	**[mmol]**	**[%]**
	C4	14.5	67.25	6.28	33.90	6.81	24.13	71.18
	C8	1.00	2.688	0.55	2.969	0,660	1,950	72,54
	C12	2.00	6.095	1.0	5.399	1.024	2.597	48.10
2		**Bromoalkyl phthalimide [g]**	**Bromoalkyl phthalimide [mmol]**	**Thioacetate [g]**	**Thioacetate [mmol]**	**[g]**	**[mmol]**	**[%]**
	C4	2.49	8.836	1.01	8.807	1.584	5.713	64,85
	C8	0.660	1.950	0.223	1.953	0.63	1.890	96,92
	C12	1.02	2.597	0.312	2.679	1.10	2.498	96,19
3		**Thioacetate ester [g]**	**Thioacetate ester [mmol]**	**Hydrazine [mL]**	**HCl [mL]**	**[g]**	**[mmol]**	**[%]**
	C4	1.94	6.700	0.776	11.64 (aquesous condensed)	0.650	4.588	65.76
	C8	0.864	2.591	0.84	10 (1M in methanol)	0.300	1.517	58.55
	C12	0.559	1.412	0.37	10 (0.8M aqueous)	0,245	0,965	68,34

Table. 1. Presentation of the reagent and product representative quantities, as well as reaction yields of each synthetic stage performed during the conducted syntheses.

3.2. Structural analysis of the ligands

^{1}H and ^{13}C Nuclear Magnetic Resonance (NMR) spectra

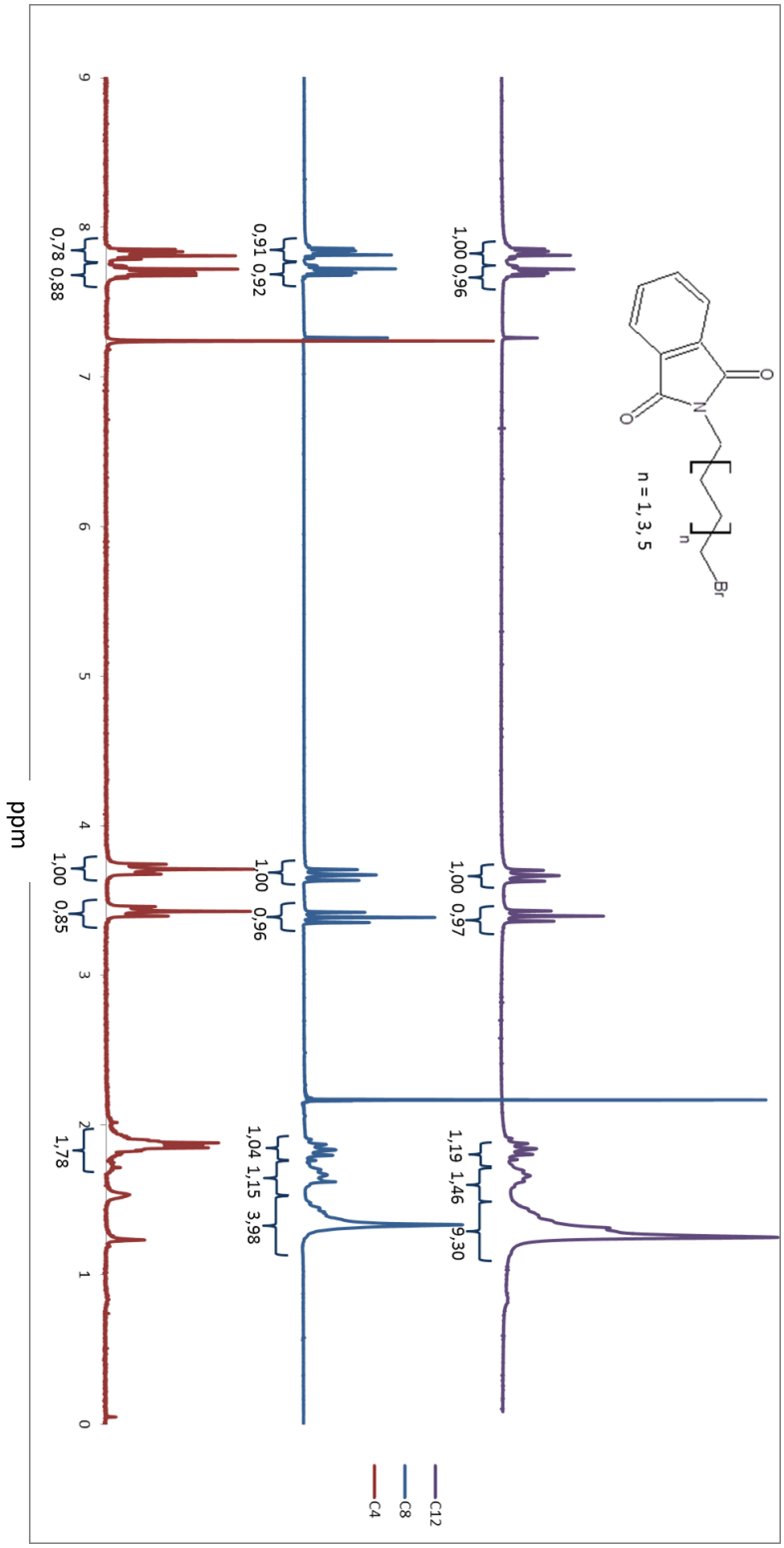

Fig. 32. ^{1}H NMR spectrum of (4-bromobutyl)phthalimide, (8-bromooctyl)phthalimide and (12-bromododecyl)phtalimide in chloroform $CDCl_3$.

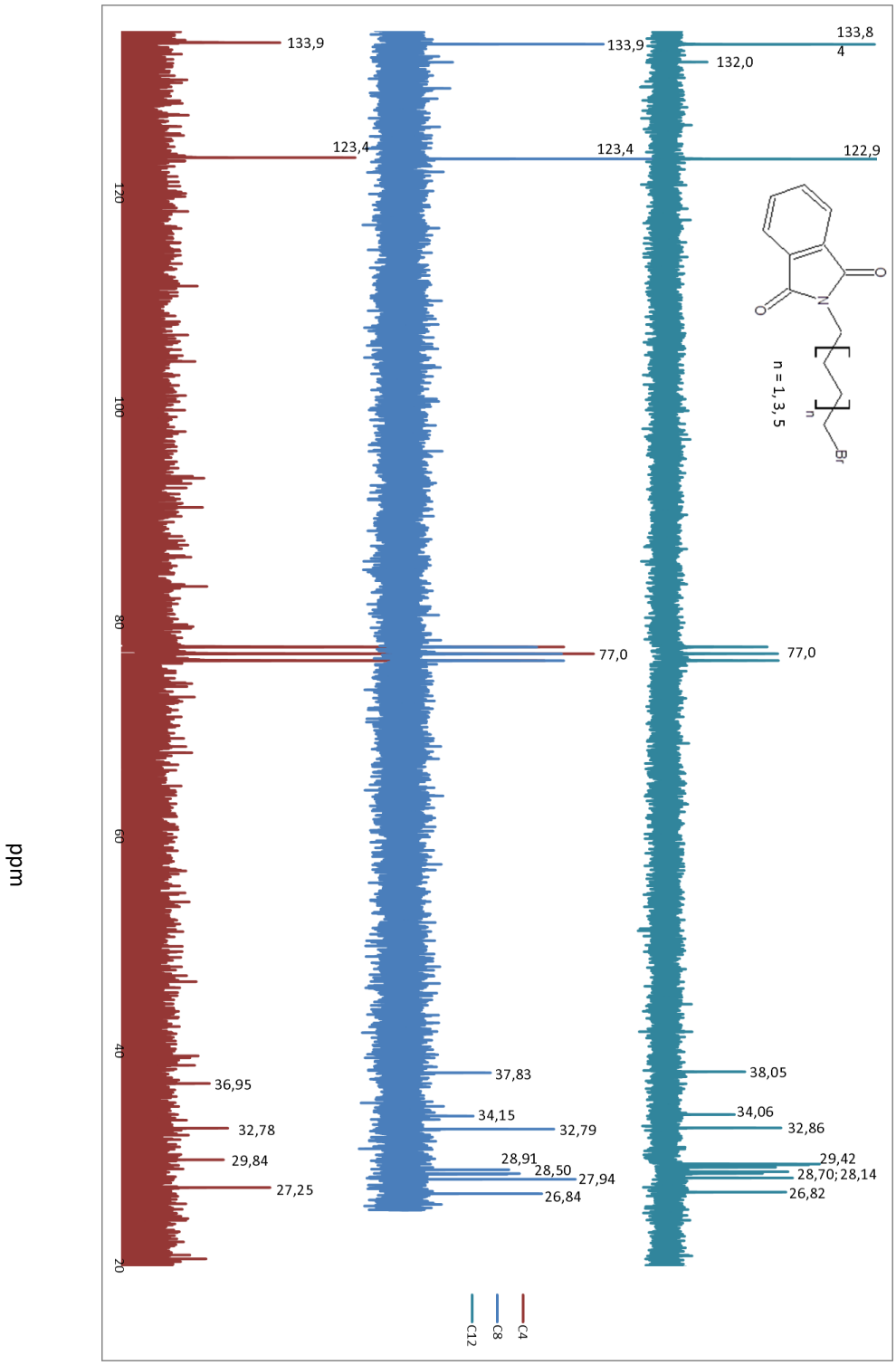

Fig. 33. ^{13}C NMR spectrum of (4-bromobutyl)phthalimide, (8-bromooctyl)phthalimide and (12-bromododecyl)phtalimide in chloroform $CDCl_3$.

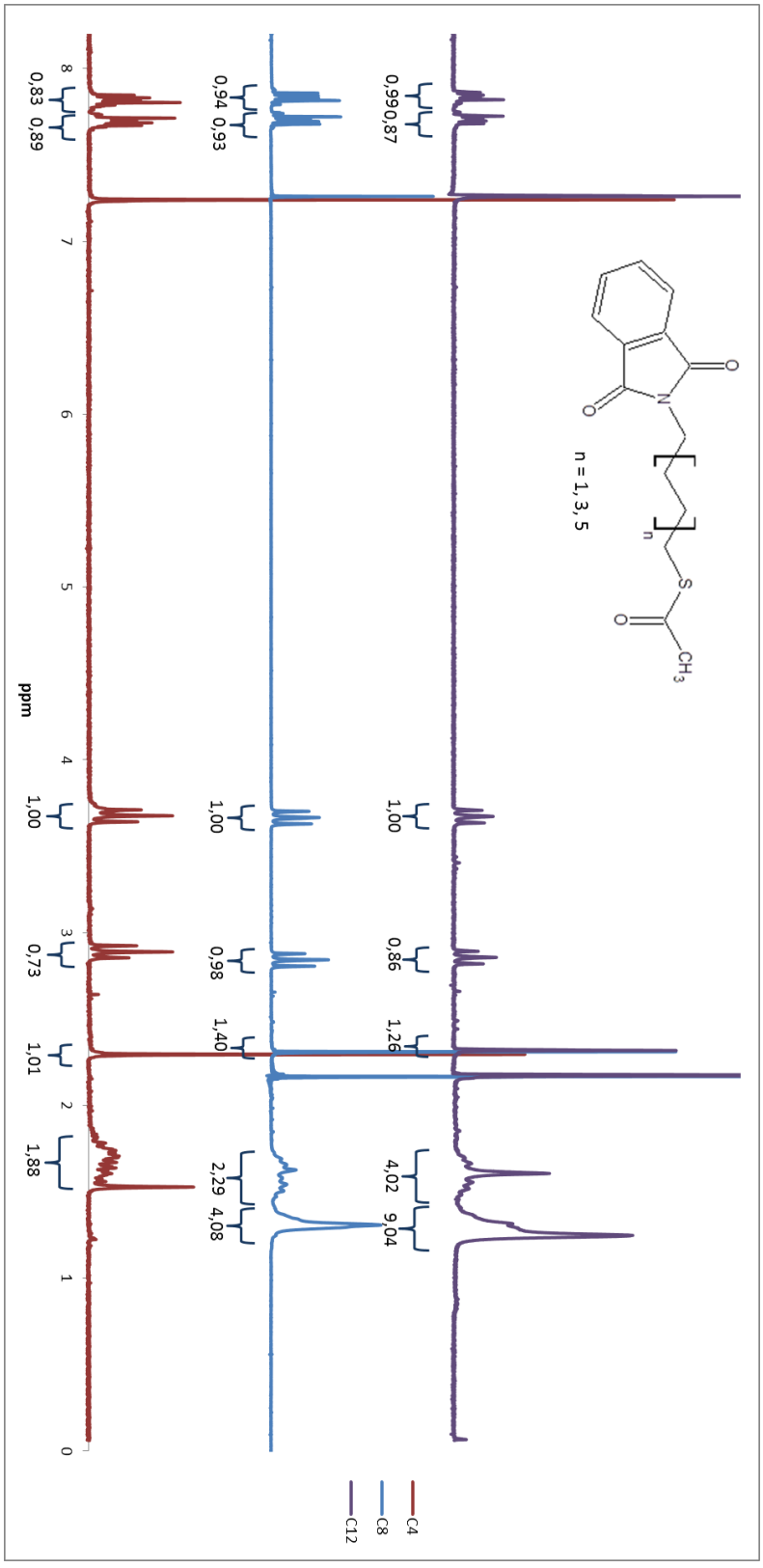

Fig. 34. ^{1}H NMR spectrum of (4-phthalimidebutyl)thioacetate, (8-phthalimideoctyl)thioacetate and (12-phthalimidedodecyl)thioacetate in chloroform $CDCl_3$.

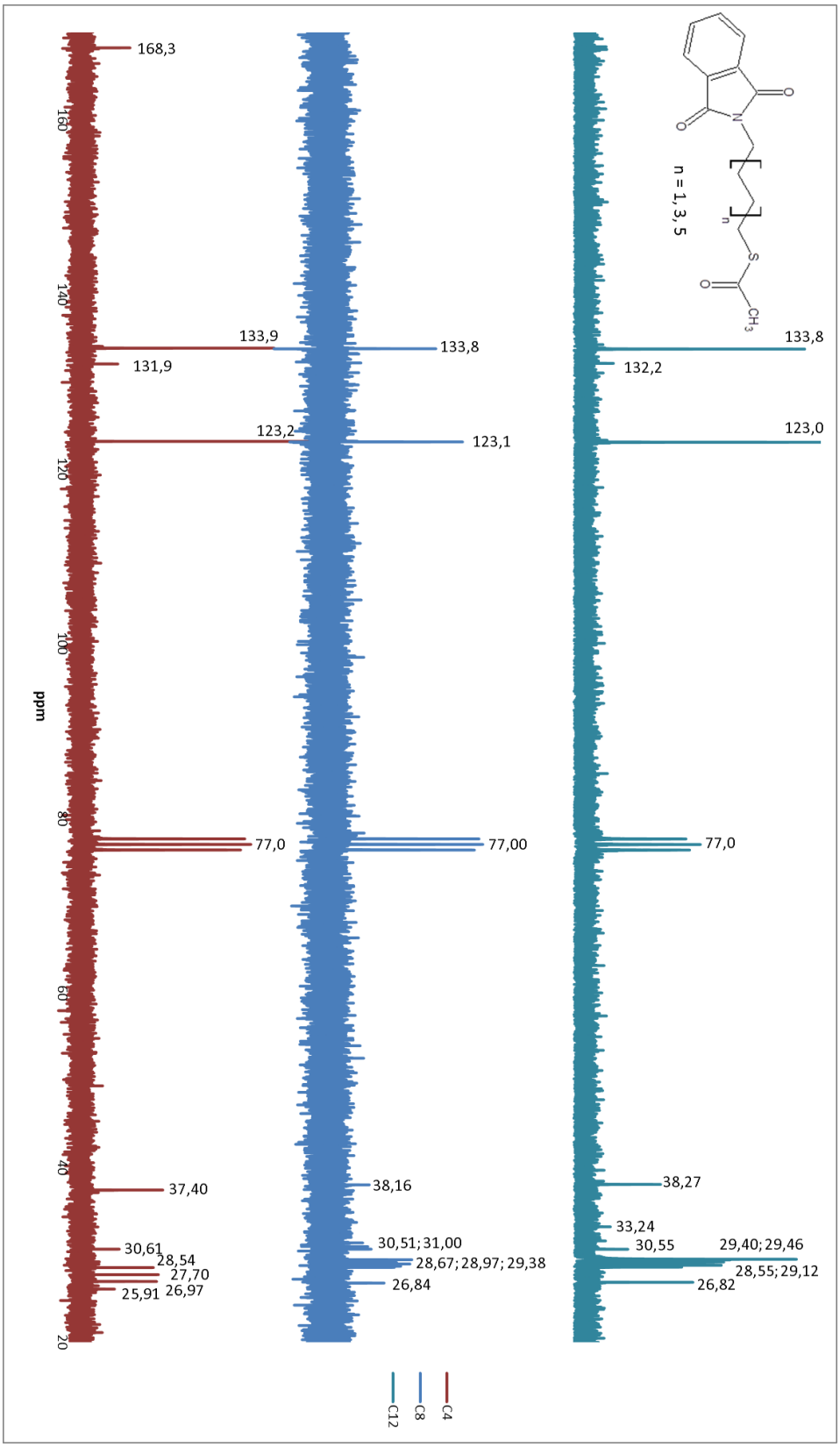

Fig. 35. ^{13}C NMR spectrum of (4-phthalimidebutyl)thioacetate, (8-phthalimideoctyl)thioacetate and (12-phthalimidedodecyl)thioacetate in chloroform $CDCl_3$.

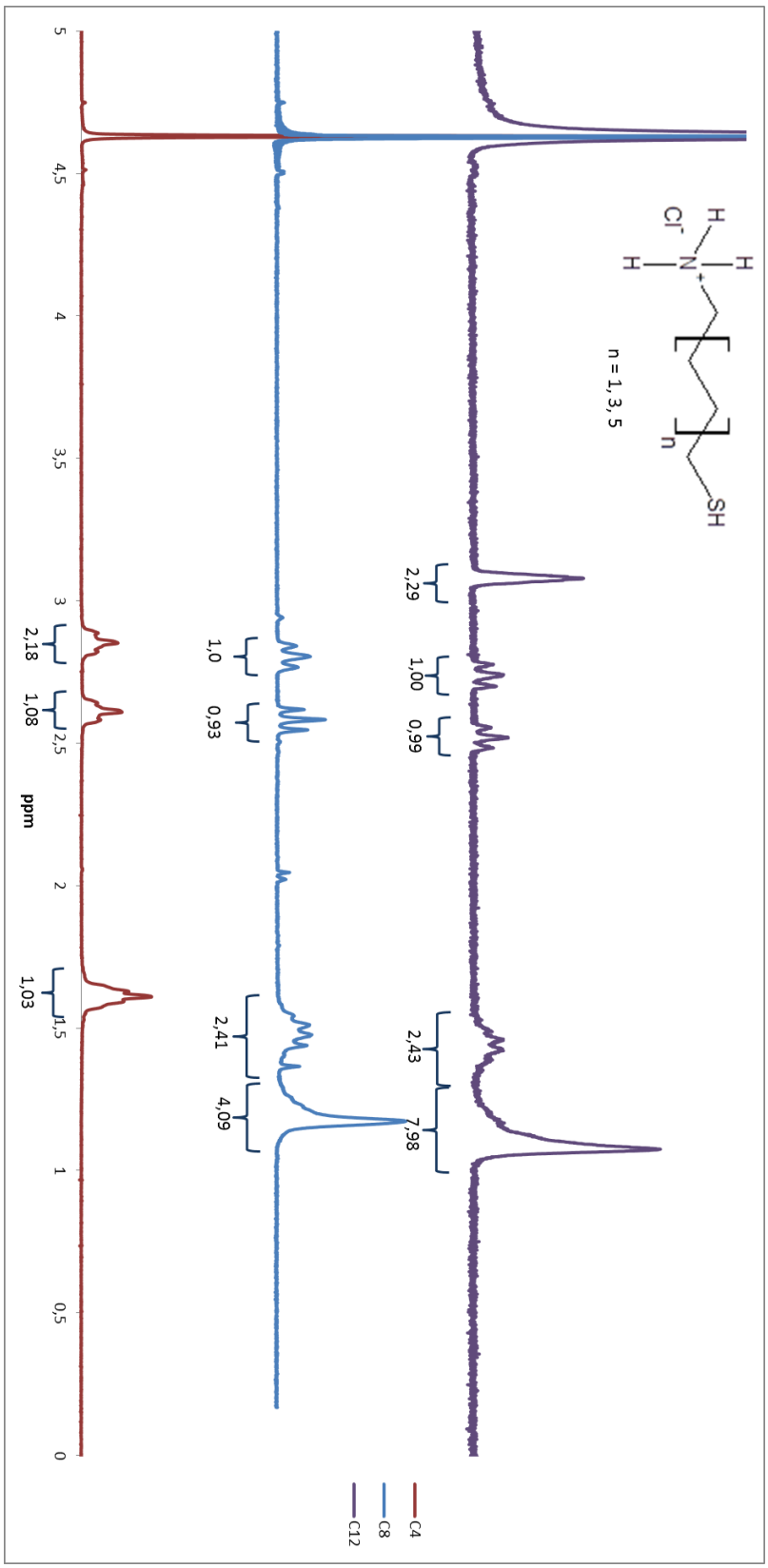

Fig. 36. ^{1}H NMR spectrum of 4-merkaptobutyl-1-aminium chloride, 8-merkaptooctan-1-aminium chloride and 12-merkaptododecan-1-aminium chloride in D_2O.

3.2.1. Spectral analysis of the intermediate and final products of the ligands' synthesis

^{1}H NMR Spectra

On the ^{1}H NMR spectra of compounds having a phthalimide substituent in one terminal position and a bromide atom in the other terminal position of the alkyl chain (Fig. 32) signals characteristic for the aromatic phthalimide group are visible in the section 7.71 – 7.81 ppm. The signals characteristic for the methylene group connected directly, through a single covalent bond, to the nitrogen atom of the phthalimide group are visible at around 3.65 – 3.71 ppm, whereas signals at around 3.37 – 3.42 ppm correspond to the methylene groups adjacent to the bromide atom. The signals in the section between 1.2 – 1.9 ppm correspond to hydrogen atoms of the alkyl chain, where each of the methylene groups neighbors only with other methyl groups within the chain.

In the ^{1}H NMR spectra of compounds obtained in the second substitution reaction, where the bromide atom is replaced by the thioacetate group (Fig. 34), the signals discernable at 2.3 ppm corresponds to the methyl groups being a part of the thioacetate. Additional proof that the reaction proceeded according to the presented Scheme 1 is the disappearance of the signal derived from the methylene group adjacent to the bromide atom, and simultaneous appearance of a signal at 2.9 ppm corresponding to the methylene group next to the thioacetate functional group. The signals in the section between 1.5 – 1.9 ppm correspond to hydrogen atoms of the alkyl chain, where each of the methylene groups neighbors only with other methyl groups within the chain.

After the removal of the phthalimide and thioacetate protective groups the final product is obtained. On the ^{1}H NMR spectra of 8-merkaptooctan-1-aminium chloride, 4-merkaptobutan-1-aminium chloride and 12-merkaptododecan-1-aminium chloride (Fig. 36) the signal at 2.58 ppm correspond to the methylene group bound by a single covalent bond with the thiol group, whereas the signal at 2.80 ppm indicates the presence of an amino group, as this signal is derived from the methylene group adjacent to it. In this spectrum the other methylene groups of the alkyl chain are represented by the signals between 1.0 – 1.5 ppm.

^{13}C NMR spectra

In the ^{13}C NMR spectra of compounds obtained after the first stage of the synthesis (substitution of one bromide atom by the phthalimide protective group) signals characteristic for the aromatic phthalimide group are visible at around 123 and 133 ppm (Fig. 33). These signals correspond to the tertiary carbon atoms of the aromatic ring. In case of all three ligands the signals at around 34 ppm correspond to the methylene group adjacent to the bromide atom, whereas the signals at around 38 ppm correspond to the methylene group adjacent to the phthalimide protective groups. Signals visible between 26 – 33 ppm are due to the remaining carbon atoms, constituting the alkyl chain.

In the ^{13}C NMR spectra of compounds obtained in the second stage (substitution of the second bromide atom by the thioacetate protective group, see Fig. 35), the signals discernable at around 30 ppm are derived from the methyl group of the thioacetate substituent. Moreover, the lack of the signal at 34 ppm provides extra proof of the completion of this substitution reaction. The other signals remain unchanged.

The ^{13}C NMR spectra were not recorded for the final products of the ligand synthesis, due to the limited solubility of these compounds in organic solvents. However, the high quality ^{1}H NMR spectra of these molecules provided sufficient data to confirm their structure.

3.3. Synthesis of the cross-linking agent – tetra-alkylated naphthalene dianhydride derivative

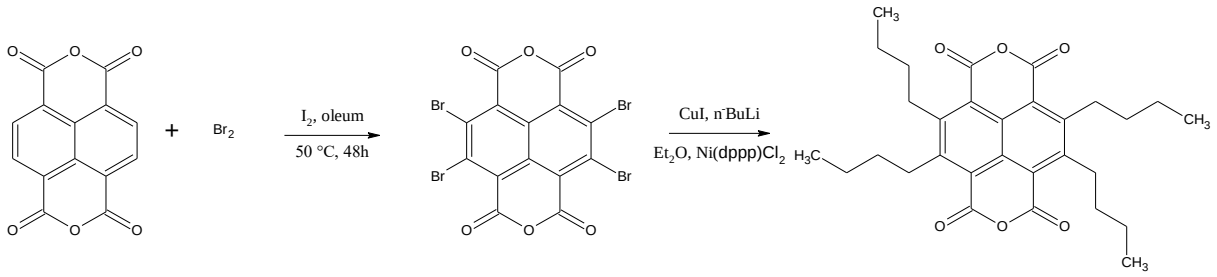

Scheme 2. Synthetic routes for the naphthalene anhydride derivative, having four alkyl substituents.

Stage 1 – Bromination of naphthalene dianhydride

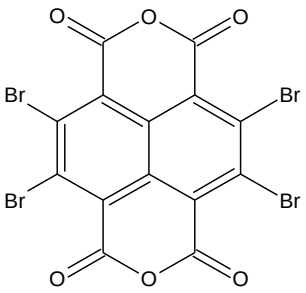

A 6.31 g (23.52 mmol) amount of the naphthalene dianhydride, 0.04 g (0.1575 mmol) of iodine, and 70 mL of 65−70% oleum were mixed in a round-bottom flask, giving a green solution. The mixture was stirred at r.t. for 30 min, before adding 3 mL (10.5 g; 65.7 mmol) of bromine. The reaction mixture was then heated at 50 °C for 48 h. Next, the mixture was poured into a beaker filled with ice and finally filtered on a Buchner funnel. The obtained precipitate was washed with distilled water (until neutral pH of the filtrate was obtained) and methylene chloride, respectively. The obtained yellow product was dried at 50 °C, during 24h.

Stage 2 – Gillman reaction – alkylation of the tetrabrominated naphthalene dianhydride

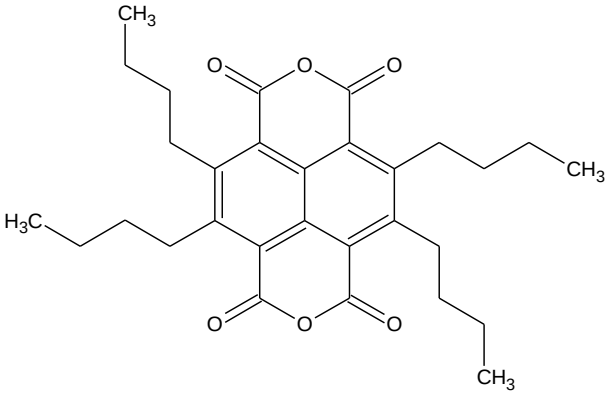

To obtain the Gillman derivative, 1.82 g (9.5 mmol) of anhydrous copper iodine (CuI) and 15 mL of anhydrous diethyl ether were added into a 100 mL round-bottom flask. The reaction was carried out under ambient gas atmosphere (Ar) at reduced temperature, in a isopropanol/dry ice bath (-78 °C). Next 7.6 mL of hexane solution of n-butyllithium (n-BuLi; 2.5 M; 0.019 mmol) was slowly (during 2 h) injected into the reaction mixture. A gradual change of the reaction mixture color into dark purple, and the dissolution of CuI was observed. The reaction mixture was stirred at the reduced temperature for 1 h. Into another

round-bottom flask 1.103 g (1.89 mmol) of the tetrabrominated naphthalene dianhydride (4,5,9,10-tetrabromo- 1,4,5,8-naphthalene tetracarboxylic dianhydride), 75 mg (0.138×10^{-4} mol) of nickel catalyst ([1,3-bis(diphenylphosphino)propane] nickel(II) chloride) and 15 mL of anhydrous diethyl ether were added. The reaction was carried out under ambient gas atmosphere (Ar) at reduced temperature, in a isopropanol/dry ice bath. In the next step the Gilman derivative obtained in the previous step was gradually added into the reaction mixture, during 4 h. A change of the mixture's color to dark green was observed. The reaction mixture was stirred at the reduced temperature for 3 h and then was brought to r.t. and stirred for another 16 h. Next, 100 mL of diethyl ether was added and the reaction mixture was transferred into a separatory funnel. The solution was extracted with aqueous hydrochloric acid (0.4 mol/L). The orange organic phase was separated and extracted twice with distilled water to remove any leftover acid. The obtained organic phase was separated and dried over anhydrous magnesium sulfate ($MgSO_4$), during 20 min. The $MgSO_4$ precipitate was then filtered. The main product was isolated in the next step.

Stage 3 – Isolation of the main product

Chloroform was evaporated under reduced pressure. The remaining residue was dissolved in toluene at an elevated temperature (120 mL). A 20 mL aliquot of the obtained solution was transferred into a separate beaker, and 100 mL of hexane was added, upon which precipitation of a white sediment occurred. This precipitate was filtered on a suction funnel. The filtrate was condensed under reduced pressure to a volume of ~5 mL. Then, 145 mL of hexane was added, and the obtained solution was kept at −10 °C for 12 h. In the next step the precipitated sediment was once again filtered off. Finally the solvent was evaporated at reduced pressure.

3.4. Structural analysis of the cross-linking agent

The ^{1}H and ^{13}C NMR experiments were conducted solely for the final products of the synthesis due to the insufficient solubility of the intermediate products.

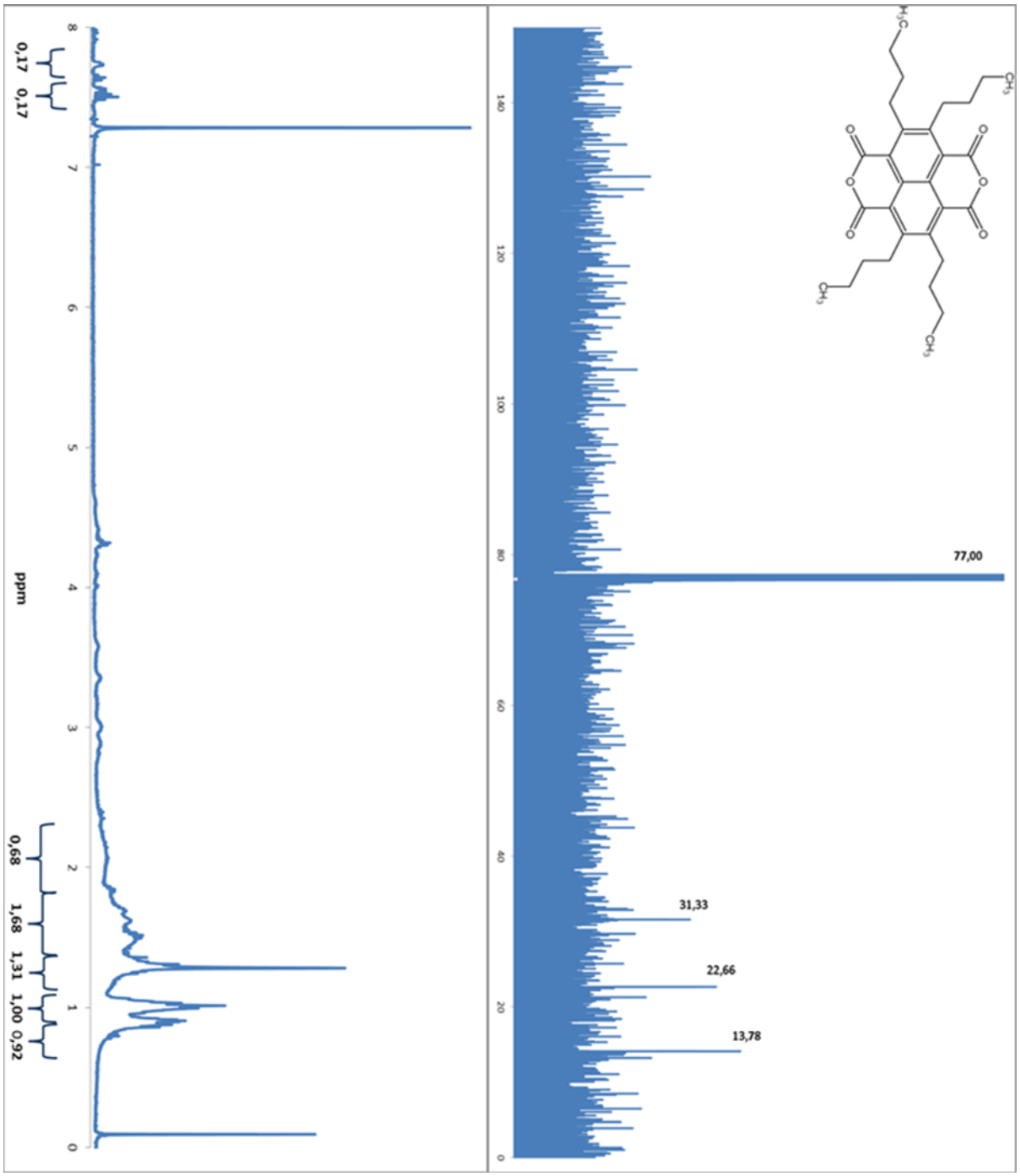

Fig. 37 . ^{1}H and ^{13}C NMR spectra of the tetra-alkylated naphthalene anhydride derivative in CDCl3.\

3.4.1. Spectral analysis of the cross-linking agent molecules

^{1}H NMR Spectra

The ^{1}H NMR spectrum of the cross-linking agent solution indicates that although the studied sample predominantly contains the tetra-substituted anhydride naphthalene derivative, having four alkyl chains attached to the aromatic core, derivatives substituted to a lesser extent (having 1, 2, or 3 alkyl chains) are also present. These minor contaminants also participate in the cross-linking reaction, since they too possess the reactive anhydride functional group within their structure. The deficiency in the number of alkyl substituents influences only their solubility in the organic solution. On the presented spectrum signals visible between 0,84-2,50 ppm correspond to alkyl chains attached directly to the aromatic core of the naphthalene anhydride. The weak signals within the range of 2,85 -3,60 ppm and 7,50 – 8,50 ppm correspond to the hydrogen nuclei of the incompletely substituted naphthalene anhydride molecules.

^{13}C NMR spectra

The signals visible in the ^{13}C NMR spectrum of the tetra-alkylated naphthalene dianhydride derivative correspond to the carbon atoms of the alkyl chains. The signal at 31.33 ppm is derived from the carbon atoms linked directly to the aromatic core of the molecule. The signal at 13.78 ppm corresponds to the terminal carbon atoms in the alkyl substituents, whereas the signal at 22.66 ppm corresponds to the remaining carbon atoms of the alkyl chains. Signals of the quaternary and tertiary aromatic atoms, as well as the atoms constituting the dianhydride functional group were not registered. These signals are often weaker and require higher sample concentration, which was impossible to achieve in this case due to the limited solubility of the molecule. The data obtained in the ^{1}H and ^{13}C NMR experiments is sufficient to confirm the structure of the cross-linking agent.

3.5. Nanoparticle synthesis and functionalization

3.5.1. Gold nanoparticles

3.5.1.1.Gold nanoparticle functionalization in the organic phase

In the first step the AuNPs, synthesized according to the Martin method, were transferred into a separatory funnel. A 40 mL of octadecylamine (0.041 mg; 0.152 mmol) toluene solution was added into the funnel. Extraction of the AuNPs into the organic phase was performed by vigorous shaking of the system. The organic phase was separated and added into 300 mL of MeOH. This solution was left overnight to allow the AuNPs to precipitate to the bottom of the flask. In the next step, the AuNP methanol solution was centrifuged at 7000 rpm for 10 min, washed with 70 mL of MeOH, and centrifuged again at 7000 rpm for 10 min. This washing procedure was repeated 3 times. After each centrifugation the supernatant was decanted from the precipitate and thrown away. Finally, the obtained AuNP black precipitate was dissolved in 20 mL of toluene.

A 10 mL aliquot of the AuNP toluene solution was divided into 2 mL portions in Eppendorf falcon tubes. Next, 300 μL of the C8 aminothiolate ligand methanol solution (6.73×10^{-3} mol/L) was added into each falcon tube, and the resulting solutions were sonicated for 30 min in reduced temperature (obtained by addition of dry ice to the water bath of the sonicator). Then, the solutions were centrifuged at 5000 rpm for 10 min, and the supernatant was decanted. To the obtained precipitates, 9 mL of MeOH was added and the fractions were combined. Next, the methanol solution was divided equally among six 15 mL falcon tubes, and each of the obtained samples was sonicated for 5 min in reduced temperature. Then 12 mL of n-pentane was added into each falcon, and the precipitates were centrifuged at 7000 rpm during 5 min. The supernatants were decanted, and again 1.5 mL of MeOH was added into each of the falcons, the samples were sonicated for 5 min in reduced temperature, 12 mL of n-pentane was added, and the samples were centrifuged at 7000 rpm for 5 min. This washing procedure was repeated two more times. Finally, 2.81 mL of distilled water was added into the AuNP precipitate obtained after centrifugation to obtain an aqueous AuNP solution (4.03×10^{-6} mol of AuNPs/L). Their core diameter was 5.6 nm, as determined with UV−vis measurements.

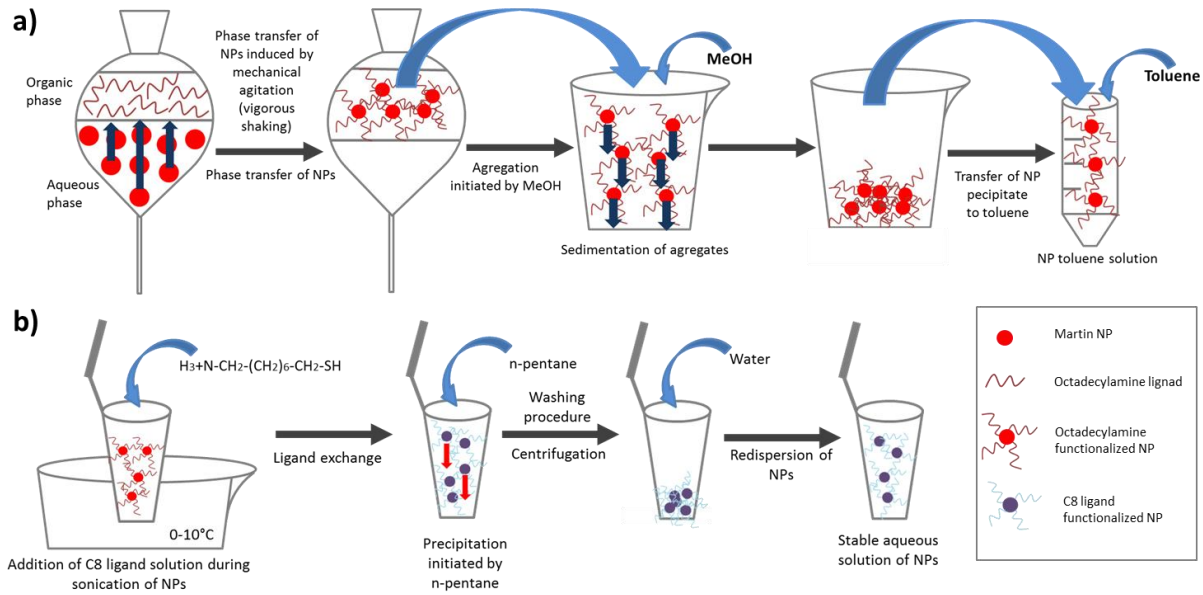

Scheme 3. The procedure of synthesis of octadecylamine functionalized NPs (a), and functionalization of such NPs with the C8 ligand (b).

3.5.1.2. Gold nanoparticle functionalization in the aqueous phase

To functionalize AuNPs, 2 mL of distilled water, aqueous solution of 8-mercaptooctane-1-aminium chloride ligand (171 µL; 10 mM) and hydrochloric acid (96 µL; 0.8 M) were added into a glass vial. The solution was then heated to 70°C, and a solution of AuNPs (20 mL) was added drop-wise into the flask at the rate of 1 drop per second. The mixture was kept at 70 °C for one hour. The obtained NPs were stable for at least 3 months. The NPs were centrifuged at 9000 rpm for 10 min to remove all objects larger than 30 nm. The obtained NPs are denoted Au@C8 in the following text.

3.5.2. Noble metal nanoparticles

Silver nanoparticles synthesis

To obtain AgNPs, tri-sodium citrate solution (1.6 mL; 38.3 mM) was mixed with fresh aqueous sodium borohydride solution (0.4 mL; 112 mM). The obtained solution was cooled to 10 °C and aqueous solution of $AgNO_3$ (20 mL; 1 mM) was added dropwise under continuous stirring, upon which a yellow color appeared.

Silver nanoparticles functionalization

To functionalize the AgNPs, an acidic solution of the ligand was prepared by mixing glacial acetic acid (50 µL), aqueous solution of the ligand C8 (50 µL; 0.001 M) and of distilled water (1 mL). This solution was next cooled to 3–5 °C, and AgNPs solution (5 mL) was added. The color of the solution should not change upon the addition of the AgNPs. The obtained AgNPs were stable for several hours in the solution. The obtained NPs are referred to as Ag@C8 in the following text.

Platinum nanoparticles synthesis

In the case of platinum nanoparticles (PtNPs) aqueous solution of K_2PtCl_4 (7.8 mL; 10 mM) and aqueous solution of trisodium citrate (3.64 mL; 34 mM) were added to distilled water (65 mL). Next fresh aqueous sodium borohydride solution was prepared by dissolving sodium borohydride (4.17 mg) in trisodium citrate solution (5.55 mL; 34 mM) and diluting the obtained mixture with distilled water (25 mL). Finally, the obtained $NaBH_4$ solution was added dropwise under continuous stirring to the solution of K_2PtCl_4 at room temperature. The obtained mixture was kept at room temperature for 5 h and then was centrifuged at 9000 rpm during 10 min. The obtained supernatant was separated giving a clear, greenish solution of PtNPs.

Platinum nanoparticles functionalization

To functionalize PtNPs, distilled water (2.2 mL), aqueous solution of 8-mercaptooctane-1-ammonium chloride ligand (190 µL; 10 mM) and hydrochloric acid (0.6 µL; 0.8 M) were added into a glass vial. The mixture was then heated to 70 °C in a water bath, and 2 mL of the aqueous solution of PtNPs was added drop-wise at 0.5 $mL \cdot min^{-1}$ rate. The mixture was kept at the elevated temperature for another 10 min. The obtained NPs are denoted as Pt@C8 in the following text.

3.6. Characterization of nanoparticles

3.6.1. DLS

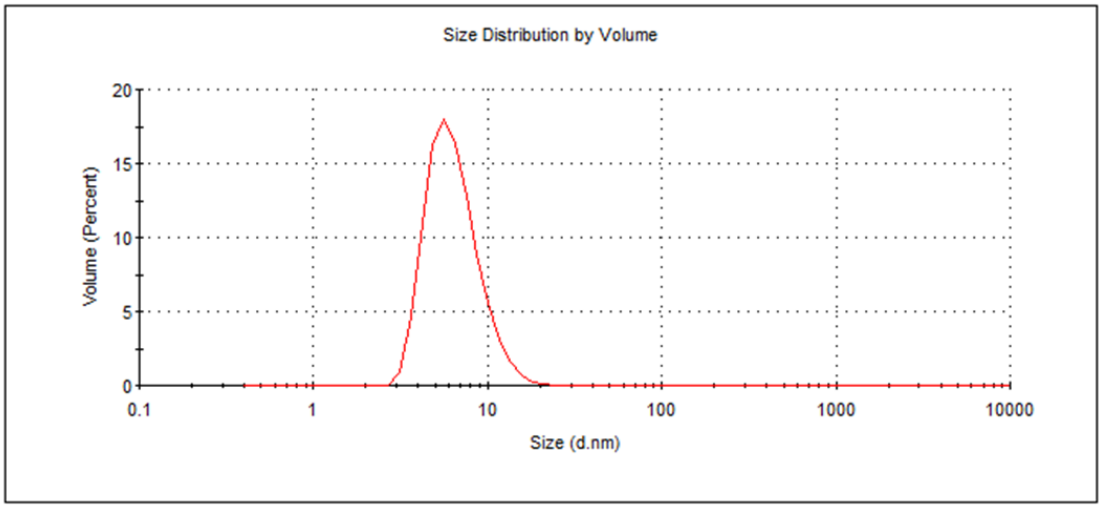

Fig. 38. A graph obtained as a result of the DLS measurement of an aqueous solution of AuNPs synthesized via the Martin method.

The synthesized NPs possessed a diameter of 6.6 nm. As can be seen in Fig. 38, in the obtained graph only one narrow peak was present. Signals originating from larger clusters of the NPs were not detectable. This provides a proof of the measured nanoobjects' low polydispersity and stability against aggregation.

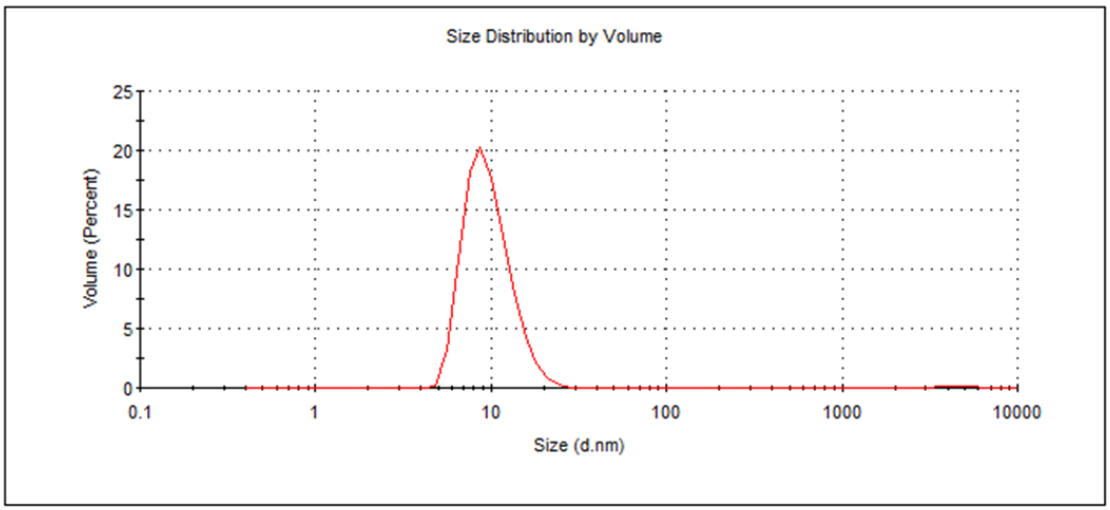

Fig. 39. A graph obtained from the DLS measurement of aqueous solution of AuNPs functionalized in aqueous conditions with the 8-merkaptooctan-1-aminium chloride.

The NPs obtained after functionalization with the 8-merkaptooctan-1-aminium chloride possessed a diameter of 9.8 nm. As expected, the diameter of these NPs is slightly larger than that of the Martin NPs, since the surface ligand possesses a fairly long alkyl chain. A similar trend was observed in case of the NPs functionalized with ligands C4 and C12. The presence of a single narrow peak in the obtained graph provides evidence of the measured nanoobjects' monodispersity.

3.6.2.UV-vis

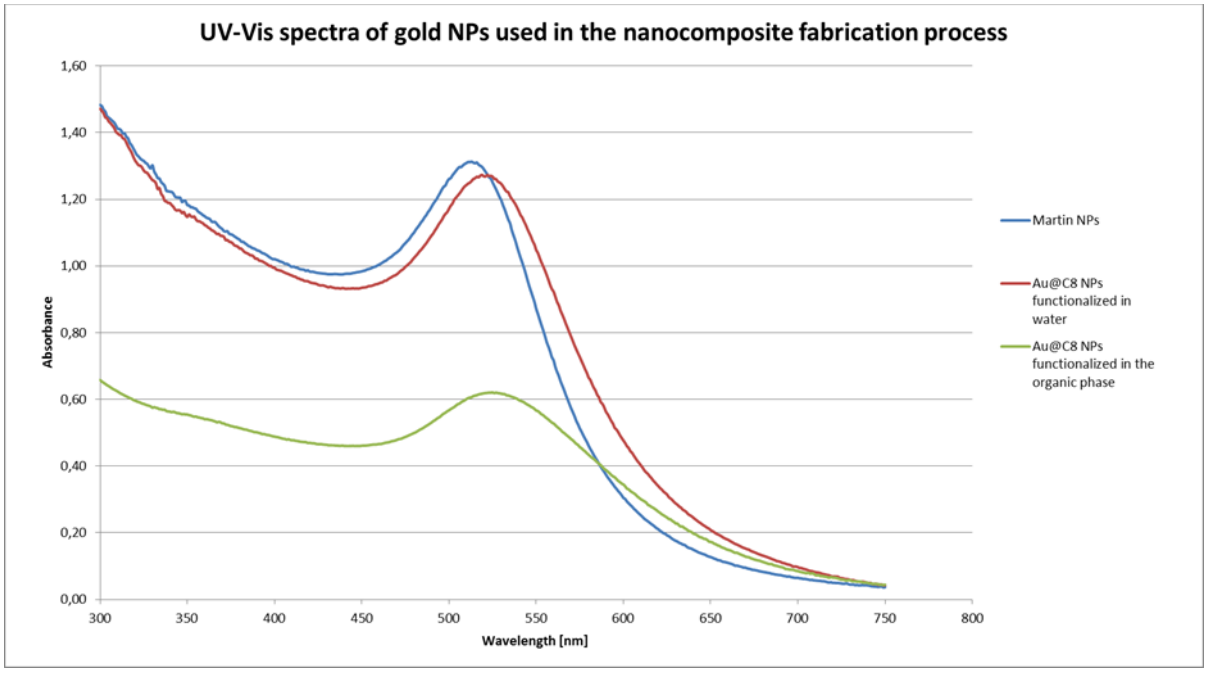

Fig. 40. UV-vis spectra of AuNPs used in the process of 2D and 3D nanocomposite fabrication. Spectra of AuNPs before functionalization with aminothiolalkyl ligand (Martin AuNPs) and after their functionalization in the aqueous and organic phase are shown.

From the UV-vis spectra the size of the gold NPs were calculated, according to the procedure described in Ref. 256. The calculated sizes of the NPs are as following: Martin NPs – 6,06 nm; Au@C8 functionalized in the water phase – 6,23 nm; and Au@C8 functionalized in the organic phase – 6,02 nm. As seen from the obtained spectra the size of the nanoparticles functionalized in the aqueous phase is slightly larger, as compared to the Martin nanoparticles. Since the UV-vis spectrometric method allows for the measurement of the metallic core size, this may indicate that during the functionalization process the nanoparticles

were temporarily less stable. The small width of the peaks corresponding to the Martin NPs and the NPs functionalized with C8 ligand in aqueous conditions indicates the low polydispersity of these solutions. A clear widening of the peak was visible in case of the NPs functionalized with the C8 ligand in the organic phase. This signifies a larger polydispersity of the obtained NP solution.

3.7. 2D nanostructures – self-organization method at liquid-liquid interfaces

3.7.1. Cross-linked NP monolayer fabrication process

Formation of the AuNP monolayer at the oil−water interface by mechanical agitation

A 10 mL glass vial was filled with 2.5 mL of distilled water, 20 μL of AuNPs (4.03×10^{-6} mol AuNPs/L), 2.5 mL of hexane, and 20 μL of 0.04 M aqueous solution of NaOH. As a result, a biphasic system was formed with the AuNPs dispersed in the bottom aqueous phase. Next, the vial was vigorously shaken for 45 s. As a consequence, the system became turbid due to the formation of the oil-in-water emulsion, and the AuNPs were transferred onto the interface, forming a purple layer. Straight away, 55 μL of 0.8 M HCl was injected into the bottom aqueous phase, through the top phase, and immediately the sample vial was once again shaken vigorously for 60 s. This resulted in formation of a red AuNP monolayer at the interface.

In this process NPs functionalized with the C4, C8 or C12 ligand may be used. The chemical properties and reactivity of C4, C8 and C12 ligands are analogous to some extent, however an increase of carbon atoms in the ligands' structure causes gradual alternation of their characteristics. The C8 ligand having an intermediate amount of carbon atoms possesses transitional properties between the properties of the short C4 and the long C12 ligand. For the synthesis of 2D nanofilms the NPs functionalized with C8 ligands were utilized, since they exhibit optimal solubility in both the polar aqueous phase (when in the protonated state) and in the oleic phase (when in the neutral deprotonated state). This ensures better stability of NPs once located at the liquid-liquid interface, where some of the surface ligands are immersed in the water phase, and others in the oil phase. Such increased stability makes the fabrication of

a stable NP monolayer feasible, making the C8 ligand the best choice for the 2D monolayer nanofilm formation process.

Construction of the compression-reaction device

The technical issue that had to be overcome in order to fabricate a cross-linked 2D NP monolayer was the development of a means of controlling the interparticle distance between NPs located at the liquid-liquid interface. This was imperative since initially the distance between neighboring NPs at the interface exceeds greatly the length of the cross-linking agent. Hence effective cross-linking requires reduction of this distance. Moreover, successful preparation of a stable 2D nanofilm required a reaction system isolated from the external environment, to ensure constant composition of the reaction mixture during the fabrication process. These requirements were fulfilled owing to the designed compression-reaction device. The compression-reaction device served as a reaction vessel during 2D monolayer film fabrication that, once securely closed, hindered the evaporation of volatile solvents used during the NP monolayer cross-linking process. The mobile pistons situated on either side of the device enabled area regulation of the liquid-liquid interface, and therefore, provided control of the distance between adjacent NPs within the interfacial monolayer. This function of the device was indispensable, as it allowed for the reduction of the NP-NP distance to an appropriate value that allowed covalent linking of neighboring NPs by the cross-linking agent. Conduction of efficient cross-linking was hence possible. The device was constructed using a 50 mL polyethylene syringe with the tapered end cut off to create a cylinder with two identical openings at both ends. An opening (a window) of the size of about 1 × 1 cm^2 was cut out in the top portion of the cylinder to provide an access to the interior of the device.

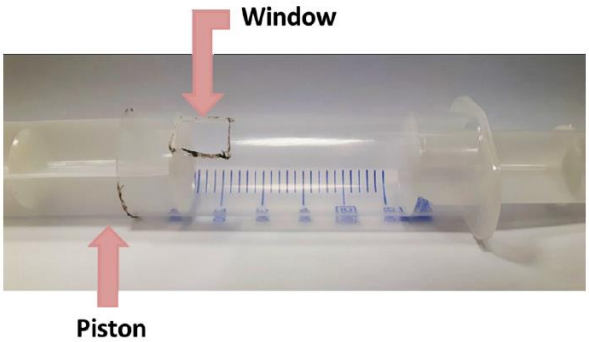

Fig. 41. Image showing the compression – reaction device.

The cylinder was equipped with two polyolefin pistons at both ends. By moving the pistons, the liquid−liquid interfacial area could be easily controlled. The obtained device was equipped with a mixing element, and mounted on a magnetic stirrer. After the addition of the solvents and the AuNPs, one of the pistons was moved past the opening to create a closed (isolated) system to avoid hexane evaporation during the cross-linking process. During the compression of the interfacial area, a needle was inserted into the wall of the cylinder to countervail the inner pressure. The amount of solvents and substrates was easily controlled with a syringe and needle inserted through the wall of the device. After the cross-linking reaction was completed, a second window was cut out in the cylinder, enabling manipulation of the obtained film.

Formation of the AuNP monolayer using the compression-reaction device

The first four vials containing the biphasic hexane/water system with the AuNPs adsorbed at the interface were prepared via the mechanical agitation method described above (point 3.6). Next, 20 mL of 15 mM HCl(aq), 10 mL of hexane, and the four 10 mL vials with the hexane/water/AuNPs system were introduced into the compression-reaction device through the window in the top of the cylinder. A biphasic system was then established. Next, excess solvents (approximately 10 mL of water and 10 mL of hexane), introduced into the system along with the Au@C8 NPs at the interface, were removed from the device. Then, the interfacial area was slowly compressed. The pistons were shifted inward until they were 16 units apart on the cylinder's scale. This distance matched an interfacial area that corresponded well to the area occupied by a monolayer of densely packed AuNPs. The appropriate interfacial area was designated via a trial and error method. An optimum distance between NPs at the interface was selected by comparison of the quality of monolayer films obtained at different degrees of compression. The obtained films were assessed upon their SEM micrographs, registered subsequently to the covalent cross-linking process. The subsequent stages of the process are illustrated in Fig. 42. Upon further compression, migration of the AuNPs into the aqueous phase occurred, due to excessive confinement of the electrostatically repulsing AuNPs. The obtained monolayer was then left for 90 min, while the system was slowly mixed (225 rpm), to allow the AuNPs to spread uniformly at the interface. After this time, 2 mL of a hexane solution of the crosslinking naphthalene dianhydride derivative (4.065×10^{-6} mol) was injected into the upper organic phase, and the system was left under gentle

stirring for 3 days for the reaction to complete. A naphthalene dianhydride derivative, having a semiconducting conjugated aromatic core, was chosen as the cross-linking agent. I decided to employ such molecule because it's properties may be useful in future research, for fabrication of conducting monolayer membranes.

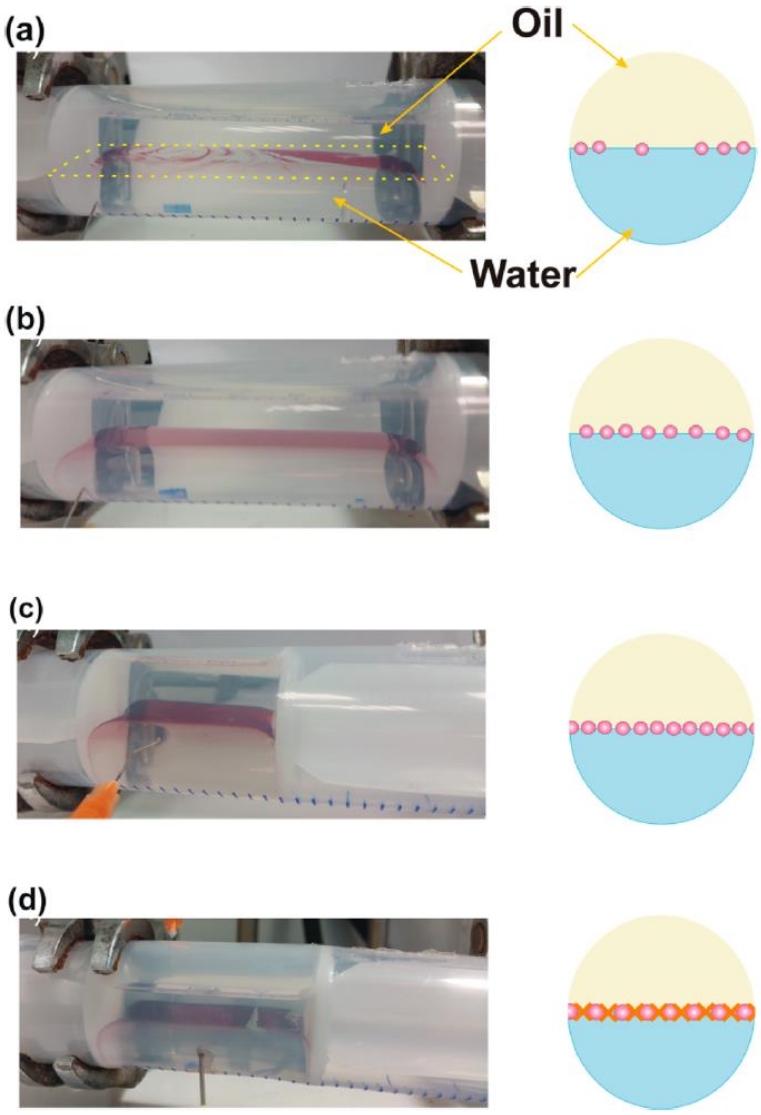

Fig. 42. Subsequent steps of the synthesis of the composite film: (a) AuNPs forming irregular patches at the oil-water interface. (b) Uniform spreading of AuNPs after stirring. (c) AuNPs monolayer after compression. (d) Cross-linked AuNP monolayer. The monolayer cracked in a way characteristic of stiff materials. The schemes illustrate the corresponding arrangement of the AuNPs at the oil-water interface.

Transfer of the cross-linked monolayer onto a TEM grid

To demonstrate the robustness of the obtained cross-linked monolayer and its stability in air conditions, the as-prepared monolayer was transferred onto a TEM grid. Such grids possess circular openings in their structure. The obtained nanofilm was stretched across such openings, and was supported only on the periphery of each aperture, leaving the most part of the film unsupported. This provided a direct evidence of the truly free-standing nature of the film. To transfer the monolayer membrane a Teflon support was placed in the bottom phase of the compressing device before the addition of the AuNPs. On this holder a TEM grid (Quantifoil R2/2, 300 Cu mesh) was then placed.

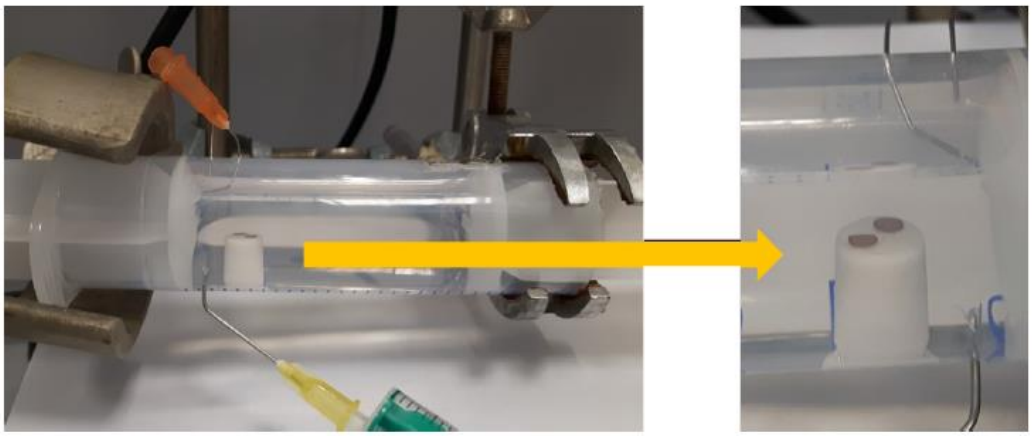

Fig. 43. Photograph showing the Teflon holder and TEM grids immersed in the bottom phase inside the compression-reaction device, before free-standing monolayer fabrication process.

The grid was present in the device during the whole fabrication process. Once the cross-linking reaction was completed, 1.5 mL of the upper hexane phase was removed and, subsequently, 1.5 mL of pure hexane was added. This rinsing procedure was repeated 5 times to remove any unbound cross-linking agent from the system. Finally, two needles (0.5 mm diameter) were inserted into the device through its walls – one above the top phase and one in the bottom of the device, so that the end of the needle was submerged in the aqueous phase – to allow very slow gravitational outflow of the solvents. As the liquid−liquid interface was lowered below the level of the TEM grid, the monolayer was deposited on its top. Finally, an opening (1×1 cm^2) was made in the top wall of the cylinder through which the grid was taken out from the device. Before the analysis the grid was immersed in pure chloroform for 0.5 min to remove any organic contaminations such as unreacted or weakly bound cross-

linking molecules, as well as any polymer residues that may be left on the TEM grid after its fabrication.

3.7.2. Emulsification-induced transfer of the AuNPs onto the interface ("cargo mechanism")

The AuNPs do not adsorb spontaneously at the interface. The key role in the AuNP transfer mechanism is played by hexane microdroplets that act as the carriers of the AuNPs that transport them as a "cargo" from the bottom phase to the interface. Transfer of the AuNPs from the bulk aqueous phase to the oil−water interface is facilitated by the formation of the oil-in-water emulsion. Vigorous shaking is the simplest way for creation of microdroplets in the bottom phase. Such mechanical agitation provides input of energy needed for expending the interface between the two immiscible liquids and the formation of the oil-in-water emulsion. Another way of microdroplet generation is by inducing a rapid quench of temperature of a biphasic system, where both phases are saturated with the minor ingredient (water in the oleic phase, and oil in the aqueous phase) before the quench. In case of the water – hexane pair when considering liquid-liquid equilibria, a general trend of increasing solubility of oil in water with temperature is observed.[265] A rapid decline of temperature leads to a sudden drop of this solubility. The single binary water – oil phase transforms into a biphasic system, whereby the precipitated hexane in the water-rich phase is in the form of microdroplets.

Two phenomena are responsible for the emulsification-induced transport mechanism: (i) the energy barrier due to the partial deprotonation of the aminothiolate ligands occurring during the transition of the AuNPs from aqueous phase on the oil−water interface and (ii) the entrapping of the AuNPs at the oil−water interface. The rough approximation of the deprotonation energy for primary amines is about 20−30 kJ/mol[266] (about 10 k_BT per ligand molecule). The number of ligands on the AuNP of the diameter ~5 nm is estimated as ~400−500.[267] Thus, assuming that from 10 to 100 ligand molecules have to be deprotonated for the AuNP to be adsorbed on the oil−water interface, the energy barrier is as big as 10^2−10^3 k_BT. Creation of the oil-in water emulsion provides an excitation that is needed to overcome such a high energy barrier and bring the system to the stable lowest energy state (Fig. 44). The formation of the oil-in-water emulsion increases the energy of the system in two ways. First, it increases the total oil−water interfacial area and, consequently, the total

interfacial energy. Second, it causes the increase of the chemical potential, μ_{oil}, of the oleic phase. The value of μ_{oil} grows because the formation of the emulsion causes a substantial increase of the pressure of the oil within the droplets. The extra pressure is given by the Laplace formula, $\Delta p = 2\gamma_{ow}/R$, where R is the radius of the droplet. Since chemical potential is an increasing function of the pressure, one has $\mu_{oil}(T, p+\Delta p) > \mu_{oil}(T, p)$. The surface tension between two liquids can be reduced by surfactant or solid particle adsorption.[268] Adsorption of the AuNPs at the interface gives rise to the decrease of the value of the oil−water surface tension, γ_{ow}, by the value $\Delta\gamma_{ow}$, which is approximated [268, 269] as the product $\Delta\gamma_{ow} = E_a N_a$. Here E_a is the AuNP adsorption energy, and N_a denotes the number of the adsorbed AuNPs per unit area of the oil−liquid interface. It is the reduction of the chemical potential μ_{oil} that makes the AuNPs adsorb at the surface of the oil droplets. That is, the lowering of the interfacial energy resulting from the decrease of the interfacial tension is not sufficient to overcome the energy barrier and trigger the adsorption. Otherwise, the AuNPs would spontaneously adsorb also at the planar oil−water interface. The oil-in-water emulsion is unstable and the oil droplets coalesce to reduce the total interfacial area. In the process, the droplets driven by the buoyancy forces carry upward the adsorbed AuNPs as their "cargo". Eventually, the planar oil− water interface is restored (Fig. 44).

The established interface contains all of the AuNPs that adsorbed at the oil droplets. The unusual stability of the AuNP monolayer adsorbed at the oil−water interface is a remarkable feature of the system discussed. Once the AuNPs had adsorbed at the interface it was extremely difficult to transfer them back into the bulk phase. The monolayer withstood even re-emulsification of the system. The only way to make the AuNPs migrate back to the aqueous phase is reduction of the interface area. The strength of the adsorption force can be explained in terms of the entrapping effect that is shown in the inset in Fig. 44.

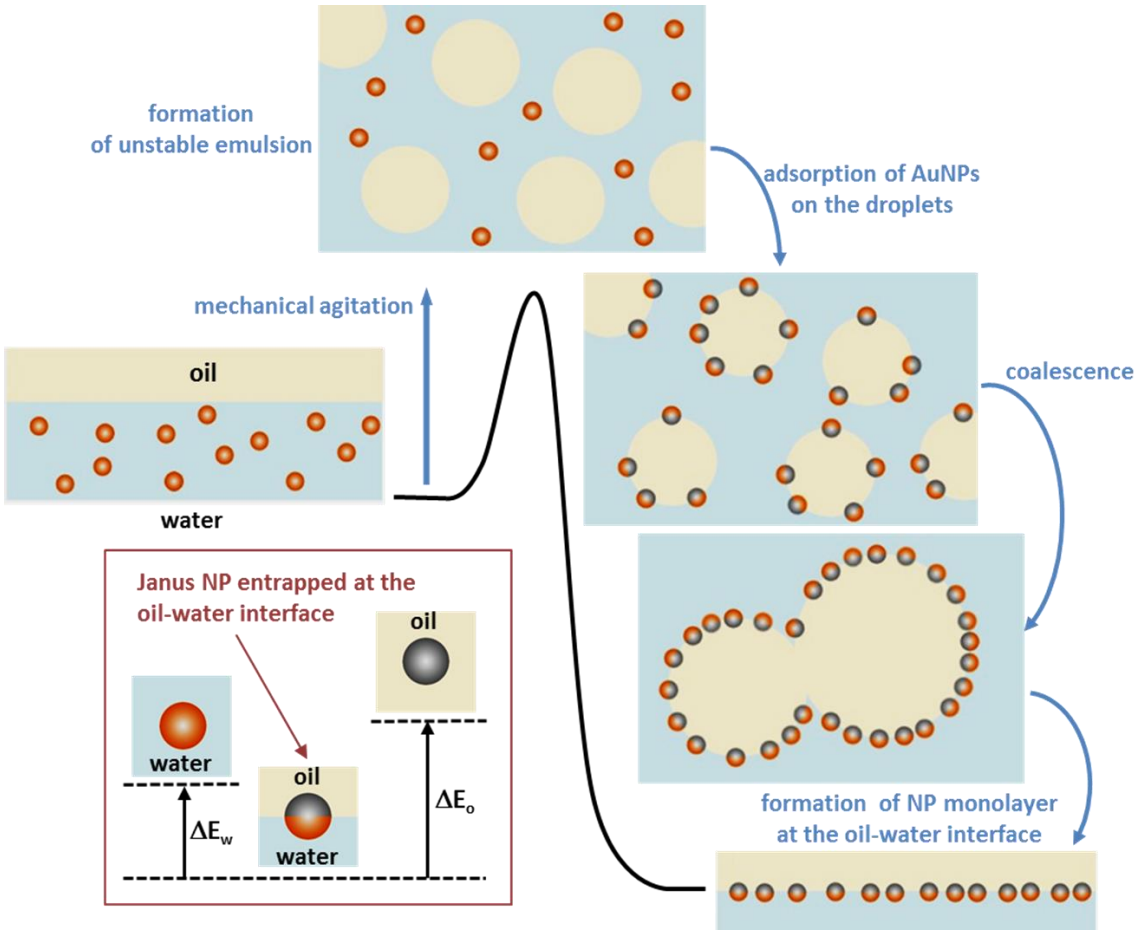

Fig. 44. Explanation of the emulsification-induced adsorption of the AuNPs at the oil−water interface. Transfer of the AuNPs at the oil−water interface requires overcoming an energy barrier due to partial deprotonation of the amine moieties. Formation of an unstable oil-in-water emulsion provides an input of energy necessary to pass this barrier. The AuNPs can adsorb at highly curved surfaces of the hexane droplets. The droplets coalesce to restore the oil−water interface containing adsorbed AuNPs. Inset: Entrapping mechanism. Energy of the Janus-like AuNPs at the oil−water interface is smaller than those in bulk oil and water phases.

The AuNPs coated with aminothiolate ligands that were used possess the ability to alter their surface charge via protonation/deprotonation processes. As a result, the ligands' properties change from highly hydrophilic to hydrophobic, when transferred from acidic aqueous solution to oleic phase. When brought at the interface, the AuNPs exhibit amphiphilic properties. Their hydrophobic portions (covered with deprotonated ligands) face toward the oleic phase, whereas their hydrophilic portions (covered with positively charged ligands) face the aqueous phase. Such a structure of the NP is often referred as to the Janus-like one.[137,

270-277] Note that a similar kind of re-distribution of the surface charge, occurring upon attachment of the AuNPs to the interface, has been reported by Reincke *et al*.[134, 204] In the work cited, charged ligands remained on the hemisphere that was submerged in the water rich phase, and neutral ligands were located on the side immersed in organic phase. Here, the energy needed to transfer the Janus-like AuNP from the interface to the oleic and water phase are, respectively, $\Delta E_w = \pi R^2[2(\gamma_w - \gamma_o) + \gamma_{ow}]$ and $\Delta E_0 = \pi R^2[2(\gamma_o - \gamma_w) + \gamma_{ow}]$. Here γ_o and γ_w denote respectively surface tension of the deprotonated AuNP in oleic phase and protonated AuNP immersed in the aqueous phase. Since the values of the surface tensions γ_o and γ_w are roughly similar, both ΔE_0 and ΔE_w are positive. This follows that the AuNP is entrapped in an energy well. The thermally activated desorption of AuNPs occurs when the depth of the well (the desorption energy) is 5−10 times larger than the thermal energy.[278] Thus, given the high resistance of the monolayer to desorption, one expects that the depth of the energy well in the system considered is many times greater than k_BT. The AuNPs did not exhibit a tendency to transfer from the aqueous to the oleic phase, even at high pH levels. This indicates that $\gamma_o > \gamma_w$ and, consequently, $\Delta E_0 > \Delta E_w$.

The stability of the AuNPs within the monolayer, combined with their ability to create chemical bonds with the cross-linking molecule, is a crucial requirement of the presented fabrication method. Fig. 45 explains the fabrication process.

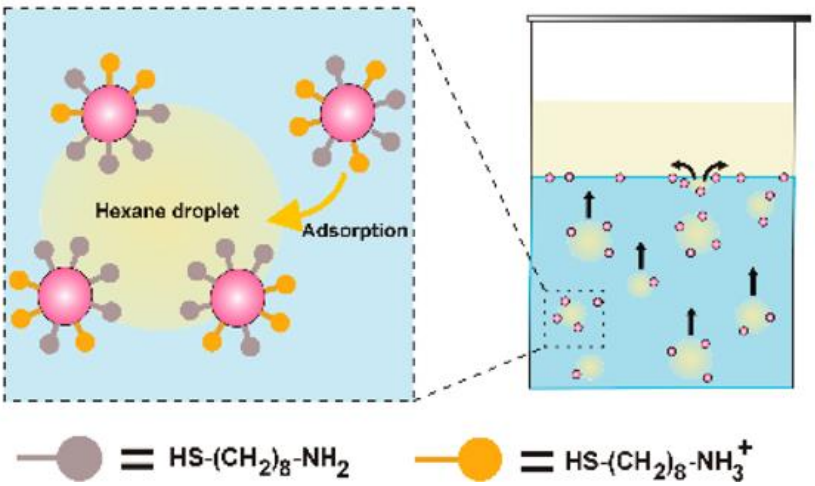

Fig. 45. Transfer of AuNPs at the oil−water interface through the "cargo mechanism". The amphiphilic (Janus-like) character of AuNPs makes them capable of adsorbing on the surface of hexane droplets that migrate to the oil−water interface carrying AuNPs as their "cargo".

3.7.3. Dependence of the NP susceptibility toward migration on the solution pH

In the method presented AuNPs functionalized with aminothiolate ligands were employed. These ligands possess a thiol group at one terminal end and an amino group in the opposite terminal position.[279] The thiol group is used for anchoring of the ligand to the AuNP surface, whereas the amino group is unbound and has the capability of bonding protons in a reversible way. An equilibrium between the protonated and nonprotonated amino groups is established depending on the pH of the solution. At low pH values the AuNPs are strongly protonated. The protonation degree decreases as the pH value rises.[280] The fraction of protonated ligands determines the net surface charge of the AuNPs because the protonation generates a positive charge on the nitrogen atom of the amino group. The possibility of easy tuning of the AuNP hydrophilicity without the need of any chemical change of the AuNPs surface offers a means of facile control of the system. Such AuNPs can be easily dispersed in the aqueous phase and can form very stable monolayers at the oil−water interface as well.

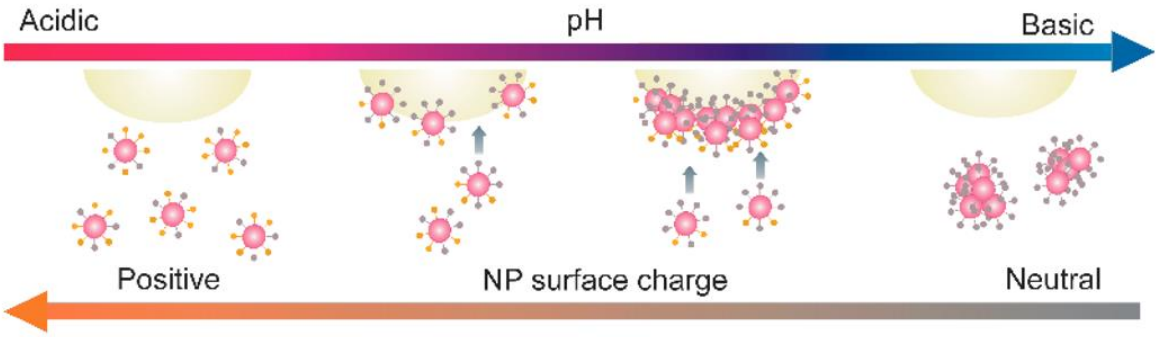

Fig. 46. pH-controlled behavior of AuNPs: At low pH AuNPs do not exhibit a tendency toward adsorption at the hexane droplet−water interface. For the range pH 3−10 they adsorb at the droplets. As pH increases further, a layer of aggregated AuNPs is formed at the interface. Exceedingly high pH levels lead to the bulk aggregation.

The transfer of the AuNPs from the bulk aqueous phase to the oil−water interface takes place only for certain pH levels. At high acidic conditions the AuNPs with a high positive charge are not capable of adsorbing on the surface of the hexane droplets, even under intense mechanical agitation. On the other hand, strongly basic conditions cause bulk aggregation and sedimentation of the AuNPs. Hence, an intermediate value of the protonation must be reached

for the adsorption of the AuNPs to occur (cf. Fig. 46). We found that the "cargo mechanism" is operative for the pH in the range from about 3 to 10.

3.7.4. Monolayer covalent cross-linking process

In my approach, I used a water−hexane binary mixture, which forms a biphasic system. This system consists of two immiscible phases: an oil and a water-rich one. The oil−water interface is used here as a template for the self-assembled AuNP monolayer. In the first step, the AuNPs are introduced onto the oil−water interface. To carry out the cross-linking reaction, the AuNPs have to be brought close enough to each other so that the cross-linking molecule is able to attach itself to the ligands bound to two neighboring AuNPs. The reduction of the interparticle distances is achieved by compression of the oil−water interface area. Because ligands immersed in the aqueous phase are protonated, the AuNPs possess positive surface charge. As a result, the electrical repulsion forces effectively prevent the AuNPs from aggregation. After the compression the AuNPs stay in close proximity to one another within the monolayer, and are prone to cross-linking. Once the interfacial area is sufficiently reduced, the AuNPs are chemically bound to create a stable and robust monolayer. A naphthalene dianhydride derivative, substituted in four positions by alkyl chains (cf. Fig. 47), was employed as the cross-linking agent. The role of the alkyl chains is to increase the solubility of the naphthalene molecule in organic solvents, as it is introduced into the system through the upper oleic phase. The amino terminal groups of the AuNP ligands are capable of forming spontaneously chemical bonds with various functional groups of organic compounds. In particular, they create amide bonds with the anhydride moiety.[281] The presence of the rigid aromatic core separating two reactive groups hiders binding of the linker molecule to the same AuNP. This feature, combined with the fact that the reaction occurs under ambient conditions, makes naphthalene anhydride derivative an effective cross-linking agent. The above described, simple self-designed compression-reaction device built of a polymeric syringe equipped with two pistons was constructed to perform the fabrication process.

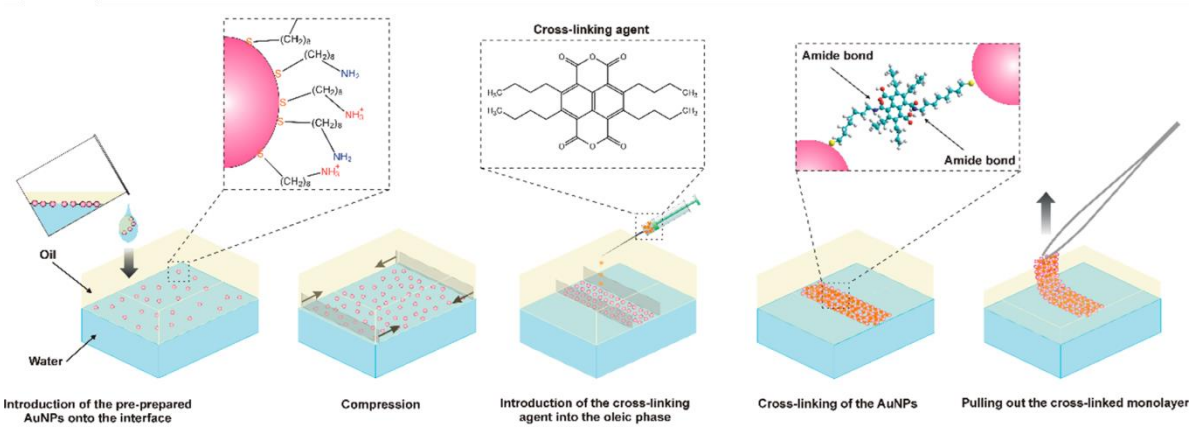

Fig. 47. Method of obtaining the free-standing nanocomposite film. Subsequent steps of the film fabrication process, that include: introduction of NPs to the liquid-liquid interface, interfacial area compression, monolayer cross-linking process in the presence of the cross-linking agent, and finally removal of the stable monolayer from the compression-reaction device.

The mobile pistons placed at both ends of the cylinder enabled facile compression of the AuNP monolayer, and achieving dense packing of the AuNPs that is necessary for the chemical cross-linking. The cross-linking agent was then introduced into the upper oleic phase. After the cross-linking reaction was completed, a uniform film floating at the oil−water interface was formed. As shown in Fig. 50b, the as-obtained film cracked in a fashion typical of brittle materials. The proper amount of the cross-linking agent was adjusted by trial and error to provide efficient cross-linking of the monolayer. An excess amount of the linking molecules leads to coating of the individual AuNPs by the naphthalene derivative molecules. Saturation of the majority of the surface amine groups with one of the two available carboxylic dianhydride moieties blocks formation of the covalent bonds between the adjacent AuNPs. As a result, the integrity of the monolayer film is substantially impaired. On the other hand, a deficient amount of the cross-linker agent makes it impossible to form a sufficient number of connections between the neighboring AuNPs. The obtained film is then very fragile and easily disintegrates.

3.7.5. Cross-linked NP monolayer – the final product

As shown in the SEM experiments, the obtained film is comprised of uniformly distributed, densely-packed AuNPs. Scarce voids and irregularities are visible within the film structure. Such imperfections may be caused by insufficient monodispersity of the NPs or perturbations

occurring during film transferal from the interface onto silicon wafers. Mechanical stress arising during film transferal is also most likely responsible for the generation of the observed large cracks of the film. The shape of this crack displays features characteristic of stiff materials, that is, the sharp mutually matching edges. Such crack shapes are created as a result of a rupture of a brittle solid. The image presented in Fig. 50b provides additional confirmation that within the film the AuNPs are permanently linked through chemical bonds. To further characterize the obtained material, a cross-section of the film transferred from the oil−water interface onto a silicon wafer was investigated with SEM microscopy. The recorded micrographs clearly indicate that the film is composed of a single layer of AuNPs spread uniformly over the silicon substrate. Additional characterization of the film was achieved by performing STEM experiments, after the deposition of the film on a TEM grid. The obtained micrographs of the free-standing film confirm the covalent nature of the interparticle bonds between adjacent NPs. These bonds provide the monolayer film with the necessary stability to withstand harsh conditions (e.g. during film rinsing, under the influence of an electron beam) and guarantee the films durability even when extended over holes of a porous grid, and lacking support from the bottom. The STEM micrographs reveal patches, having the size of a few micrometers that span over the grid surface. Individual AuNPs within the monolayers form a densely packed structure, with visible characteristic sharp-edged cracks. Such cracks are typically formed as a result of a rupture of a stiff material. Note here that similar fracture patterns have also been observed [282] for NP monolayers that were not covalently cross-linked. However, these films were deposited on solid substrates, where the adhesion of the NPs to the solid support strongly affected the mechanical properties of the deposited monolayer. The film shown in Fig. 51 is spread over a porous carbon layer, and its large portions are free-standing. These unsupported fragments of the film have contact with the solid support only at the peripheries of the holes. One may expect that if this film was not bound covalently, mechanical stress would lead rather to its bursting instead of cracking in the absence of stabilizing solid support. The STEM analysis showed that the nanocomposite film possesses both mechanical and chemical durability. It proved to be resistant to the mechanical stress associated with the deposition on the TEM grid and could withstand intense rinsing in pure chloroform. The fact that the deposited monolayer films sustained their integrity during the washing in chloroform provides a strong confirmation of the covalent cross-linking of the AuNPs. If the film was noncovalently bound, it would instantly dissolve

and rupture. Cracking of the obtained film may be caused by the evaporation of residues of the solvent. The solvent evaporation gives rise to the shrinkage of the film and, consequently, produces compressive stress.

The film was subjected to electron beam radiation during the SEM/STEM experiments. The monolayer membrane exhibited good resistance to this degrading stimuli. Fairly mild shrinking of the film took place, which was caused most probably by burning off of the organic matter. Remarkably, the free-standing film did deform, but bursting did not occur. Such high durability of the film provides a premise that the AuNPs are covalently bound to each other within the monolayer. Although the durability of the free-standing membranes is a good premise of their high mechanical stability, meticulous investigation should be carried out to characterize the mechanical properties of these films. A remark on the stability of the obtained film in the high electron beam is in order here: The described composite material is comprised of inorganic NPs linked covalently together via relatively large organic linkers. The distance between adjacent NPs corresponds roughly to the double length of the surface ligands and the cross-linking agent, which equals about 2.5 nm. For comparison, the diameter of the NP cores is about 6.0 nm. This means that the organic fraction in our composite film is quite large. Due to relatively low durability of organic matter against exposure to degrading factors (high voltage electron beam), such films possess lower resistance to degradation under harsh conditions as compared to films composed of mainly inorganic moieties. The degradation of the organic matter is responsible for the observed steady drift/shrinkage of the freestanding film during high voltage electron beam irradiation. This drift unavoidably deteriorates the quality of the images. Similar destructive effect of the electron beam on organic matter has already been described.[283] Reports presenting good quality TEM images of free-standing NP membranes describe materials composed of either multiple layers of NPs [284] or monolayers of nanoobjects much larger than those used in this study.[285] The multilayer NP sheets reported in ref. 284 possess a thickness of tens of nanometers which accounts for their increased robustness toward the SEM electron beam. The significantly larger surface area of bulkier nanoobjects reported in ref. 285 leads to their stronger stabilization (through van der Waals forces) in the organic matrix. Also, the character of the NP− matrix interactions must be taken into account when considering the films' resistance in highly degrading conditions. In our study, the NPs are connected with the matrix at a few points via linkers. The electron beam is less destructive to films bound via van der Waals

forces, where numerous weak interactions contribute to the integrity of the film, as compared to films bound by strong but sparse covalent bonds. In the second case the destruction of a small fraction of the bonds may lead to the discernible disintegration of the membrane.

3.7.6. Demonstration of the mechanical properties of the cross-linked AuNP monolayer

To characterize further mechanical properties of the nanocomposite film, its resistance to deformations was investigated. For this purpose experiments in which the obtained cross-linked film located at the oil−water interface in the compression-reaction device underwent deformations caused by the changes of the curvature of the interface were performed. The shape of the interface was changed by reducing the distance between the pistons. As a result, the curvature of the interface increased and induced bending of the film. The film was found to withstand quite significant increase of the curvature without loss of its integrity (Fig. 49). The tearing of the cross-linked monolayer occurred at the points that correspond to the highest mean curvature of the interface. These points were situated in the vicinity of the pistons, at both ends of the syringe. The generated cracks crossed the whole width of the monolayer membrane. These characteristic sharply edged cracks, also referred to as the channel cracks, indicate brittleness of the obtained membrane. Based on the profile of the interface at the longitudinal cross-section of the cylinder, the critical radius of the curvature was estimated as about 5 mm. One should keep in mind that the AuNP monolayer was cross-linked at a curved interface. For this reason the bending stress was due only to the deformations relative to the initial shape of the oil−water interface. This result indicates that the nanocomposite film is a quite flexible material.

To demonstrate the robustness of the film, we transferred it onto a piece of brass wire mesh (mesh size, 0.4 mm; wire diameter, 0.2 mm). As shown in Fig. 48a, the monolayer covered some portion of the mesh, and displayed characteristic golden gloss. However, probably due to the solvent evaporation stress, the deposited film was fairly unstable and exhibited a tendency to rupture. The film transferred onto the TEM grid with smaller mesh size (48 μm) was substantially more stable (Fig. 48b).

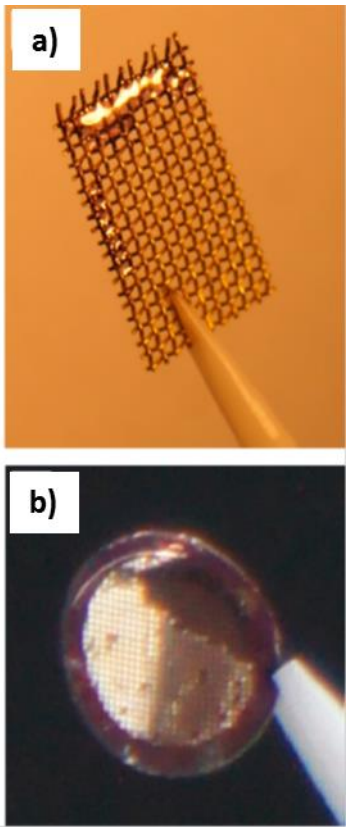

Fig. 48. (a) Photograph of the film deposited on a brass wire mesh (mesh size, 0.4 mm), and (b) TEM grid (mesh size, 48 μm).

To capture the changes occurring at the interface during film deformation, following the increase of interfacial curvature, multiple high-resolution digital photographs of the interface were taken. As can be clearly seen in the captured digital photographs, tearing of the cross-linked monolayer occurred in two places near the pistons, in the portions of the film corresponding to the highest local mean curvature. Importantly, the resulting cracks, indicated by the white arrows in Fig. 49, run across the whole sample, from one wall of the syringe to another.

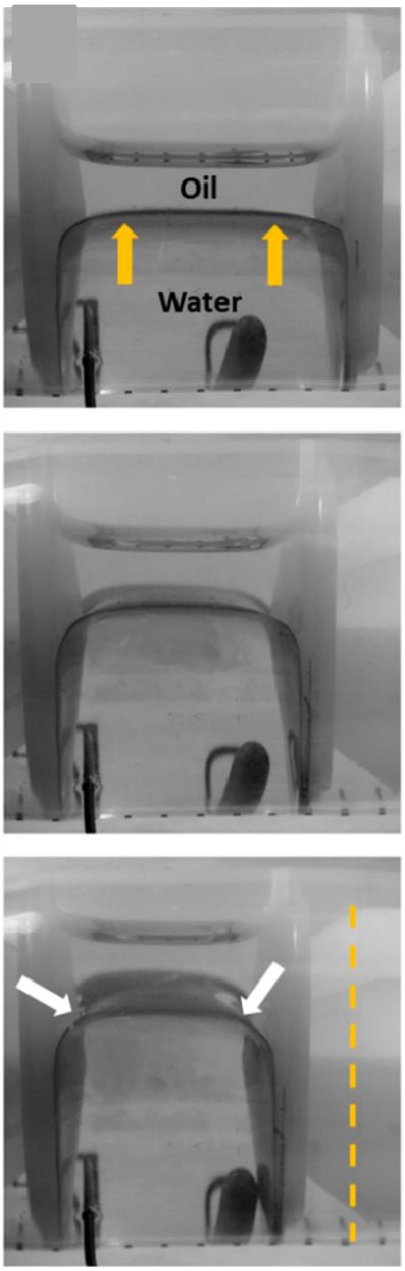

Fig. 49. Demonstration of mechanical properties of the AuNP monolayer. Subsequent stages of the deformations of the film located at the oil−water interface. The yellow dashed line represents the initial position of the mobile piston. When the mean curvature attained a critical value, the film cracked in two places indicated by the white arrows. The yellow arrows indicate their initial positions. The outer diameter of the cylinder is 3 cm.

Tearing of the cross-linked monolayer film occurred in two sites in close proximity of the pistons. The created cracks run across the entire sample and their positions correspond to the highest local mean curvature.

3.7.7. Structural analysis of the 2D nanocomposites

SEM

Investigation of the NP ordering within the cross-linked NP monolayer was achieved via SEM microscopy experiments. Arrangement of NPs was examined at high magnifications. SEM micrographs of the nanofilm's cross-section provided evidence that the obtained 2D nanocomposite was indeed composed of a single layer of NPs. Representative SEM images of cross-linked AuNP monolayer deposited on silicon are shown in Fig. 50.

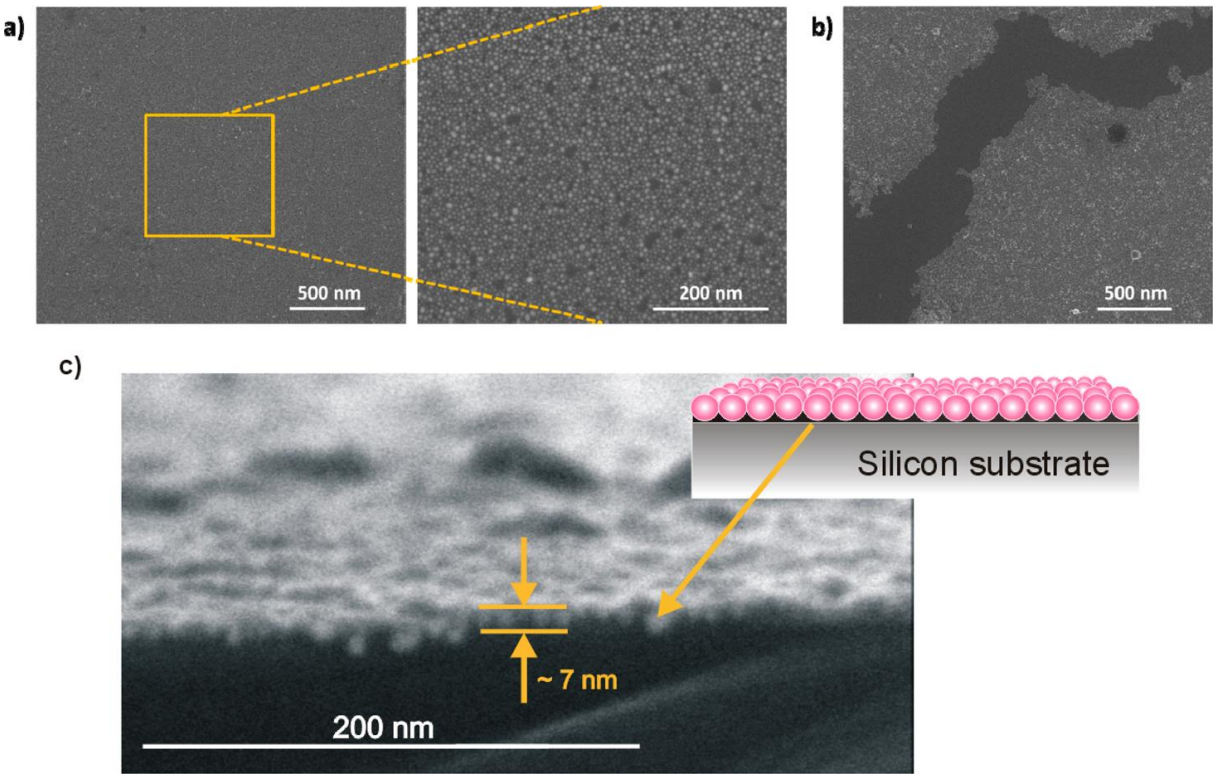

Fig. 50. SEM images of the cross-linked AuNP monolayers deposited on a silicon substrate. (a) Structure of a uniform film. (b) Shape of the crack indicating that the film broke in a way characteristic of a solid. (c) SEM image of the AuNP film deposited on a silicon substrate viewed at approximately a 90° angle demonstrating its monolayer structure.

As can be seen, relatively big uniform portions of the film, up to 12 × 12 μm^2, were successfully transferred from the oil−water interface onto the substrate. Higher magnification of the square area marked in Fig. 50a reveals fairly dense packing of the AuNPs within the monolayer, which is close to the hexagonal ordering. Voids occupy only a relatively small

fraction of the film area. The irregularities in the short-distance arrangement of the AuNPs are likely caused by their polydispersity. Fig. 50b shows a crack in the monolayer caused by mechanical stress arising during the deposition process and evaporation of the solvent from the deposited film.

Images of the nanocomposite's cross-section were also recorded after its transferal from the oil−water interface onto a silicon wafer. The obtained images clearly show that the film is composed of a single layer of AuNPs spread uniformly over the silicon substrate (Fig. 50c). The thickness of the monolayer estimated by the cross-sectional SEM image is ∼7 nm. This value is slightly bigger than the average AuNP core diameter (6.0 nm) and smaller than the diameter of the AuNP coated with the C8 aminothiolate ligand, AuNP core + 2 × ligand length = (6.0 + 2 × 1.14) nm = 8.28 nm. One expects that the apparent size of the AuNPs, due to the deformations of the coating layer, should be smaller than that calculated based on the AuNP core diameter and the ligand length. Thus, the size obtained from the cross-sectional SEM images agrees – within the measurement uncertainty (about ±1 nm) – with the estimated diameter of the C8-coated AuNPs.

STEM

To further characterize the nanocomposite film, the crosslinked AuNP monolayer was deposited on a TEM grid according to the method described in the Experimental Section and then analyzed with scanning electron transmission microscopy (STEM). It should be noted that, importantly, in the TEM grids used in the described experiments, there was no polymer layer beneath the carbon film. That is, the AuNP monolayer spreading over the holes in the carbon film was completely unsupported. The STEM micrographs that are shown in Fig. 51 provide direct proof that the cross-linked monolayer transferred onto the TEM grid forms a free-standing film.

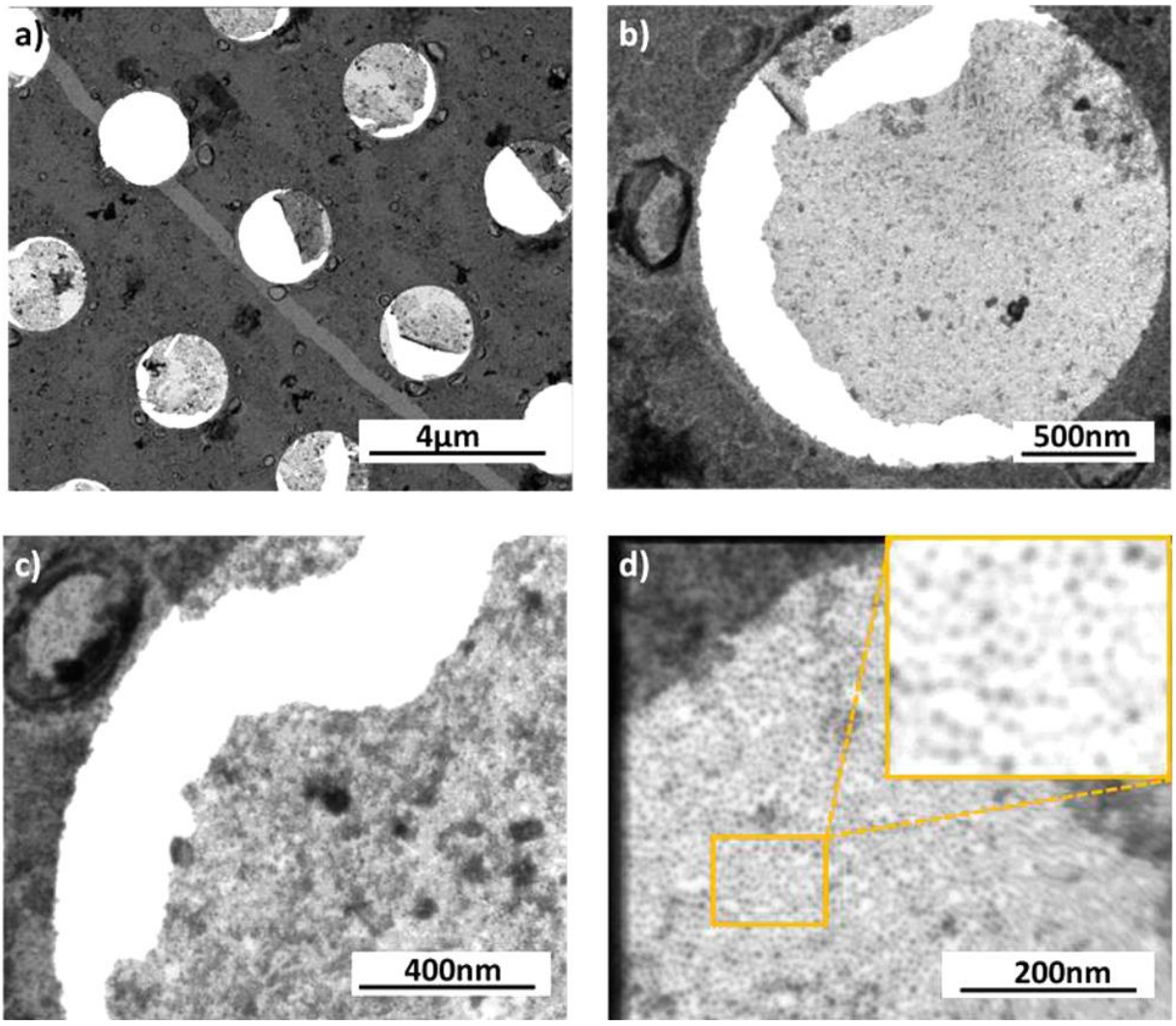

Fig. 51. STEM micrographs of the nanocomposite film deposited on a TEM grid. (a) Large-scale view of the grid covered by the film. (b−d) Subsequent magnifications of the free-standing film spanning over a hole in the grid.

As can be seen in this figure, the obtained structure is composed of patches of monolayers of the AuNPs. These patches have sizes of a few micrometers and span over the grid surface. Note that the film displays characteristic sharp-edged cracks that are usually formed as a result of a rupture of a stiff material. Magnifications of the film presented in Fig. 51d reveal also that within the monolayers the individual AuNPs form a densely packed structure identical to that shown in the SEM image in Fig. 50a. Note here that similar fracture patterns have also been observed [282] for NP monolayers that were not covalently cross-linked. However, these films were deposited on solid substrates, where the adhesion of the NPs to the solid support strongly affected the mechanical properties of the deposited monolayer. The

film shown in Fig. 51 is spread over a porous carbon layer, and its large portions are free-standing. These unsupported fragments of the film have contact with the solid support only at the peripheries of the holes. One may expect that if this film was not bound covalently, mechanical stress would lead rather to its bursting instead of cracking in the absence of stabilizing solid support. The STEM analysis showed that the nanocomposite film possesses both mechanical and chemical durability. It proved to be resistant to the mechanical stress associated with the deposition on the TEM grid and could withstand intense rinsing in pure chloroform. The fact that the deposited monolayer films sustained their integrity during the washing in chloroform provides additional confirmation of the covalent cross-linking of the AuNPs. If the film was noncovalently bound, it would instantly dissolve and rupture. The cracking of the film that can be seen in Fig. 51a was most likely caused by the evaporation of residues of the solvent. The solvent evaporation gives rise to the shrinkage of the film and, consequently, produces compressive stress. Also, the composite film could withstand quite well an exposure to the high voltage STEM electron radiation. This was demonstrated in a movie recorded during the STEM analysis, showing the free-standing monolayer stretched over the TEM grid hole treated with a high energy electron beam.

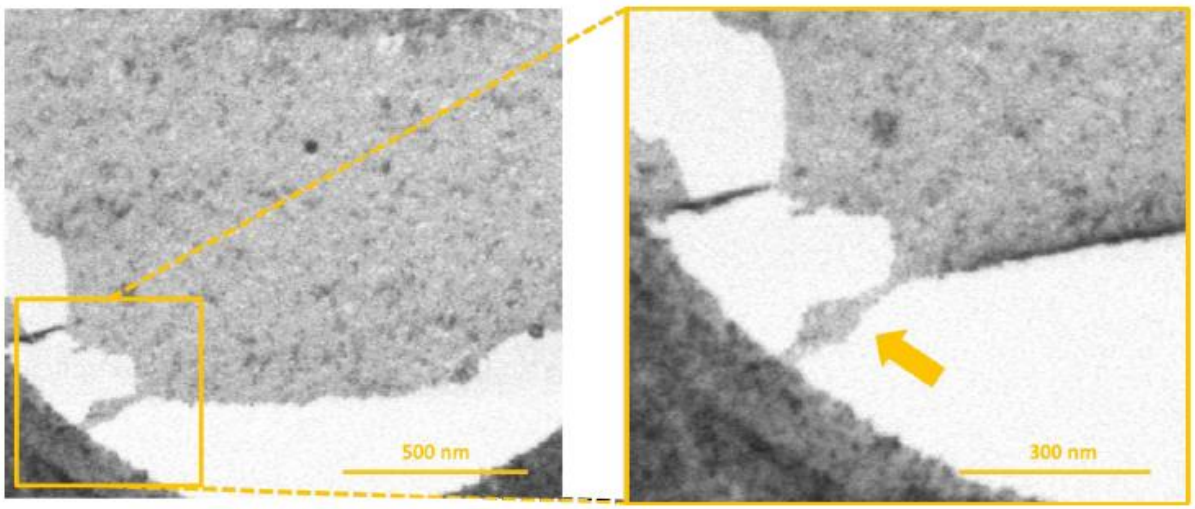

Fig. 52. STEM micrographs showing small portion of AuNP free-standing film. The film stretches under the exposure to a high voltage electron beam, but does not break apart. The arrow indicates strongly stretched portion of the film, which, despite the strong deformation, still sustained its integrity.

Snapshots of this movie exposing shrinking of the film are shown on Fig. 53. The movie reveals that only some shrinking of the film took place, which was caused most probably by

burning off of the organic matter. A steady drift/shrinkage of the freestanding film were clearly seen in the STEM movie.

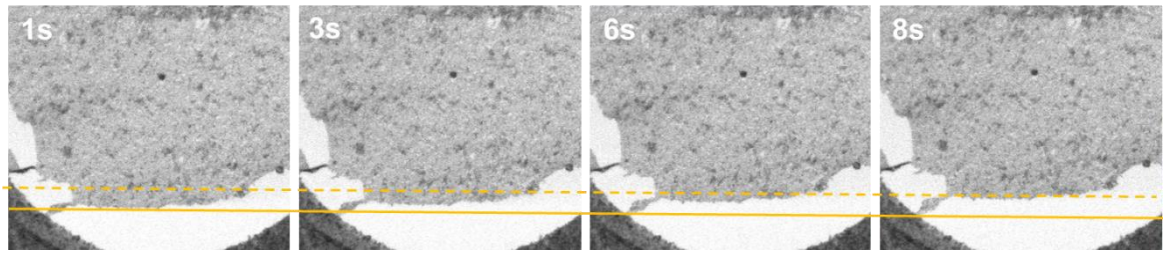

Fig. 53 Subsequent snapshots of the movie recorded during exposition of the thin film to a high voltage electron beam of the STEM. The continuous yellow line indicates the position of the film's edge at the beginning of the experiment, whereas the dashed line indicates it's position after the exposition to an electron beam. The elapsed time of beam exposure is indicated in the top left corner. Shrinking of the film is clearly visible.

3.8. 3D nanostructures - nanocomposites by covalent bonding between noble metal nanoparticles and polymer matrix

This section describes the developed method of chemical linking of ex-situ prepared noble metallic NPs to various polymer matrices (Fig. 54). In the presented method a binding reaction occurs between the NPs functionalized with aminothioalkyl ligands and polymers containing at least one of the following reactive functional groups in their structure: the aldehyde, carboxyl acid, or anhydride acid group or hydroxyl groups that can be oxidized to carbonyl groups in the reaction conditions. The synthetic procedure details are given and the structural analysis (performed via SEM, NMR, FTIR) results are discussed. Finally, a plausible role of the NPs in the covalent bond formation reaction is proposed.

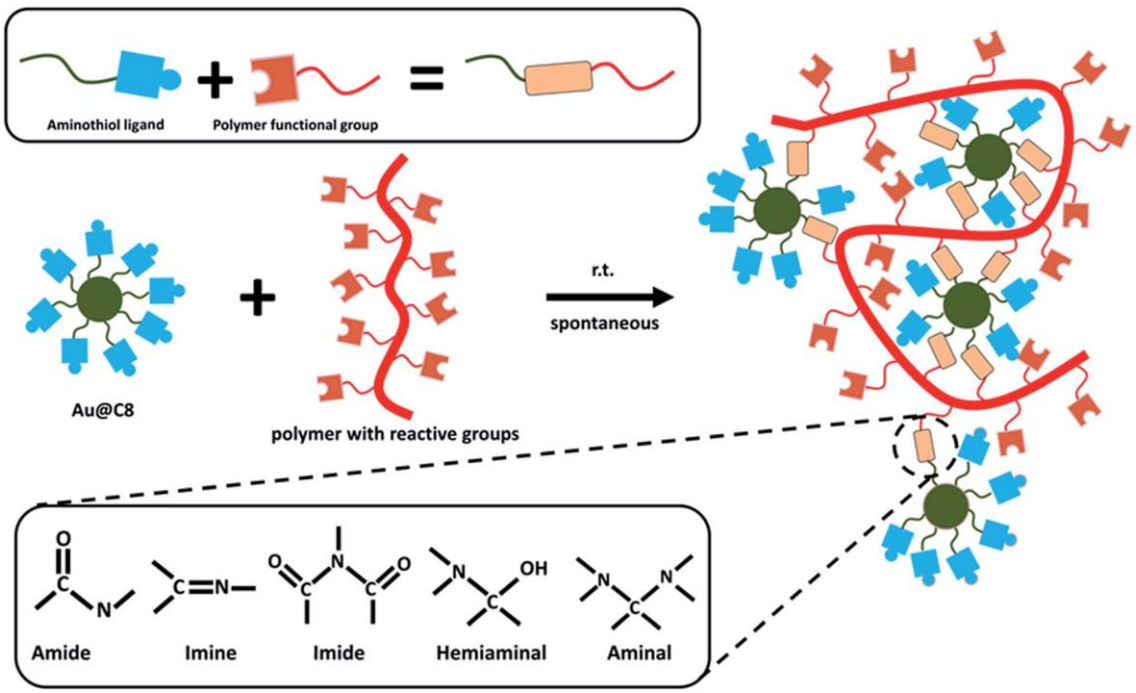

Fig. 54. Schematic illustration of the nanocomposite fabrication via spontaneous covalent bond formation between NPs' capping ligands and polymer functional groups.

3.8.1. Nanocomposite preparation

As in the case of 2D nanocomposites, for the fabrication of 3D materials NPs functionalized with C8 were utilized. In this case of the C8 ligand, a favorable proportion between the stability of the NPs and the amount of charged, unreactive surface groups can be easily achieved. In contrast, the C12 ligand due to the length of its aliphatic chain requires a higher degree of surface protonation to warrant sufficient stability in aqueous environments. This also contributes to the increased difficulty of the NP functionalization procedure, which should be conducted at elevated temperatures. Therefore, the ratio of protonated to deprotonated surface ligands on an individual NP must be higher as compared to the C8 ligand to achieve the same stability. This could lead to a decreased efficiency of the NP – polymer matrix binding process, due to the reduced amount of reactive, deprotonated ligands on the NP surface. On the other hand, experiments show that the lowest stability in aqueous environments is observable in case of the C4 functionalized NPs. This is indicated by the darker, violet shade of the Au@C4 solution, as compared to the NPs passivated with other molecules used in the research described herein. Such NPs are inadequate for nanocomposite

fabrication as aggregation begins to occur in the NP solution prior to the 3D nanocomposite preparation process.

3.8.1.1. Preparation of the starch-based composites

To obtain the powder starch–AuNPs nanocomposite, to 0.5 g of potato starch 5 mL of distilled water was added at room temperature. Then 10 mL of aqueous solution of Au@C8 (10^{-8} mol NPs L^{-1}) functionalized with aminothioalkyl ligands was injected under continuous stirring. Once the sediments settled on the bottom of the vial, the red color of the solution vanished and the solution became colorless. At the same time, the white precipitate of starch turned pink. The clear solvent was then decanted and the remaining residue, washed three times with distilled water and then left to dry at 55 °C for 12 h and then 85 °C for another 3 h. To obtain the free-floating starch–AuNPs nanocomposite film, to 20 mL of distilled water heated up to 85 °C 1 mL of starch suspension (0.1 g mL^{-1}) was added under intensive stirring. The obtained solution was stirred for 1h at elevated temperature. During this time the solution gradually became uniform and lucid. Into another vail 5 mL of AuNPs functionalized with aminothioalkyl ligand (Au@C4 or Au@C8) was added, and the solution was heated to 85 °C. Then, 1 mL of the clear starch solution prepared in the previous step was added, and the obtained mixture was stirred at 85 °C for another 10 min. Next, the sample was cooled to room temperature and 3 mL of methanol were added dropwise, upon which clouding of the solution was observed. The mixture was then centrifuged at 9000 rpm for 15 min. Next, the supernatant was removed, and to the remaining residue (the starch-NPs film) methanol:water mixtures of the ratios (1:1), (3:1), and (1:0) (v/v) were subsequently added. The mixtures of increasing methanol content were employed to change gradually the polarity of the solvent and facilitate peeling off the film from the vial walls. After each addition of the methanol:water mixture the obtained solution was left for 0.5 h at room temperature. Finally, the starch-NPs film formed during the centrifugation was detached from the polymer vial walls.

3.8.1.2. Synthesis of the PVA-based composite film

To obtain the PVA-based nanocomposites (Fig. 65c), an aqueous solution of PVA was prepared (50 mg mL^{-1}) by dissolving 250 mg of the polymer in 5 mL of water heated up to

70 °C. 3 mL of Au@C8 aqueous solution (10^{-8} mol NPs L^{-1}) was then added to the PVA solution and the mixture was stirred for 10 min at 70 °C. Finally, the obtained solution was poured into 50 mL of methanol upon which a precipitate of the composite was obtained. The PVA–AuNPs film was prepared by dissolving 2.5 g of PVA in 20 mL of aqueous solution of AuNPs functionalized with aminothioalkyl ligand (Au@C8 or Au@C12) acidified with 0.4 mL 0.8 M hydrochloric acid. The obtained solution was then heated to 75 °C and kept at this temperature for 20 min under continuous stirring. After this time the solution was centrifuged at 5000 rpm for 15 min. To 3 mL of the obtained supernatant 0.5 mL of 86% glycerin was added. Next, the solution was poured onto a polystyrene hydrophobic polymeric Petri dish and dried at 60 °C during 24 h. The obtained film could be easily peeled off the Petri dish with tweezers.

3.8.1.3. Synthesis of the cellulose-based composites

During the preparation of the cellulose-based composite (Fig. 65f) a piece of cellulose paper (165 mg) was cut and placed in a glass vail. 5 mL of Au@C8 aqueous solution (10^{-8} mol NPs L^{-1}) was then added into the vial and the obtained mixture was left for 12 h. During this time gradual lightening of the red color of the solution was observed due to the attachment of the NPs to the surface of the paper. At the same time, the color of the paper strip turned pink. After 12 h the paper was removed from the solution. After immersing this paper in distilled water the solution remained clear and colorless which confirmed that the detachment of the NPs did not occur.

3.8.1.4. Synthesis of the carboxylmethylcelullose-based composites

To conduct the binding of the metallic NPs (Au@C8) to the carboxylmethylcelullose (CMC) (Fig. 65c), 156.7 mg of CMC was added to 10 mL of an aqueous solution of Au@C8 (10^{-8} mol NPs L^{-1}) under continuous stirring. After 30 min the mixture was poured onto a polystyrene hydrophobic Petri dish and left until complete evaporation of the solvent at 70˚C. After the water evaporation the obtained film was peeled off.

3.8.1.5. Synthesis of the P[MA-co-S]-based composites

The P[MA-co-S] copolymer is composed of maleic anhydride and styrene. The P[MA-co-S]-based composite was synthesized by adding 5 mL of Au@C8 aqueous solution (10^{-8} mol NPs L^{-1}) to 10.5 mg of the polymer. The polymer did not dissolve in the aqueous solution of the AuNPs, but gradual lightening of the initial red color of the solution was observed, indicating the attachment of the AuNPs to the surface of the solid polymer. After 12 h the reddish precipitate was decanted and washed thrice with distilled water to remove any unbound NPs.

3.8.1.6. Synthesis of PVA nanomaterials functionalized with metallic NPs coated with C8 ligand (Ag@C8, Au@C8, Pt@C8)

To functionalize PVA with metallic NPs, 10 mL of methanol and 1 mL of aqueous NaOH (0.4 M) were added to 100 mg of PVA polymer. The obtained suspension was kept at room temperature for 15 min, then the supernatant was removed, and to the remaining precipitate again 10 mL of methanol and 1 mL of NaOH (0.4 M) were added. The suspension was heated in a water bath at 50 °C during 3 min and then kept at room temperature for another 10 min. After this time the supernatant was removed. In the next steps, appropriate solution of NPs functionalized with C8 ligand were added to the basified PVA polymer. For AgNPs and AuNPs, the NPs were gradually added by repeated addition of 10 mL of methanol, 2 mL of aqueous solution of metallic NPs (Ag@C8 or Au@C8) and 0.2 mL of aqueous NaOH solution (0.4 M) (in case of first two repetitions), letting the solution set for 10 min, before centrifugation at 9000 rpm during 5 min and subsequent removing of the supernatant. This procedure was repeated 17 times for Au@C8, and 20 times for Ag@C8. In case of the Pt@C8, the PtNPs solution required concentration before the functionalization with the C8 ligand. To carry out the functionalization, 1 mL of aqueous solution of C8 ligand (10 mM) was acidified with hydrochloric acid (0.8 M). The obtained solution was heated to 80 °C in a water bath and 3 mL of the concentrated solution of PtNPs were gradually added, in 100 mL portions. Once functionalized with the appropriate ligand the solution of Pt@C8 was added gradually to the basified PVA polymer by adding in subsequent steps (a) 10 mL methanol, 1 mL of Pt@C8 and 0.6 mL NaOH (aq) (0.4 M) (b) 10 mL methanol, 1 mL Pt@C8, 0.6 mL of NaOH (aq) (c) 10 mL methanol, 1 mL Pt@C8, 0.8 mL NaOH (aq) (0.4 M) (d) 10 mL methanol, 1 mL Pt@C8, 0.6 mL NaOH (aq) (0.4 M). Each time the resulting solutions were

slightly basic. After the addition of Au@C8, Ag@C8, or Pt@C8 the obtained solution was kept for 10 min at room temperatures to allow the NPs to bind with the matrix. Gradual vanishing of the red (Au@C8), orange (Ag@C8) or greenish (Pt@C8) color of the solution and darkening of the precipitate accompanied this process. Finally, the obtained dark red PVA–Au@C8, dark orange PVA–Ag@C8 or greenish PVA–Pt@C8 precipitate was washed three times with 10 mL of methanol. The precipitate was dried at 3 h under vacuum at room temperature. Half of the obtained PVA–Au@C8 was then sintered at 80 °C during 12 h.

3.8.1.7. Preparation of PVA-based nanomaterials functionalized with unbound aminothiolalkyl ligand C8

An aqueous solution of aminothioalkyl C8 (10 mM) was prepared in the first step by mixing together 3.9 mg of 8-aminooctan-1-thiol in the form of hydrochloride salt, 2 mL of distilled water, and 25 mL of aqueous HCl solution (0.8 M). Then, from the obtained solutions, mixtures for the functionalization of PVA were prepared by mixing 22 mL of distilled water, 171 µL the C8 ligand solution (10 mM) prepared in the previous step, and 96 µL of aqueous solution of HCl (0.8 M). In the next step, PVA was basified by adding 10 mL of methanol and 1 mL of aqueous NaOH (0.4 M) to 100 mg of PVA polymer. The obtained suspension was kept at room temperature for 15 min, then the supernatant was removed and to the remaining precipitate again 10 mL of methanol and 1 mL of NaOH (0.4 M) were added. The suspension was heated in a water bath at 50 °C during 3 min and then kept at room temperature for another 10 min. After this time the supernatant was removed. In the following steps the solution of the C8 ligand was added gradually by adding each time 10 mL of methanol, 2 mL of aqueous solution of amine derivative (C8) and 0.2 mL of aqueous NaOH solution (0.4 M) (in case of first two repetitions), letting the solution set for 10 min, before centrifugation at 9000 rpm for 5 min, followed by removal of the supernatant. This procedure was repeated 17 times. Finally, the obtained white precipitate was washed three times with 10 mL of methanol. The precipitate was dried for 3 h under vacuum at room temperature.

3.8.2. Structural analysis of the 3D nanocomposites

3.8.2.1. FTIR

Starch-based nanocomposite

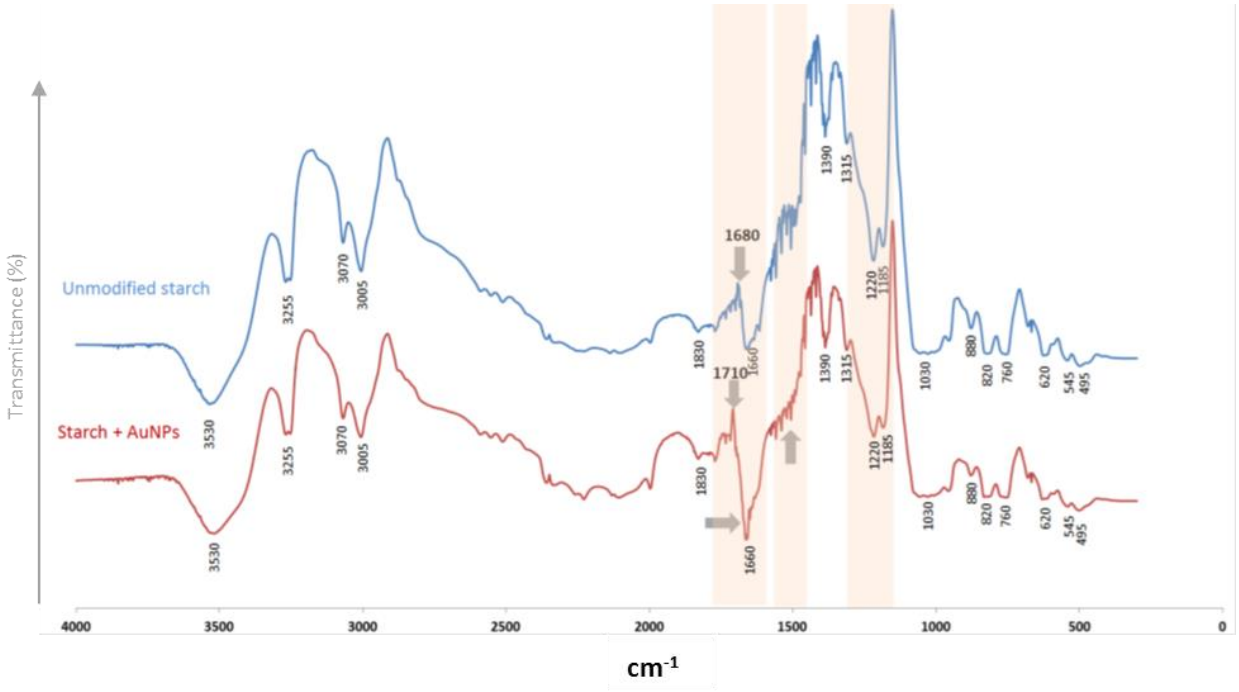

Fig. 55. FTIR spectrum of potato starch and potato starch-AuNPs nanocomposite.

Fig. 55 depicts a comparative graph showing FTIR spectra of the obtained starch-based nanocomposite, and the unmodified polymer matrix (i.e. virgin starch). Areas where differences are visible are marked by an pink tint. Arrows indicate the position of bands that are altered as a result of the formation of covalent bonds between the NPs' surface ligands and active groups of polymer matrix. A new peak located at around 1680 cm^{-1} emerged in the spectrum of the AuNP-modified starch, visible as a widening of the neighboring band. Also, substantial increase of the intensity of the peak located near 1665 cm^{-1} is observed. This provides a clear evidence of the formation of the imine bonds.[286] A slight widening of the peak in the 1220 cm^{-1} region, as well as the appearance of the peaks in the band 1500-1560 cm^{-1} is visible. Both these peaks are due to the terminal amino groups of the ligands on the NPs' surface. These ligands are not bound chemically to the polymer matrix. However, they prove the presence of the functionalized NPs in the matrix.

PVA-based nanocomposites

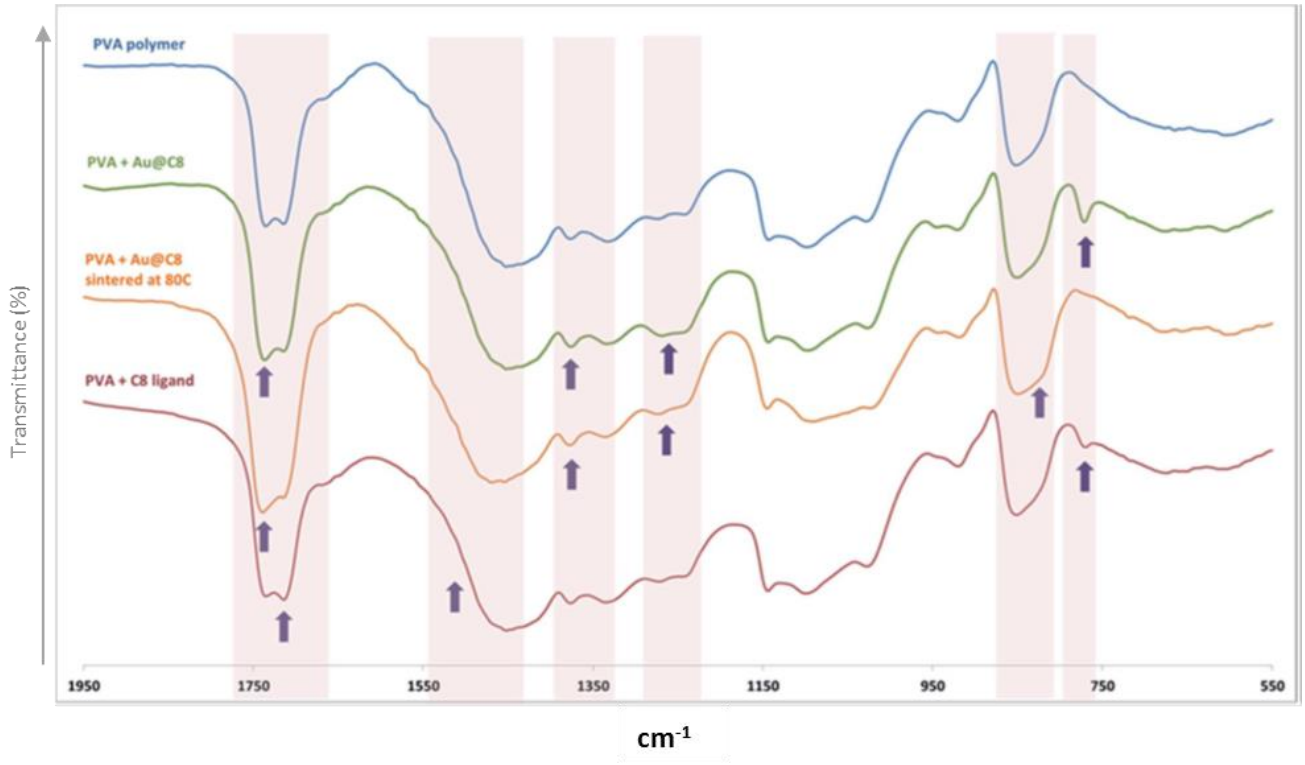

Fig. 56. FTIR spectra of (from top to bottom): unmodified PVA polymer, PVA–Au@C8, PVA–Au@C8 sintered at 80 ˚C, PVA modified with free C8.

Fig. 56 depicts a comparative graph showing FTIR spectra of the obtained PVA-based nanocomposites, and the unmodified polymer matrix (i.e. virgin PVA). Areas where differences are visible are marked by a pink tint. Arrows indicate bands with a higher intensity, as compared to the band intensity of the unmodified polymer matrix. The peak at 1760 cm^{-1} corresponds to aldehyde groups existing within the polymeric backbone. A comparison of the FTIR spectra of unmodified PVA and PVA-Au@C8 clearly show visible differences indicating the formation of new covalent bonds in the latter case. A considerable intensification of the signals at 1735 and 1240 cm^{-1} is noticeable. These signals correspond to the imide or secondary amide groups in the solid state.[286] The strong band at 1735 cm^{-1} is a sum of two overlaying bands: a band of the aliphatic secondary amides, which is usually visible as a strong band at 1650–1630 cm^{-1}, and an imide band adsorbing at higher frequencies, up to 1740 cm^{-1}.[286] The signal at 1240 cm^{-1} is characteristic for imides in the solid phase and is due to the C–N stretching of the imide group. An important change in the spectrum after the functionalization is also discernible as a widening of the broad signal at

around 1435 cm^{-1}. It is caused by the overlaying of this signal with the characteristic secondary amide band occurring in the band 1565–1475 cm^{-1}.[287] Also, widening of the signal at 848 cm^{-1} is associated with the appearance of a secondary amide band related with the N–H wagging vibration.[288] Note that the other characteristic amide bands that are located at around 3400 cm^{-1} are not visible due to the presence of the wide peak associated with hydroxyl groups in the PVA structure.

The FTIR spectrum of the PVA–Au@C8 nanocomposite after sintering at 80 °C was also recorded. As can be seen in Fig. 56, after the exposure to the elevated temperature, the signal at 765 cm^{-1} that is due to the $–NH_3^+$ rocking of amine salts, disappears. This signal originates from a fraction of the amine groups that form carboxylate aminium salts with acidic groups. Other characteristic amine salt signals (in the bands 3550–3355, 3350– 3150, and 1560–1625 cm^{-1}) are covered by polymer and water bands.

Compared to the spectrum of the unmodified PVA polymer, the FTIR spectrum of PVA-C8, being the product of reaction between PVA polymer and unbound C8 ligands (synthesized without the presence of NPs), exhibits growth of the intensity of the right branch of the doublet signal at about 1710 cm^{-1}, which is characteristic for protonated imines.[286] The FTIR spectrum of PVA-C8 displays also the presence of carboxylate aminium salt, evidenced by the signal at 765 cm^{-1} corresponding to the rocking of $–NH_3^+$ group.

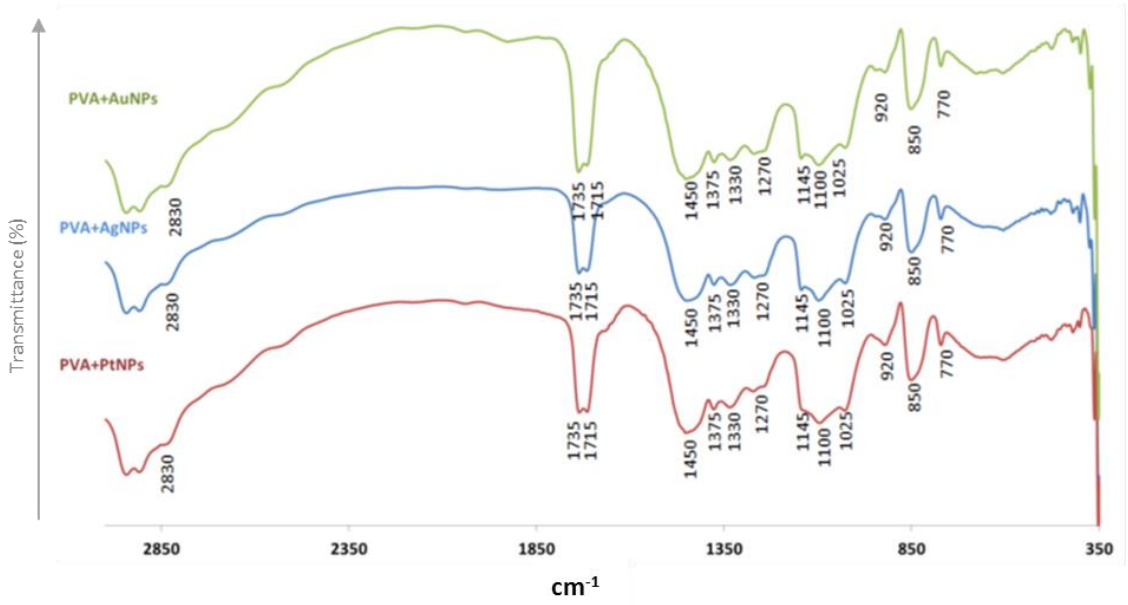

Fig. 57. FTIR spectrum of PVA polymer modified with AuNPs, AgNPs or PtNPs.

Fig. 57 shows a comparative graph showing FTIR spectra of PVA-based nanocomposites obtained using different metallic NPs (Au, Ag, Pt). The FTIR spectra of PVA–Ag@C8 and PVA–Pt@C8 composites were quite similar to that of the PVA–Au@C8, displaying signals of amide and imide bonds, including the appearance of signals at 1735 cm^{-1} and 1240 cm^{-1}, as well as widening of signals as 1435 and 848 cm^{-1}.

- *P[MA-co-S]-based nanocomposites*

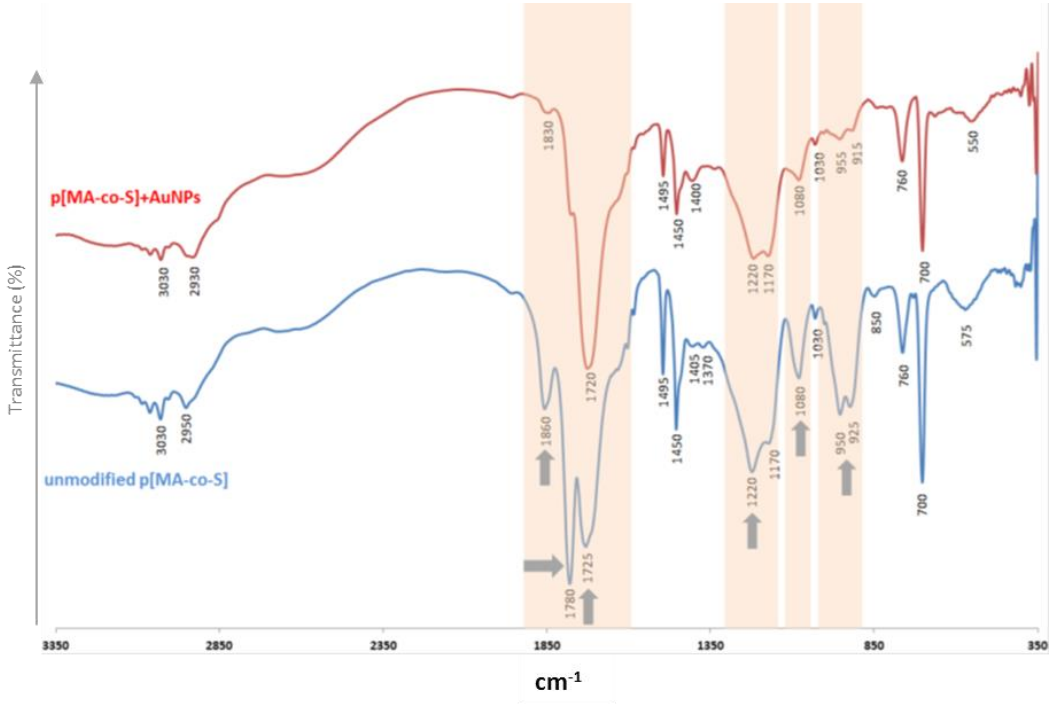

Fig. 58. FTIR spectrum of p[MA-co-S] copolymer and p[MA-co-S]-AuNPs nanocomposite.

Comparison of FTIR spectra of p[MA-co-S] and p[MA-co-S] functionalized with Au@C8 (p[MA-co-S]+AuNPs nanocomposite) shows several evident differences between the two spectra. After the modification of the copolymeric matrix with gold nanoparticles functionalized with C8 ligand the intensity of the following signals significantly decreases: 1855 cm^{-1} (a very strong anhydride C=O antisymmetric stretch), 1780 cm^{-1} (a very strong anhydride C=O symmetric stretch), 1220 cm^{-1} (a strong cyclic anhydride or carboxylic acid signal), 1085 cm^{-1} (a strong anhydride signal), 950 and 920 cm^{-1} (medium carboxylic acids signals). The formation of amide or imide bonds is supported by the growth of signals at around 1725 cm^{-1} is visible as an increase of intensity at this frequency. The strong band at 1725 cm^{-1} may be a sum of two overlaying bands: a band of the aliphatic secondary amides,

which is usually visible at 1650-1630 cm^{-1}, and an imide band which adsorbs at higher frequencies, up to 1740 cm^{-1}. A new signal is also seen at 1400 cm^{-1}. This signal however does not indicate the formation of a new bond. It is derived from the small fraction of anhydride groups that transform into carboxylic acid salts.

3.8.2.2. NMR

PVA-based nanocomposite

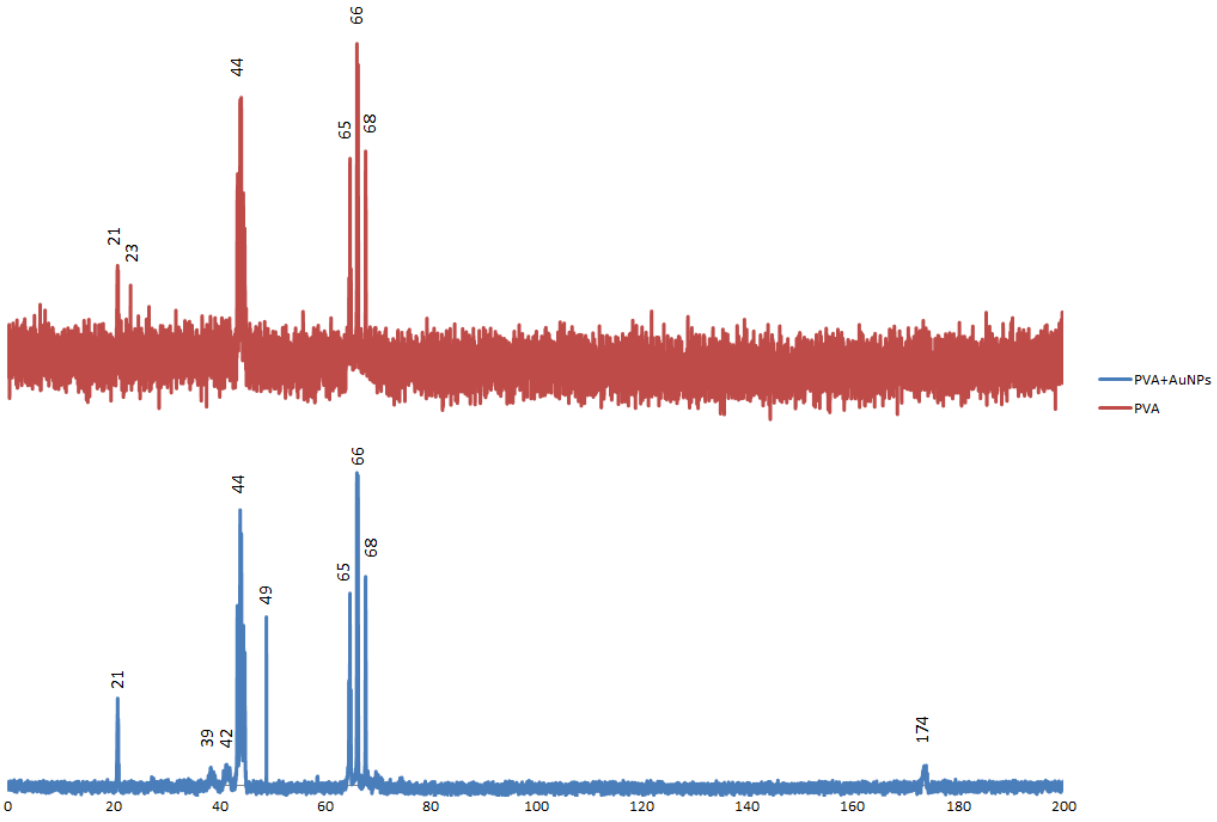

Fig. 59. NMR spectra of PVA and PVA-AuNPs mposite.

Presence of amide covalent bonds was evidenced via ^{13}C NMR experiments. A signal at 174 ppm, in the PVA-AuNPs nanocomposite spectra indicated the presence of such chemical bonds.

P[MA-co-S]-based nanocomposite

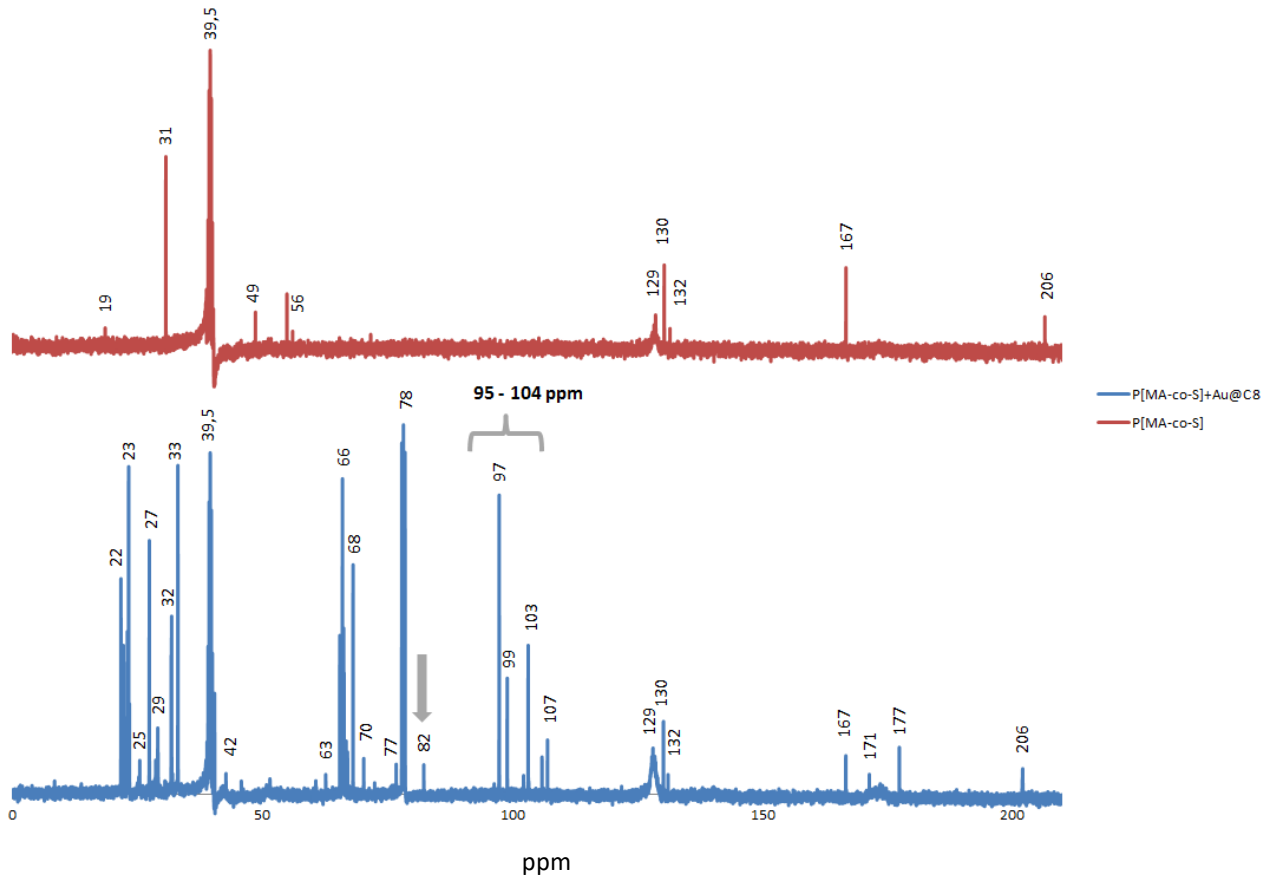

Fig. 60. NMR spectra of P[MA-co-S] and P[MA-co-S]-AuNPs nanocomposite.

It was found that in the NMR spectrum new signals emerged after the modification of the polymer matrix. The new peaks appeared at 81 ppm (indicated by a grey arrow on Fig. 60) and in the range from 95 to 104 ppm. The signal located at 81 ppm is characteristic for the aminal bonds, whereas the signals in the higher region are due to the formation of the hemiaminals. The presence of numerous signals in the region 95–104 ppm results from a number of possible neighboring groups in the polymer chain in the vicinity of the created hemiaminal bonds. This may be also a consequence of the polydispersity of the polymer chain length that gives rise to the multiplicity of the peaks.

3.8.2.3. SEM studies

SEM images of the starch–Au@C8 grain obtained at room temperature shown in Fig. 61 reveal uniform distribution of the NPs on the surface of the nanocomposite. Signs of aggregation of nanoparticles into larger agglomerates are not visible.

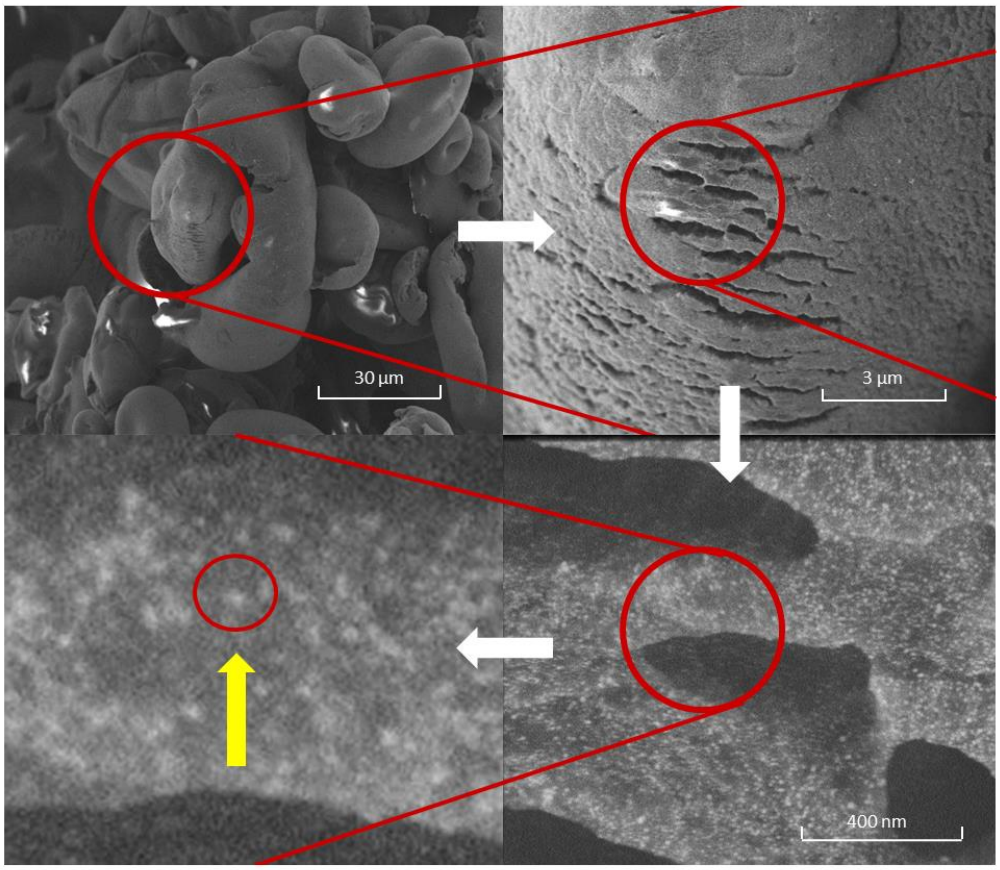

Fig. 61. SEM images of the starch–Au@C8 powder nanocomposite. The yellow arrow indicates single AuNP bound to the matrix.

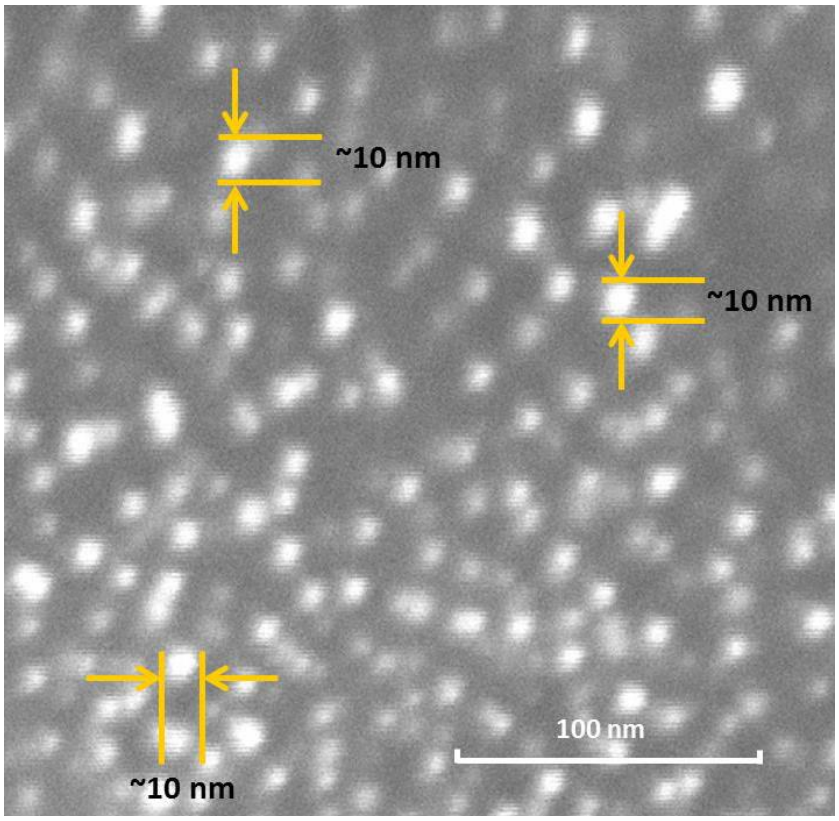

Fig. 62. SEM image of the surface of starch-Au@C8 powder nanocomposite demonstrating homogeneous distribution of the NPs. Approximate sizes of selected NPs are marked.

3.8.2.4. Determination of stability of NP against leaching for the obtained starch-based nanocomposites

To check the NP light absorption level UV-vis spectroscopic measurements of supernatant samples, acquired from suspensions of starch, were done. To perform these measurements, 45 mg of the starch– Au@C8 powder nanocomposite was added into 5 mL of distilled water. After 1 h UV-vis spectrum of the supernatant was recorded. The nanocomposite was then subjected to 1 h of ultrasonic exposure and 24 h of subsequent soaking, and the UV-vis spectrum was taken. Both the obtained spectra were found to be identical and displayed no peaks characteristic for the NPs.

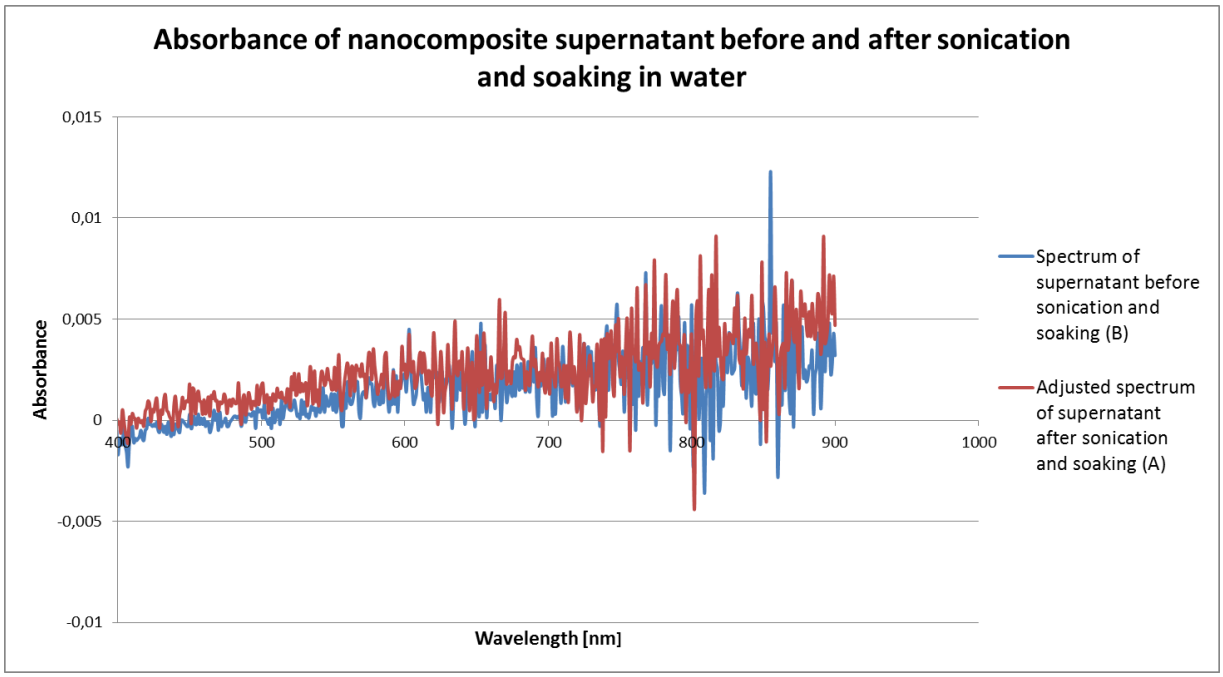

Fig. 63. UV-vis absorbance spectrum of the supernatant before (B) sonication and soaking of the nanocomposite, as well as of the supernatant after the sonication (A) and soaking of the nanocomposite.

The difference between the spectra obtained after (A) and before (B) sonication was analyzed. To the values of the resulting difference a linear function $ax + b$ was fitted, where x is the wavelength measured in nm. The coefficient a was, within statistical uncertainty, equal zero $a = (-1.15 \pm 3.22) \times 10^{-7}$ nm^{-1}, whereas the coefficient b had a nonzero value. This proves that the two analyzed spectra differed only by a constant value that was due to the difference in a background level. The constant value b, obtained as a result of the fitting, was subtracted from the spectrum A. The difference between the spectrum B and the adjusted spectrum A is shown in Fig. 64. This result proved that the release of the NPs actually did not take place.

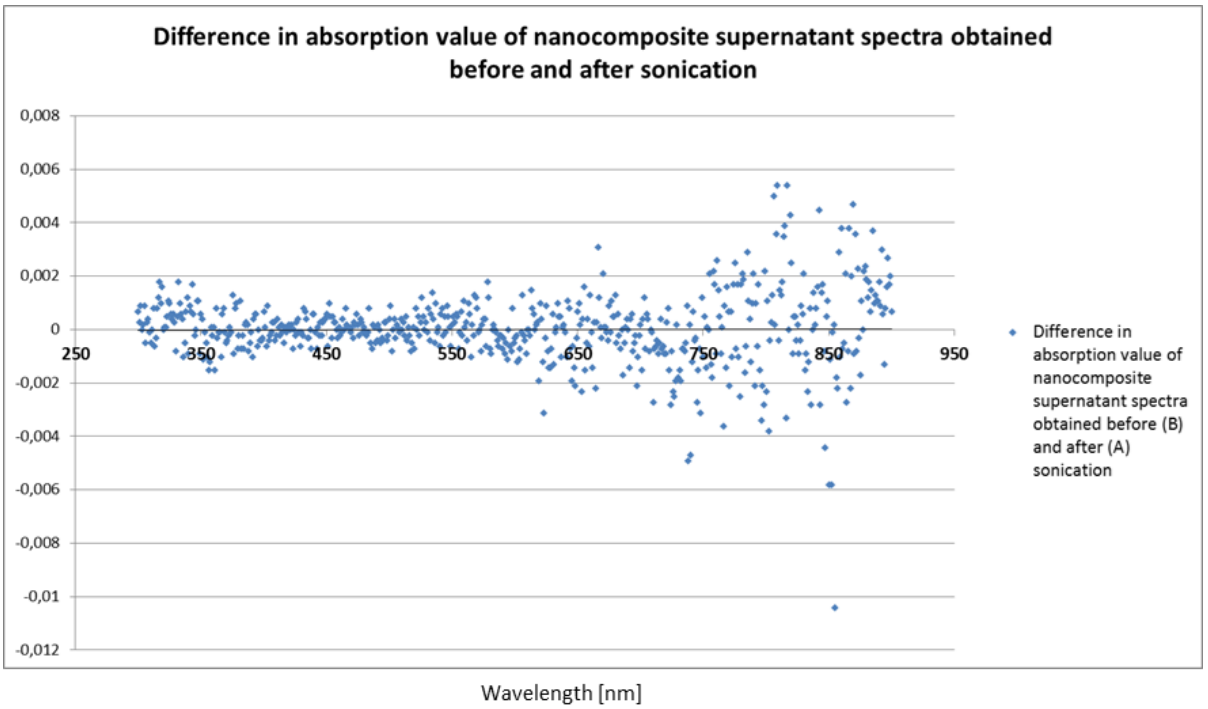

Fig. 64. Illustration of the value of difference in absorption between spectra of a nanocomposite supernatant obtained before and after sonication. The spectrum (A) was adjusted by subtraction of constant (background) value *b*.

3.9. Characterization of the synthesized 3D nanocomposites

3.9.1. Starch-based nanocomposites

I have incorporated three types of the NPs into the polymer matrix – the AuNPs, PtNPs, and AgNPs, all coated with the same 8-merkaptooctan-1-aminium chloride ligand. The materials obtained with the use of AuNPs, PtNPs and AgNPs are shown in Fig. 65.

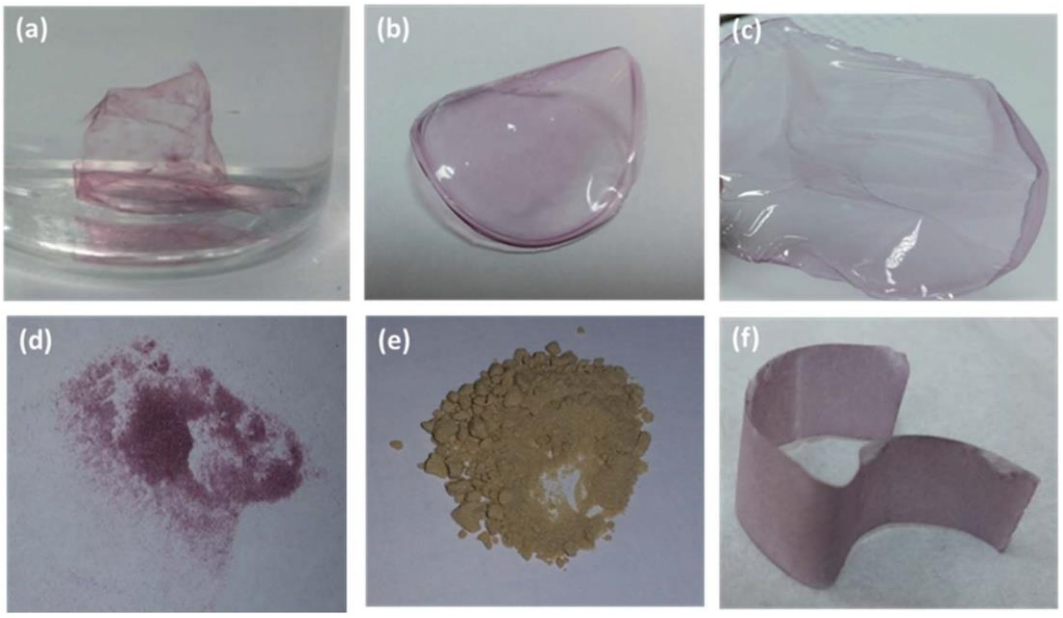

Fig. 65. (a) The starch–AuNPs nanocomposite thin film floating freely in a water-filled vial. The PVA–AuNPs (b), and CMC–AuNPs (c) nanocomposite free-standing films. The starch–AuNPs (d), and starch–AgNPs (e) powder nanocomposite. (f) Paper strip modified with the AuNPs – an example of the cellulose–AuNPs nanocomposite.

Importantly, the NPs can be embedded either on the surface or within the bulk of the matrix, depending on the employed protocol of the composite preparation. When the reaction of the bond formation between the capping ligands and the surface groups of starch is carried out at room temperature, the NPs are embedded only on the outer portions of the polymer matrix. This is caused by the low solubility of starch in aqueous environments at temperatures lower than 70 °C.[289] Preheating the starch solution to 90 °C prior to the addition of the NPs results in a homogenous embedding of the NPs throughout the bulk of the polymer matrix. The starch modification process is facilitated by electrostatic attraction between the positively charged NPs and the negatively charged starch polymer chains. The positive charge is provided by the capping ligands possessing primary amine groups in the terminal position which are easily protonated. The electrostatic interaction allows the NPs to locate themselves on the polymer chain. The NPs are linked through imine bonds that are formed between the terminal aldehyde groups of the polymer and the amine groups of the capping ligand. Since the aldehyde moieties are present only in the terminal positions of the polymer backbone, the number of the imine bonds formed is expected to be miniscule compared to the total number of the monosaccharide units. The aldehyde group is liberated in the tautomeric transformation

between the cyclic and linear form of the terminal glucose unit (Scheme 4b). However, the total number of the aldehyde groups can be substantially increased during the modification process either by acidification or oxidation (Scheme 4a). In acidic conditions hydrolysis of the 1,4- or 1,6-glycoside bonds occurs, releasing one aldehyde group per each hydrolyzed bond. In the case of oxidation, cleavage of the C–C bonds between the second and third carbon atoms of the glucose ring takes place. Both the hydroxyl groups created are then oxidized yielding two aldehyde groups per each C–C broken bond.[290] In the case discussed, acidic hydrolysis is more likely to occur, since the solution of aminothioalkyl-functionalized AuNPs is highly acidic. However, the oxidation process can also take place due to oxygen present in the solution. The increase of the number of the aldehyde groups allows incorporation of a greater amount of the NPs, which is beneficial for the nanocomposite preparation process. Importantly, the NPs create interconnections between the polymer chains that can compensate for the linkages lost due to the hydrolysis process. Thanks to these connections the composite material is gaining the mechanical durability.

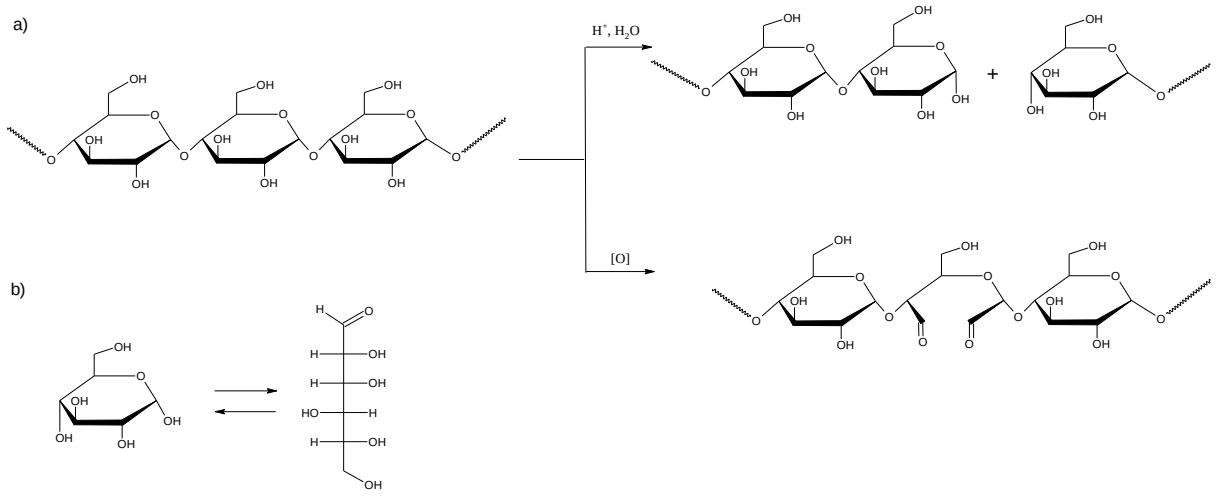

Scheme 4. Pathways of the oxidative conversion of hydroxyl into carbonyl groups, facilitating formation of covalent bonds with the amine moiety, shown for polysaccharide (a). (b) Structure of two tautomeric forms (cyclic and linear) of glucose monomer.

The formation of the C-N imine bonds was confirmed by FTIR spectroscopy performed for the starch–Au@C8 nanocomposites. The evidence of the creation of the covalent bonds follows from the comparison of the spectra of the unmodified potato starch and the same polymer modified by the incorporation of Au@C8. The presence of a new peak located at around 1680 cm^{-1}, as well as the substantial increase of the intensity of the peak at 1665 cm^{-1},

as seen on Fig. 55, evidences the formation of imine bonds.[286] To demonstrate the durability of the chemical bonds formed between the capping ligands and the polymer matrix in the presence of the NPs, I performed experiments showing that leaching of the NPs form the composite into an aqueous environment does not occur during soaking of the nanocomposite. The NPs were not detached from the surface of the polymer even after ultrasonic exposure of the nanocomposite in aqueous solutions. On the other hand non-functionalized NPs or NPs functionalized with nonreactive organic ligands, such as carbohydrate chains, do not bind to solid matrices at all or form weak bonds. Binding through the non-chemical bonds (hydrogen bonding, electrostatic interactions, or dispersive forces) results in a nanocomposites from which the NPs quite easily leach into the environment. During the experiments I observed that the Martin's AuNPs in neutral pH (in basic and acidic conditions they become unstable and aggregate rapidly) hardly adsorbed on potato starch, and the obtained powder nanocomposite had light red color. Moreover, this nanocomposite slightly stained water a reddish color each time it was immersed in it.

3.9.2. PVA-based nanocomposites

PVA is a widely used synthetic polymer that does not contain carbonyl groups. We employed it successfully to obtain a free standing nanocomposite film. The modification method comprised mixing of aqueous solution of the polymer with a solution of the Au@C8 at elevated temperature followed by evaporation of water. The resulting free-standing nanocomposite film is shown in Fig. 65b. The modification of PVA is feasible because, as it has been reported,[288] in oxidizing conditions this polymer undergoes degradation resulting in a scission of the main chain. This decomposition process involves formation of polyketones that can be further converted into aldehydes, and carboxylic acid terminated polymers (Scheme 5). This process is accelerated significantly at high temperatures, which is the reason why the functionalization should be carried out at elevated temperatures (70 °C). A peak at around 1760 cm^{-1} in the FTIR spectrum corresponding to the aldehyde group was observed in the PVA polymer before any processing (see Fig. 56), indicating that the oxidation process occurs in the solid state at air conditions. The formation of the aldehyde and carboxyl acidic groups allows for the linking of the polymer with the aminothioalkyl ligands through amide bonds. The presence of these bonds in the PVA–Au@C8 nanocomposite was evidenced by ^{13}C NMR and FTIR spectroscopy. The FTIR spectra of unmodified PVA and PVA–Au@C8

that are shown in Fig. 56 exhibit substantial differences. The comparison of these two FTIR spectra provides a clear evidence for the formation of peptide and imide bonds between PVA functional groups and the ligand amine groups. Analysis of FTIR spectra of PVA-based nanocomposites reveal signals characteristic for imides and secondary amides, indicating the formation of covalent bonds between the polymeric backbone and amine groups of reactive NPs. The presence of amide bonds was further confirmed by NMR, as a signal at 174 ppm was visible on the spectra (see Fig. 59). Sintering of the nanocomposites at 80 °C leads to the disappearance of carboxylate aminium salt signals. This salt is formed as an intermediate product of the amide formation (see Fig. 67). It follows that some of the amine groups are initially trapped in the form of carboxylate aminium salts, though they may be transformed into amides after thermal energy is delivered to the system. That is, complete transformation of amines into amide groups is possible in the presence of the NPs, but requires heat treatment.

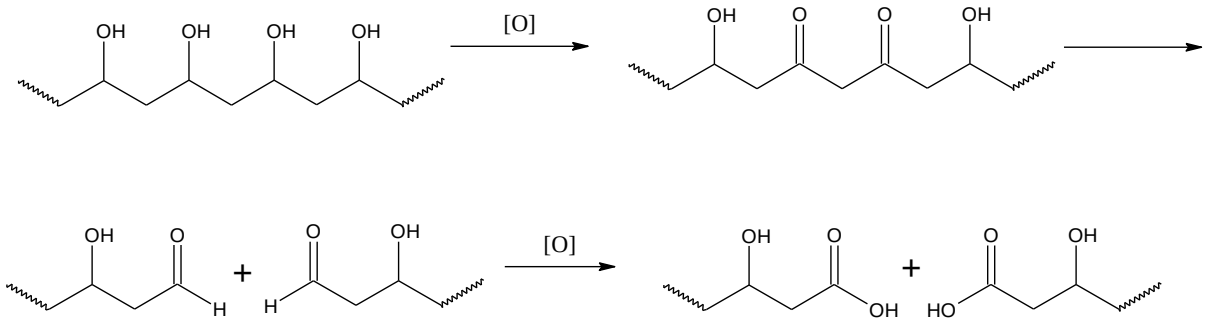

Scheme 5. Pathways of the oxidative conversion of hydroxyl into carbonyl groups, facilitating formation of covalent bonds with the amine moiety, shown for PVA.

3.9.3. Carboxymethylcellulose (CMC) – based nanocomposites

CMC is an anionic water-soluble polymer derived from cellulose that is commonly used in the industry. We applied CMC for the preparation of a free-standing nanocomposite film. Using a method similar to that applied to obtain the PVA-based nanocomposite film, I incorporated the Au@C8 into the bulk of the polymer matrix. The synthesis was easy to perform because the capping ligands readily bound to the carboxylic groups of the CMC chain forming imine bonds. The resulting nanocomposite material had a form of a robust semi-transparent free-standing film (~0.5 mm thick), which is presented in Fig. 65c. The

thickness of the film can be easily controlled by the amount of CMC applied onto the Petri dish.

3.9.4. Poly[maleic anhydride-co-styrene] (P[MA-co-S]) – based nanocomposites

Experiments were also performed using a synthetic copolymer of maleic anhydride and styrene, P[MA-co-S], as the matrix. The modification process was done by immersing granules of this polymer in aqueous solution of Au@C8. This procedure is illustrated in Fig. 66. The presence of carboxylic acid groups in the matrix before functionalization with nanoparticles, evidenced by FTIR experiments, is not surprising since the anhydride groups can be easily transformed into carboxylic acid in acid or basic conditions. The aminothiol molecules readily bound to the polymer due to the presence of acidic anhydride functional groups in the chain (see Scheme 6).

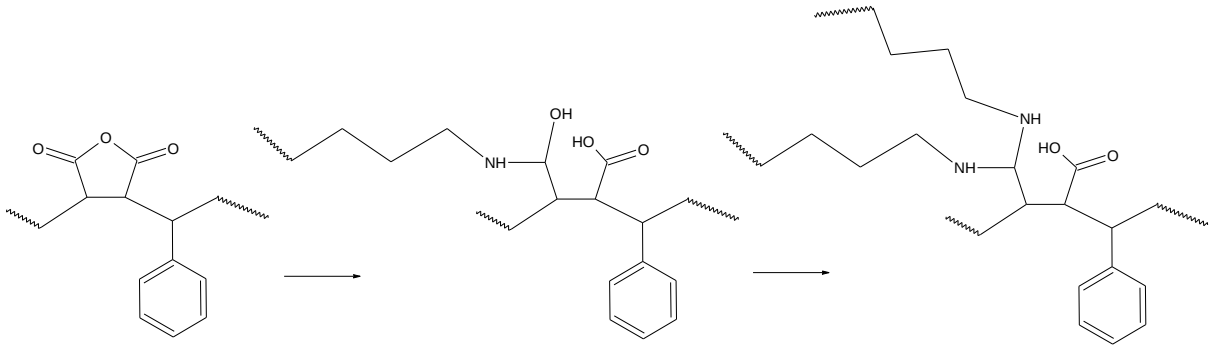

Scheme 6. Formation of the aminal and hemiaminal bonds between the P[MA-co-S] co-polymer and amine groups.

The binding occurs through the formation of aminal and hemiaminal bonds, and was confirmed by ^{13}C NMR studies. It was found that in the NMR spectrum new signals emerged after the modification of the polymer matrix (see Fig. 60). The new peaks appeared at 81 ppm and in the range from 95 to 104 ppm. The signal located at 81 ppm is characteristic for the aminal bonds, whereas the signals in the higher region are due to the formation of the hemiaminals. The presence of numerous signals in the region 95–104 ppm results from a number of possible neighboring groups in the polymer chain in the vicinity of the created hemiaminal bonds. This may be also a consequence of the polydispersity of the polymer chain length that gives rise to the multiplicity of the peaks. To further characterize the material, FTIR spectra were also recorded for unmodified P[MA-co-S] and the P[MA-co-S]-Au@C8

nanocomposite (see Fig. 58).The disappearance of the signals corresponding to carboxylic acid groups occurring due to the formation of bonds between the surface ligands of Au@C8 and the functional groups of the matrix, is observed. In this case amide or imide bonds formation is the most probable explanation.

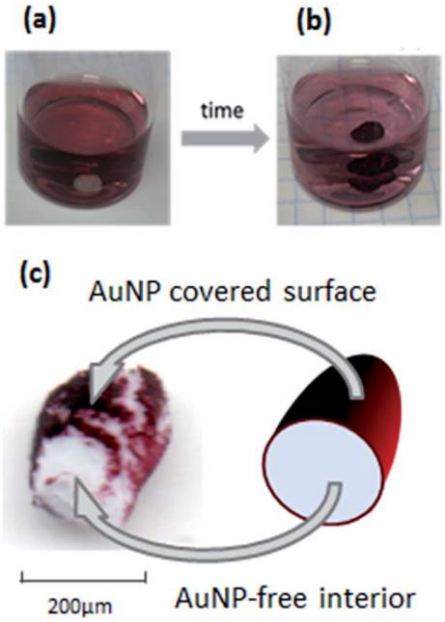

Fig. 66. Photograph of a grain of P[MA-co-S] polymer taken 10 min (a) and 24 h (b) after immersion in aqueous solution of Au@C8. (c) A picture of the cross section of the grain of P[MA-co-S] copolymer functionalized with Au@C8 at 25 ˚C. As seen, the NPs are embedded only on the outer portions of the grain.

3.9.5. Cellulose–based nanocomposites

Cellulose is another example of a natural polysaccharide material that can covalently bind to the aminothioalkyl functionalized NPs. The binding mechanism is in this case essentially the same as for starch. The modification procedure was simple, as it consisted only of immersing of a piece of cellulose paper in an aqueous solution of the Au@C8. The adsorption process was completed within minutes, and manifested by a change of the color of the sample from white to pink. The modified paper sample is shown in Fig. 65f.

3.9.6. The role of NPs in the process of bond formation

The formation of amide bonds from carboxylic acids and amines at ambient conditions is energetically unfavorable (endoergic) [291] and usually possesses a high energy barrier.[292] The peptide bond formation is a two-stage process. An acid– base reaction occurs first, yielding a stable salt according to the equation (see also Fig. 67a):[293]

$$R–COOH + R'–NH_2 \rightleftharpoons R–COO^- H_3N^+–R' \rightleftharpoons R–CO–NH–R'$$

It follows that the equilibrium of the bond formation reaction is strongly shifted in the hydrolysis direction,[294] and does not occur in the opposite direction spontaneously at ambient conditions.[295] To increase the amide synthesis reaction yield, activating agents or catalysts must be employed, since direct condensation of the formed salt takes place only at elevated temperatures (160–180 °C).[296] There are several methods of imide bond creation described in the literature, but there, like in the case of amides, such reactions take place between amines and activated carboxyl derivatives such as carboxylic anhydrides or carboxyl acid chlorides.[281] Inactivated carboxyl acids do not yield imides in reactions with amines. Acylation of amines by carboxylic esters may also occur, but the reactivity of simple esters (methyl, ethyl) in this conversion is minor, making catalyst or high pressure utilization necessary.[297] Imides may also be formed in a reaction between an amide group and an adjacent ammonium carboxylic salt or carboxyl acid group. However, these reactions require high temperatures of several hundred degrees.[298] The above examples clearly show that when an imide is formed at ambient conditions a reaction enhancer is necessary. We have however observed that both amide and imide bonds were created at room temperature when the amine-terminated ligand was attached to the NP surface. This follows that in such conditions the reactivity of the amine terminal group towards peptide and imide bond formation is substantially enhanced. The reaction Gibbs free energy, ΔG, is a quantity that determines the reaction direction, having a negative value for favored reactions and positive for disfavored ones. Because the enthalpy of the amide or imide formation is negative at ambient temperatures,[299, 300] the drop of the reaction entropy, ΔS, is responsible for the positive value of ΔG of the amide or imide formation. This is expected since the binding of the free amines to the polymer backbone considerably reduces their motion liberty (both

transitional and rotational), significantly decreasing their entropy, and making the contribution TΔS negative. When the ligands are attached to the NPs the loss of entropy is significantly reduced because the ligands are pre-immobilized prior to the bond formation reaction. Most likely, in the NP-mediated bond formation the entropy contribution is substantially diminished. This makes ΔG negative, allowing the reaction to proceed spontaneously. The NPs play thus a role of the reaction enhancing agent, since it is the immobilization of the ligands on its surface that makes the reaction exoergic at ambient conditions. This role of the NPs is explained schematically in Fig. 67.

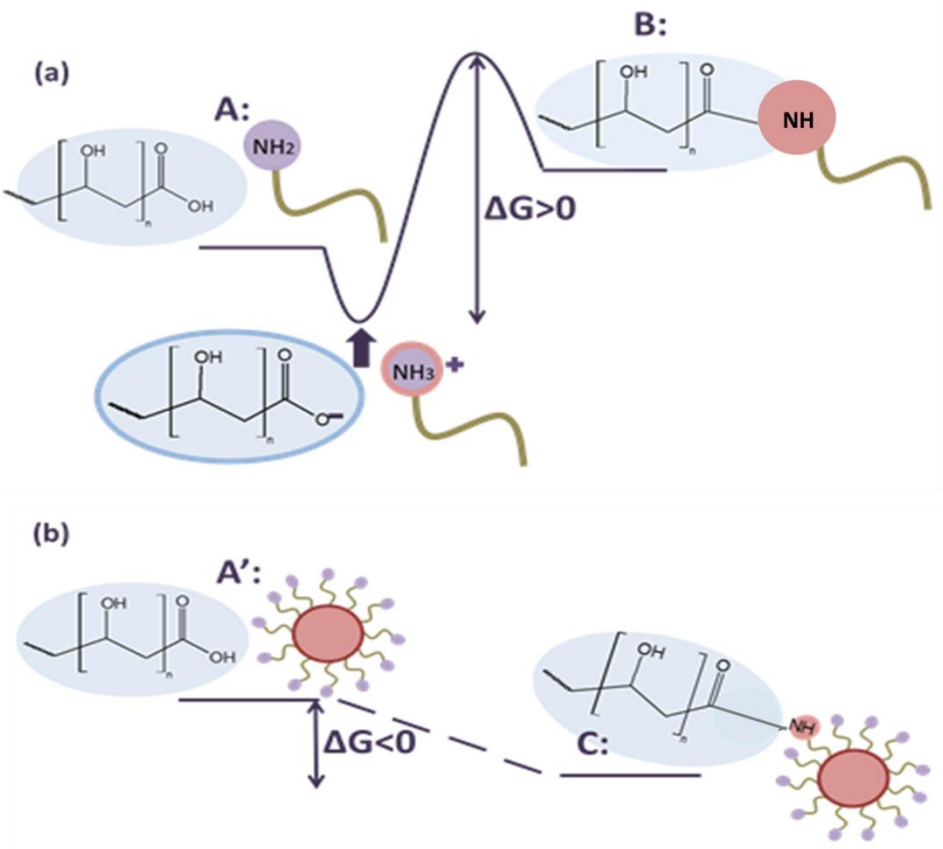

Fig. 67. The energetic states of substrates, intermediate products and final products of peptide bond formation reaction in the absence (a) and in the presence of the NPs (b).

The fact that the covalent amide bonds are not formed in a reaction between free aminothioalkyl molecules and PVA matrix, but are evident when the reacting ligands are attached to the surface of NPs is remarkable. It proves that the presence of the NPs is necessary for this amide or imide bond formation reaction to occur. The conditions of the

bond formation reactions of PVA polymer with free ligand (the concentration of the ligand, pH, the reaction time etc.) were exactly the same as in the case of the bond formation reactions involving the NPs. This allowed for the elimination of the possibility of any other factors influencing the reactions investigated. FTIR spectra of the products of the reactions of PVA with free ligands (PVA-C8) were recorded and compared with the corresponding FTIR spectra of PVA–Au@C8 nanocomposites. The FTIR spectrum of the mixture of PVA-C8 is shown in Fig. 56. Compared to the spectrum of the unmodified PVA polymer, the FTIR spectrum of PVA-C8 exhibits growth of the intensity of the right branch of the doublet signal at about 1710 cm^{-1}, which is characteristic for protonated imines.[286] The presence of imines is not surprising as they are formed spontaneously in ambient conditions. The FTIR spectrum of PVA-C8 displays also the presence of carboxylate aminium salt, evidenced by the signal at 765 cm^{-1} corresponding to the rocking of $–NH_3^+$ group. This salt is formed instead of amide bonds, which are not present in the PVA-C8 (see also Fig. 67a). Another evidence of the important role of the NPs in the binding reaction was provided by the synthesis of the P[MA-co-S]–Au@C8 composite. The reaction between an amine and acid anhydride functional group occurs usually in basic conditions (in the presence of triethyl amine).[301] In the method employed in this work such bonds are formed in acidic conditions, which indicates that an equilibrium between protonated and neutral ligands must exist on the surface of the NPs. Even in highly acidic conditions not all ligands are in the protonated state and at least a small percentage of the ligands remains uncharged. This is consistent with recent reports [302] showing dependence of ionization of ligands immobilized on the NP surface on the curvature of the NPs. It was shown that the immobilization of ionizable ligands may influence their acid–base equilibrium. The equilibrium in such conditions is shifted towards the uncharged state, compared to ligands in bulk solution, if the curvature of the NP is small. Because it is expected that the curvature of the NP influences the equilibrium between the protonated and ambient terminal amino groups of the surface ligands, affecting the rate of the reaction between these functional groups and the polymer, an extension the method to other NPs with similar curvature, e.g., carbon NPs, would be possible. Although the principal assumptions of the method should also apply to such NPs, the functionalization technique would have to be adjusted. The thiol group does not have high affinity towards the surface of carbon NPs, therefore a different anchoring group would have to be used.

4. Summary

The presented dissertation describes synthesis of a 2D, truly freestanding monolayer film composed of covalently cross-linked gold nanoparticles (AuNPs), as well as 3D polymer-based nanocomposites, containing metallic NPs chemically bound to the polymeric matrix. In the first part of my research I focused on designing the chemical structure and developing of a synthetic protocol for an organic ligand that would provide NPs with desired properties upon their surface functionalization. Amongst the key anticipated properties, the ability of the NPs to self-assemble at the liquid-liquid interface, leading to the formation of a stable monolayer, was fundamental. Since fabrication of robust 2D and 3D nanomaterials requires strong chemical bonding between the NPs within the nanomaterial, another indispensable feature of the NPs was the capability of covalent bond formation with reactive organic functional groups. A group of linear aminothiolalkyl ligands was designed, which possess a thiol group, with a high affinity to noble metals, in one terminal position, and a reactive amine group in the opposite terminal position. The distinctive chemical structure of the synthesized ligands provided NPs with features essential for the fabrication of a 2D and 3D nanostructures.

The development of a proper synthetic procedure for the fabrication of 2D nanomembranes posed a principal challenge. The issue of selection of a suitable platform for the synthesis of nanocomposites was resolved in the second part of my research. The biphasic oil-water system provided a platform (i.e. the liquid-liquid interface) for membrane fabrication. The chemical structure of the synthesized ligands provided NPs with features essential for the fabrication of a 2D membrane, constructed of chemically bound monolayer of NPs with the aid of the chosen reaction platform. These features include: (1) stabilization of NPs at the interface, preventing their aggregation, even during strong compression of such 2D structures. This is provided by the presence of a partial surface charge of NPs at the interface due to protonation of the terminal amine group; (2) anchoring of the NPs at the liquid-liquid interface, preventing of NP from re-entry into the bulk phase during membrane contraction. When adsorbed at the oil−water interface, NPs may not escape due to the large energy well. Additionally, such functionalized AuNPs display the amphiphilic (Janus-like) structure, wherein protonated ligands are situated in the aqueous phase of the system, and deprotonated ones are located in the oleic phase. Such positioning of the ligands firmly anchors the NPs, securing their position at the liquid-liquid interface. Therefore, the described NPs self-

assemble into a highly stable monolayer at the interface, where unhampered access of the cross-linking agent is guaranteed. These features make the 2D monolayer fabrication process feasible.

In the developed fabrication method a high degree of control of the NP bulk–to–interface migration process was essential. During the conducted research, I found that the pH level of NP solution influences their surface charge by altering the tendency of detaching of the labile terminal proton of the surface ligand's amine functional group. The possibility of easy tuning of the character of AuNPs coated with aminothiolate ligands, from a hydrophilic to a hydrophobic one without the need of any chemical change of the AuNPs surface, via the reversible protonation/deprotonation mechanism offers a means of facile control of the system. This feature was utilized in the NP monolayer formation process, as the pH level change influences the NPs' susceptibility towards migration from the bulk phase to the liquid-liquid interface. During my research the mechanism of the NPs' migration was examined in detail to gain a better understanding of this transferal process, leading to a higher controllability of the described fabrication method. It was found that to bring the AuNPs at the oil−water interface, an excitation of the system that leads to the formation of the oil-in-water emulsion is required. After the excitation, the AuNPs are transported onto the oil−water interface on the surface of the oil droplets that carry them as their "cargo".

As one of the milestones leading to successful fabrication of a 2D NP membrane a practical reaction vessel for this process had to be constructed. Designing and building of such a vessel was the next important objective in the course of my research. The membrane fabrication process was executed in a self-constructed reaction-contraction device, equipped with two mobile pistons, that allowed for precise control of the liquid-liquid interface area. This enabled the reduction of the distance between neighboring NPs at the interface. Interfacial reduction was necessary as AuNPs must be in close proximity so that the cross-linking molecules are able to form covalent bonds with neighboring AuNPs, making chemical cross-linking efficient.

Enhancement of the membrane robustness and mechanical strength required chemical cross-linking of NPs once a NP monolayer was obtained at the water-oil interface. Utilization of a suitable cross-linking agent for efficient chemical binding of NPs was crucial at this stage. As the cross-linking agent, naphthalene dianhydride derivative, which forms amide bonds with

the ligand molecules, was used. This naphthalene dianhydride derivative, substituted in four positions by alkyl chains, bonded with the surface ligands in a spontaneous cross-linking reaction, occurring at ambient conditions. The cross-linking process required neither reaction enhancing additives nor harsh reaction conditions. The use of a liquid-liquid interface as the reaction platform guaranteed unrestricted access of the cross-linking agent to the NPs' reactive groups.

Obtaining a truly free-standing monolayer NP membrane that would be stable in air conditions needed appropriate embedment of the nanocomposite on a porous substrate, that would provide support on the periphery of the film, yet leave its majority portion of the film completely free-standing. Developing of an appropriate approach for this goal was challenging. The as-synthesized free-standing film was transferred from the oil−water interface onto porous grids using a gravitational outflow of solvents from the reaction vessel. SEM experiments revealed that the obtained film comprises of uniformly distributed, densely-packed AuNPs, whereas SEM images of the cross-linked AuNP monolayer cross-section confirmed the single-layer nature of the obtained membrane. STEM images of the cross-linked AuNP monolayer deposited on a TEM grid confirmed that a truly free-standing, unsupported monolayer film stretched across openings of the grid was obtained. Moreover, STEM images revealed that the AuNPs within the free-standing film form a densely packed structure.

The next part of my research was devoted to developing of an undemanding method of formation of durable, well-defined 3D nanocomposites, wherein the aggregation of nanoadditives is inhibited and their detachment from the matrix is hindered. I created a novel approach to the chemical linking of ex-situ prepared noble metal NPs to various polymer matrices. In this method, NPs functionalized with the designed aminothiolalkyl ligands are capable of chemical linking via amide, imide, imine, or aminal bonds with a variety of polymers possessing carbonyl groups or hydroxyl groups that can be converted, upon oxidation, into carbonyl groups. This feature of the NPs follows directly from the presence of the surface aminothiolalkyl ligands. The capability of linking the NPs through different functional organic groups makes them potentially versatile with respect to the type of cross-linking agent (2D nanocomposites) and polymeric host matrix (3D nanocomposites). The foundation of an undemanding character of the developed method was realized since the

binding of the NPs to the polymeric matrix occurs spontaneously at ambient conditions, and does not require any external stimuli, such as temperature or UV irradiation. The synthetic procedure entails merely simple mixing of the chosen polymer, in the form of a solution or solid with an aqueous solution of the aminothioalkyl functionalized NPs. SEM experiments revealed that the NPs are distributed uniformly within the resulting nanocomposite. Aggregation of the NPs in the obtained 3D nanocomposites does not occur due to durable covalent bonding between the NPs and the polymer matrix. UV-Vis experiments confirmed that the NPs do not leach from the fabricated 3D nanocomposites when immersed in aqueous solutions.

Finally, since better understanding of the covalent bond formation mechanism assures elevation of the possibility of controlled manipulation of the fabrication process, considerable effort of my research was put to proposing a plausible bond formation mechanism. Spontaneous formation of durable chemical bonds between aminothioalkyl functionalized NPs and polymeric chains is possible due to the decrease of the entropy contribution to the reaction's Gibbs' enthalpy, following the initial anchoring of the ligand on the surface of the NPs. Binding of the amine molecules to the surface of NPs prior to the bond formation reaction reduces significantly translational, rotational, and vibrational degrees of freedom of these molecules, and hence leads to the drop of the entropy, ΔS, of the amide and imide formation reaction. In the NP-mediated bond formation reaction the entropy contribution is substantially diminished, leading to a positive value of the ΔG of the amide and imide formation. This allows the reaction to take place spontaneously at ambient conditions.

9. Literature

[1] https://ocg.cancer.gov/news-publications/e-newsletter-issue/issue-11

[2] *"Handbook of Metal Physics – Metallic Nanoparticles"*, series editor: Misra, P.; editor: Blackman, J.; **2009**, Elsevier

[3] Daniel, M.-C.; Astruc, D.; *Chem. Rev.* **2004**, *104*, 293-346.

[4] Roduner, E.; *Chem. Soc. Rev.*, **2006**, *35*, 583–592.

[5] Lead, J. R.; Wilkinson, K. J.; *Environ. Chem.*, **2006**, *3*, 159-171.

[6] Hough, R. M.; Noble, R. R. P.; Reich, M.; *Ore Geol. Rev.*, **2011**, *42*, 55-61.

[7] *"Glass and Glassware",* Savage, G.; **1975**, Octopus Book: London

[8] Faraday, M.; *Philosophical Transactions*, **1857**, *147*, 145-181.

[9] P´erez-Juste, J.; Pastoriza-Santos, I.; Liz-Marz´an, L. M.; Mulvaney, P.; *Coordination Chemistry Reviews*, **2005**, *249*, 1870–1901.

[10] Langille, M. R.; *J. Am. Chem. Soc.* **2012**, *134*, 14542−14554.

[11] *"Handbook of Less-Common Nanostructures*", Kharisov, B. I.; Kharissova, O. V.; Ortiz-Mendez, U.; **2012**, CRC Press

[12] Nikoobakht, B.; El-Sayed, M. A.; *Chem. Mater.* **2003**, *15*, 1957-1962.

[13] Law, M.; Goldberger, J.; Yang, P.; *Annu. Rev. Mater. Res.*, **2004**, *34*, 83–122.

[14] Wang, Z. L.; Gao, R. P.; Pan, Z. W.; Dai, Z. R.; *Adv. Eng. Mater.*, **2001**, *3*, No. 9, 657 – 661.

[15] Pan, Z. W.; Dai, Z. R.; Wang, Z. L.; *Science* **2001**, *291*, 1947-1949.

[16] Iijima, S.; *Nature*, **1991**, *354*, 56-58.

[17] De Volder, M. F. L.; Tawfick, S. H.; Baughman, R. H.; John Hart, A.; *Science*, **2013**, *339*, 535 – 539.

[18] Mahmoud, M. A.; Saira, F.; El-Sayed, M. A.; *Nano Letters*, **2010**, *10* (9), 3764-3769.

[19] Barbosa, S.; Agrawal, A.; Rodriguez-Lorenzo, L.; Pastoriza-Santos, I.; Alvarez-Puebla, R. A.; Kornowski, A.; Weller, H.; Liz-Marzan, L. M.; *Langmuir*, **2010**, *26*, 14943−14950.

[20] Nehl, C. L.; Liao, H. W.; Hafner, J. H.; *Nano Lett.*, **2006**, *6*, 683−688.

[21] Vo-Dinh, T.; Liu, Y.; Fales, A. M.; Ngo, H.; Wang, H.-N.; Register, J. K.; Yuan, H.; Norton, S. J.; Griffin, G. D.; *Wiley Interdisciplinary Reviews: Nanomedicine and Nanobiotechnology*, **2015**, *7*, 17−33.

[22] Minati, L.; Benetti, F.; Chiappini, A.; Speranza, G.; *Colloids Surf., A*, **2014**, *441*, 623−628.

[23] Dam, D. H. M.; Lee, J. H.; Sisco, P. N.; Co, D. T.; Zhang, M.; Wasielewski, M. R.; Odom, T. W.; *ACS Nano*, **2012**, *6*, 3318−3326.

[24] Dondapati, S. K.; Sau, T. K.; Hrelescu, C.; Klar, T. A.; Stefani, F. D.; Feldmann, J.; *ACS Nano*, **2010**, *4*, 6318−6322.

[25] Su, Q.; Ma, X.; Dong, J.; Jiang, C.; Qian, W.; *ACS Appl. Mater. Interfaces*, **2011**, *3*, 1873−1879.

[26] Pallavicini, P.; Chirico, G.; Collini, M.; Dacarro, G.; Dona, A.; D'Alfonso, L.; Falqui, A.; Diaz-Fernandez, Y.; Freddi, S.; Garofalo, B.; *Chem. Commun.*, **2011**, *47*, 1315−1317.

[27] Burt, J. L.; Elechiguerra, J. L.; Reyes-Gasga, J.; Montejano-Carrizales, J. M.; Jose-Yacaman, M.; *J. Cryst. Growth*, **2005**, *285*, 681-691.

[28] Cabrera-Trujillo, J.; Montejano-Carrizales, J.; Rodríguez-Lopez, J.;´ Zhang, W.; Velazquez-Salazar, J.; Jose´ -Yacama´ n, M.´; *J. Phys. Chem. C*, **2010**, *114*, 21051-21060.

[29] Jiang, L.; Tang, Y.; Liow, C.; Wu, J.; Sun, Y.; Jiang, Y.; Dong, Z.; Li, S.; Dravid, V. P.; Chen, X.; *Small*, **2013**, *9*, 705-710.

[30] Jing, H.; Zhang, L.; Wang, H.; *Springer Berlin Heidelberg*, **2013**, 1-74.

[31] Niu, W.; An Alvin Chua, Y.; Zhang, W.; Huang, H.; Lu, X.; *J. Am. Chem. Soc.*, **2015**, *137*, 10460−10463.

[32] Ng, K. K.; Zheng, G.; *Chem. Rev.*, **2015**, *115*, 11012−11042.

[33] Christian, P.; Von der Kammer, F.; Baalousha, M.; Hofmann, Th.; *Ecotoxicology*, **2008**, *17*, 326–343.

[34] *"Inorganic Nanoparticles: Synthesis, Applications, and Perspectives"*, Altavilla, C.; Ciliberto, E.; **2016**, CRC Press

[35] Regulacio, M. D.; Han, M.-Y.; *Accounts of Chemical Research*, **2010**, *43*, No. 5, 621-630.

[36] Ray, S. C.; Saha, A.; Jana, N. R.; Sarkar, R.; *J. Phys. Chem. C*, **2009**, *113*, 18546–18551.

[37] "Methods and strategies for the synthesis of diverse nanoparticles and their applications: a comprehensive overview", C. Dhand, C.; Dwivedi, N.; Loh, X. J.; Jie Ying, A. N.; Verma, N. K.; Beuerman, R. W.; Lakshminarayanan, R.; Ramakrishna, S.; *RSC Adv.*, **2015**, *5*, 105003–105037.

[38] de Carvalho, J. F.; de Medeiros, S. N.; Morales, M. A.; Dantas, A. L.; Carrico, A. S.; *Appl. Surf. Sci.*, **2013**, *275*, 84–87.

[39] Ward, M. B.; Brydson, R.; Cochrane, R. F.; *J. Phys.: Conf. Ser.*, **2006**, *26*, 296–299.

[40] *"Synthesis and Patterning Methods for Nanostructures Useful for Biological Applications, in Nanotechnology for Biology and Medicine"*, ed.: Daraio, C.; Jin, S.; Silva, G. A.; Parpura, V.; **2012**, Springer, New York , pp. 27–44.

[41] R. D. Amato, R. D.; Falconieri, M.; Gagliardi, S.; Popovici, E.; Serra, E.; Terranova, G.; Borsella, E.; *J. Anal. Appl. Pyrolysis*, **2013**, *104*, 461–469.

[42] Heiligtag, F. J.; Niederberger, M.; *Materials Today*, **2013**, *16*, No. 7/8, 262-271.

[43] Cushing, B. L.; Kolesnichenko, V. L.; O'Connor, C. J.; *Chem. Rev.* **2004**, *104*, 3893−3946.

[44] *„Nanoparticles Preparation Using Microemulsion Systems, Microemulsions – An Introduction to Properties and Applications. 12."*, Zielińska-Jurek, A.; Reszczyńska, J.; Grabowska, E.; Zaleska, A.; Najjar, R. (Ed.) , **2012**, InTech

[45] H. Hayashi, Y. Hakuta, *Materials*, **2010**, *3*, 3794 – 3817.

[46] Kim, M.; Son, W.-S.; Ahn, K. H.; Kim, D. S.; Lee, H.-S.; Lee, Y.-W.; *J. of Supercritical Fluids*, **2014**, *90*, 53–59.

[47] M. Outokesh, M.; Hosseinpour, M.; Ahmadi, S. J.; Mousavand, T.; Sadjadi, S.; Soltanian, W.; *Ind. Eng. Chem. Res*., **2011**, *50*, 3540–3554.

[48] Hayashi, H.; Torri, K.; *J. Mater. Chem*, **2002**, *12*, 3671-3676.

[49] Dong, H.; Chen, Y.-C.; Feldmann, C.; *Green Chem.*, **2015**, *17*, 4107-4132.

[50] Swihart, M. T.; *Current Opinion in Colloid and Interface Science*, **2003**, *8*, 27–133.

[51] Senter, R. A.; Chen, Y.; Coffer, J. L.; Tessler, L. R.; *Nano Lett.*, **2001**, *1*, 383 –386.

[52] Sathish, K. K.; Amutha, R.; Arumugam, P.; Berchmans, S.; *ACS Appl. Mater. Interfaces*, **2011**, *3*, 1418–1425.

[53] Pimprikar, P. S.; Joshi, S. S.; Kumar, A. R.; Zinjarde, S. S.; Kulkarni, S. K.; *Colloids Surf., B*, **2009**, *74*, 309–316.

[54] Kundu, S.; Nithiyanantham, U.; *Ind. Eng. Chem. Res.*, **2014**, *53*, 13667–13679.

[55] Cabrera, F. C.; Mohan, H.; Santos, R. J. D.; Agostini, D. L. S.; Aroca, R. F.; M. A. Rodr´ıguez-P´erez, M. A.; Job, A. E.; *J. Nanomater.*, **2013**, *2013*, Article ID 710902, 10 pages.

[56] Pokorski, J. K.; Steinmetz, N. F.; *Mol. Pharm.*, **2011**, *8*, 29–43.

[57] Iravani, S.; *Green Chem.*, **2011**, *13*, 2638–2650.

[58] Turkevitch, J.; Stevenson, P. C.; Hillier, J.; *Discuss. Faraday Soc,*. **1951**, *11*, 55-75.

[59] Frens, G.; *Nature: Phys. Sci.*, **1973**, *241*, 20-22.

[60] Brust, M.; Walker, M.; Bethell, D.; Schiffrin, D. J.; Whyman, R. J.; *J. Chem. Soc., Chem. Commun.* **1994**, 801-802.

[61] Brust, M.; Fink, J.; Bethell, D.; Schiffrin, D. J.; Kiely, C. J.; *J. Chem. Soc., Chem. Commun.*, **1995**, 1655-1656.

[62] Martin, M. N.; Basham, J. I.; Chando, P.; Eah, S.-K.;

[63] Sperling, R. A.; Parak, W. J.; *Phil. Trans. R. Soc. A*, **2010**, *368*, 1333–1383.

[64] H. Schmidt, *Appl. Organometal. Chem*, **2001**, *15*, 331-343.

[65] Toma, H. E.; Zamarion, V. M.; Toma, S. H.; Araki, K.; *J. Braz. Chem. Soc.*, **2010**, *21*, No. 7, 1158-1176.

[66] Li, H.; Zhao, M.; Jiang, Q.; *J. Phys. Chem. C*, **2009**, *113*, 7594-7597.

[67] Yacamán, M. J.; Acencio, J. A.; Liu, H. B.; Gardea-Torresdey, J.; *J. Vacuum Sci. Technol. B*, **2001**, *19*, 1091-1103.

[68] Li, H.; Han, P. D.; Zhang, X. B.; Li, M.; *Materials Chemistry and Physics*, **2013**, *137*, 1007-1011.

[69] Schmid, G.; Baumle, M.; Geerkens, M.; Helm, I.; Osemann, C.; Sawitowski, T.; *Chem. Soc. Rev.*, **1999**, *28*, 179-207.

[70] Montejano-Carrizales, J. M.; Aguilera-Granja, F.; Moran-Lopez, J. L.*; Nanostruct. Mater.*, **1997**, *8*, 269-287.

[71] Baletto, F.; Ferrando, R.; *Rev. Mod. Phys.*, **2005**, *77*, 371-423.

[72] Guo, D.; Xie, G.; Luo, J.; *J. Phys. D: Appl. Phys.*, **2014**, *47*, 013001-013026.

[73] Ramos, M.; Ortiz-Jordan, L.; Hurtado-Macias, A.; Flores, S.; Elizalde-Galindo, J. T.; Rocha, C.; Torres, B.; Zarei-Chaleshtori, M.; Chianelli, R. R.; *Materials*, **2013**, *6*, 198–205.

[74] Carlton, C. E.; Ferreira, P. J.; *Micron*, **2012**, *43*, 1134–1139.

[75] Wang, J. W.; Narayanan, S.; Huang, J. Y.; Zhang, Z.; Zhu, T.; Mao, S. X.; *Nature Commun.*, **2013**, *4*, 2340.

[76] Mordehai, D.; Kazakevich, M.; Srolovitz, D. J.; Rabkin, E.; *Acta Mater.*, **2011**, *59* 2309–2321.

[77] Ouyang, G.; Zhu, W. G.; Sun, C. Q.; Zhu, Z. M.; Liao, S.Z.; *Phys. Chem. Chem. Phys.*, **2012**, *12*, 1543–1549.

[78] Ducker, W. A.; Senden, T. J.; Pashley, R. M.; *Nature*, **1991**, *353*, 239–241.

[79] Guo, D.; Li, J.; Chang, L.; Luo, J.; *Langmuir*, **2013**, *29*, 6920–6925.

[80] Heim L.-O.; Blum, J.; *Phys. Rev. Lett.*, **1999**, *83*, 3328–3331.

[81] Wronski, C. R. M.; *Br. J. Appl. Phys.*, **1967**, *18*, 1731-1737.

[82] Warrier, P.; Teja, A.; *Nanoscale Research Letters*, **2011**, *6*, 247.

[83] Nath, P.; Chopra, K. L.; *Thin Solid Films*, **1974**, *20*, 53-62.

[84] Resonance Spectroscopy and Sensing

[85] Kelly, K. L.; Coronado, E.; Zhao, L. L.; Schatz, G. C.; *J. Phys. Chem. B*, **2003**, *107*, 668-677.

[86] "Mie Scattering of Electromagnetic Waves", Yushanov, S.; Crompton, J. S.; Koppenhoefer, K. C.; *Excerpt from the Proceedings of the 2013 COMSOL Conference in Boston*

[87] Garnett, J. C. M.; *Phil. Trans. R. Soc. London, Ser. A*, **1906**, *205*, 237-288.

[88] Ghosh, S. K.;Pal, T.; *Chem. Rev.*, **2007**, *107*, 4797–4862.

[89] Cuenya, B. R.; *Thin Solid Films*, **2010**, *518*, 3127–3150.

[90] Cho, A.; *Science*, **2003**, *299*, 1684-1685.

[91] Mills, G.; Gordon, M. S.; Metiu, H.; *J. Chem. Phys.*, **2003**, *118*, 4198-4205.

[92] Mavrikakis, M.; Stoltze, P.; Norskov, J. K.; *Catal. Lett.*, **2000**, *64*, 101-106.

[93] Starr, D. E.; Campbell, C. T.; *J. Am. Chem. Soc.*, **2008**, *130*, 7321-7327.

[94] Stuckless, J. T.; Starr, D. E.; Bald, D. J.; Campbell, C. T.; *Phys. Rev. Lett.*, **1997**, *56*, 13496-13502.

[95] Xu, R.; Wang, D.; Zhang, J.; Li, Y.; *Chem. Asian J.*, **2006**, *1*, 888-893.

[96] Narayanan, R.; El-Sayed, M. A.; *J. Phys. Chem. B*, **2004**, *108*, 5726-5733.

[97] Narayanan, R.; El-Sayed, M. A.; *Nano Lett.*, **2004**, *4*, 1343-1348.

[98] Komanicky, V.; Iddir, H.; Chang, K. C.; Menzel, A.; Karapetrov, G.; Hennessy, D.; Zapol, P.; You, H.; *J. Am. Chem. Soc.*, **2009**, *131*, 5732.

[99] *"Phenomenology of Magnetism at the Macroscopic Scale"*, Gignoux, D.; **2005**, Springer: New York, NY, USA.

[100] Indira, T. K.; Lakshmi, P. K.; *International Journal of Pharmaceutical Sciences and Nanotechnology*, **2010**, *3*, Issue 3, 1035-1042.

[101] *"Magnetic Nanoparticles: A Review of Chemical and Physical Characteristics Important in Medical Applications"*, Yadollahpour, A.; Rashidi, *Oriental Journal of Chemistry*, Vol. 31, Special Issue, doi: http://dx.doi.org/10.13005/ojc/31.Special-Issue1.03

[102] Kolhatkar, A. G.; Jamison, A. C.; Litvinov, D.; Willson, R. C.; Lee, T. R.; *Int. J. Mol. Sci.*, **2013**, *14*, 15977-16009.

[103] Gubin, S. P.; Koksharov, Y. A.; Khomutov, G. B.; Yurkov, G. Y.; *Russ. Chem. Rev.*, **2005**, *74*, 489–520.

[104] Issa, B.; Obaidat, I. M.; Albiss, B. A.; Haik, Y.; *Int. J. Mol. Sci.*, **2013**, *14*, 21266-21305

[105] Frenkel, J.; Doefman, J.; *Nature*, **1930**, *126*, 274–275.

[106] Gonser, U.; Krischel, K.; Nasu, S.; *J. Magn. Magn. Mater.*,1980, *15-18*, 1145-1146.

[107] Bean, C. P.; Livingston, J. D.; *Superparamagnetism. J. Appl. Phys.*, **1959**, *30*, 120S–129S.

[108] Akbarzadeh, A.; Samiei, M.; Davaran, S.; *Nanoscale Res Lett.*, **2012**; *7*(1), 144.

[109] Supramolecular chemistry: defined, Wang, M.-X.; *Supramolecular Chemistry*, **2016,** *Vol. 28*, Nos. 1–2, 1–3, http://dx.doi.org/10.1080/10610278.2015.1059021.

[110] "Supramolecular Chemistry", Lehn, J.-M.; **1995,** WILEY-VCH Verlag GmbH, Weinheim.

[111] Whitesides, G. M.; Grzybowski, B.; *Science*, **2002**, *295*, 2418–2421.

[112] *"Supramolecular Chemistry: From Molecules to Nanomaterials"*, ed.: Gale, P.; J. Steed, J., **2012**, Wiley-VCH Verlag GmbH & Co. KGaA, Weinheim.

[113] Tiwari, J. N., Tiwari, R. N.; Kim, K. S.; *Progress in Materials Science*, **2012**, *57*, 724–803.

[114] *"Self-Assembly and Nanotechnology: A Force Balance Approach"*, Lee, Y. S., **2008**, John Wiley and Sons, Inc.

[115] *"Self- Assembly and Nanostructured Materials"*, Whitesides, G. M.; Kriebel, J. K.; Mayers, B. T., Chapter 9

[116] Cademartiri, L.; Bishop, K. J. M.; *Nature Materials*, **2015**, *14*, 2–9.

[117] Biancaniello, P.; Kim, A.; Crocker, J.; *Phys. Rev. Lett.*, **2005**, *94*, 58302:1-4.

[118] Jones, M. R.; Macfarlane, R. J.; Lee, B.; Zhang, J.; Young, K. L.; Andrew J. Senesi, A. J.; Mirkin, C. A.; *Nature Mater.*, **2010**, *9*, 913–917.

[119] Robert J. Macfarlane, R. J.; Lee, B.; Jones, M. R.; Nadine Harris, N.; Schatz, G. C.; Mirkin, C. A.; *Science*, **2011**, *334*, 204–208.

[120] Nykypanchuk, D.; Maye, M. M.; van der Lelie, D.; Gang, O.; *Nature*, **2008**, *451*, 549–552.

[121] Park, S. Y.; Lytton-Jean, A. K. R.; Lee, B.; Weigand, S.; Schatz, G. C.; Mirkin, C. A.; *Nature*, **2008**, *451*, 553–556.

[122] Shevchenko, E. V.; Talapin, D. V.; Kotov, N. A.; O'Brien, S.; Murray, C. B.; *Nature*, **2006**, *439*, 55–59.

[123] Leunissen, M. E.; Christova1, C. G.; Hynninen, A.-P.; Royall, C. P.; Campbell, A. I.; Imhof, A.; Dijkstra1, M.; van Roij, R.; van Blaaderen, A.; *Nature*, **2005**, *437*, 235–240.

[124] Nie, Z.; Fava, D.; Kumacheva, E.; Zou, S.; Walker, G. C.; Rubinstein, M.; *Nature Mater.*, **2007**, *6*, 609–614.

[125] Supramolecular self-assemblies as functional nanomaterials, Eric Busseron, Yves Ruff, Emilie Moulin and Nicolas Giuseppone, Nanoscale, 2013, 5, 7098-7140.

[126] Grzelczak, M.; Vermant, J.; Furst, E. M.; Liz-Marza´n, L. M.; *ACS Nano*, **2010**, *4* (7), 3591–3605.

[127] Tang, Z. Y.; Zhang, Z. L.; Wang, Y.; Glotzer, S. C.; Kotov, N. A.; *Science,* **2006**, *314*, 274–278.

[128] Wang, H.; Lin, W.; Fritz, K. P.; Scholes, G. D.; Winnik, M. A.; Manners, I; *J. Am. Chem. Soc.*, **2007**, *129*, 12924–12925.

[129] Aldaye, F. A.; Palmer, A. L.; Sleiman, H. F.; *Science*, **2008**, *321*, 1795–1799.

[130] Correa-Duarte, M. A.; Perez-Juste, J.; Sanchez-Iglesias, A.; Giersig, M.; Liz-Marzan, L. M.; *Angew. Chem. Int. Ed.*, **2005**, *44*, 4375–4378.

[131] Courty, A., Mermet, A., Albouy, P. A., Duval, E. & Pileni, M. P. Vibrational coherence of self-organized silver nanocrystals in fcc supra-crystals. Nature Mater. 4, 395–398 (2005).

[132] Collier, C. P.; Saykally, R. J.; Shiang, J. J.; Henrichs, S. E.; Heath, J. R.; *Science,* **1997**, *277*, 1978–1981.

[133] Detrich, A.; Deák, A.; Hild, E.; Kovács, A. L.; Hórvölgyi, Z.; *Langmuir*, **2010**, *26* (4), 2694–2699.

[134] Rabani, E.; Reichman, D. R.; Geissler, P. L.; Brus, L. E.; *Nature*, **2003**, *426*, 271-274.

[135] Lin, Y.; Bo¨ker, A.; Skaff, H.; Cookson, D.; Dinsmore, A. D.; Emrick, T.; Russell, T. P.; *Langmuir*, **2005**, *21*, 191-194.

[136] Schwenke, K.; Isa, L.; Del Gado, E.; *Langmuir*, **2014**, *30*, 3069−3074.

[137] Pieranski, P.; *Phys. Rev. Lett.*, **1980**, *45*, 569-572.

[138] Boker, A.; He, J.; Emrick, T.; Russell, T. P.; *Soft Mater*, **2007**, *3*, 1231-1248.

[139] Binks, B. P.; Lumsdon, S. O.; *Langmuir*, **2000**, *16*, 8622–8631.

[140] Duan, H.; Wang, D.; Kurth, D. G.; Mohwald, H.; *Angew. Chem. Int. Ed*,. **2004**, *43*, 5639 –5642.

[141] Reincke, F.; Hickey, S. G.; Kegel, W. K.; Vanmaekelbergh, D.; *Angew. Chem. Int. Ed.*, **2004**, *43*, 458 – 462.

[142] Hermanson, K. D.; Lumsdon, S. O.; Williams, J. P.; Kaler, E. W.; Velev, O. D.; *Science*, **2001**, *294*, 1082–1086.

[143] Korth, B. D.; Keng, P.; Shim, I.; Bowles, S. E.; Tang, C.; Kowalewski, T.; Nebesny, K. W.; Pyun, J.; *J. Am.Chem. Soc.*, **2006**, *128*, 6562–6563.

[144] Klajn, R.; Bishop, K. J. M.; Grzybowski, B. A.; *Proc. Natl Acad. Sci. USA*, **2007**, *104*, 10305–10309.

[145] Zhihong Nie, Z.; alla Petukhova, A.; and eugenia Kumacheva, E.; *Nature Nanotechnology*, **2010**, Vol 5 , January, 15-25.

[146] Lu, Z.; Yadong Yin, Y.; *Chem. Soc. Rev.*, **2012**, *41*, 6874–6887.

[147] Pileni, M.-P.; *Acc. Chem. Res.*, **2007**, *40* (8), 685–693.

[148] Chen, C.-L.; Zhang, P.; Rosi, N. L.; *J. Am. Chem. Soc.*, **2008**, *130*, 13555-13557.

[149] Chapter 1 One-dimensional nanostructures: An introduction

[150] Zhai, T. Y.; Li, L.; Ma, Y.; Liao, M. Y.; Wang, X.; Fang, X. S.; Yao, J. N.; Bando, Y.; Golberg, D.; *Chem. Soc. Rev.*, **2011**, *40*, 2986–3004.

[151] Liang, H. W.; Liu, S.; Yu, S. H.; *Adv. Mater.*, **2010**, *22*, 3925–3937.

[152] Zhang, Z.; Sun, X.; Dresselhaus, M. S.; Ying, J. Y.; *Phys. Rev. B*, **2000**, *61*, 4850-4861.

[153] Holmes, J. D.; Johnston, K. P.; Doty, R. C.; Korgel, B. A;. *Science*, **2000**, 287, 1471-1473.

[154] Lu, X.; Hanrath, T.; Johnston, K. P.; Korgel, B. A.; *Nano Lett.*, **2003**, *3*, 93-99.

[155] Rodrigues, V.; Bettini, J.; Silva, P. C.; Ugarte, D.; *Phys. Rev. Lett.*, **2003**, *91*, 096801:1-4.

[156] Gambardella, P.; Rusponi, S.; Veronese, M.; Dhesi, S. S.; Grazioli, C.; Dallmeyer, A.; Cabria, I.; Zeller, R.; Dederichs, P. H.; Kern, K.; Carbone, C.; Brune, H.; *Science,* **2003**, *300*, 1130-1133.

[157] Romo-Herrera, J. M.; Terrones, M.; Terrones, H.; Dag, S.; Meunier, V.; *Nano Lett.*, **2007**, *7* (3), 570–576.

[158] Jiang, L.; Dong, H. L.; Hu, W. P.; *Soft Matter*, **2011**, *7*, 1615–1630.

[159] Xiang, J.; Lu, W.; Hu, Y. J.; Wu, Y.; Yan, H.; Lieber, C. M.; *Nature*, **2006**, *441*, 489–493.

[160] Qian, F.; Gradecak, S.; Li, Y.; Wen C. Y.; Lieber, C. M.; *Nano Lett.*, **2005**, *5*, 2287–2291.

[161] Law, M.; Greene, L. E.; Johnson, J. C.; Saykally, R.; Yang, P. D.; *Nat. Mater.*, **2005**, *4*, 455–459.

[162] McAlpine, M. C.; Ahmad, H.; Wang, D. W.; Heath, J. R.; *Nat. Mater.*, **2007**, *6*, 379–384.

[163] Vickery, J. L.; Patil, A. J.; Mann, S.; *Adv. Mater.*, **2009**, *21*, 2180–2184.

[164] Someya, T.; Sekitani, T.; Iba, S.; Kato, Y.; Kawaguchi, H.; Sakurai, T.; *Proc. Natl. Acad. Sci. U. S. A.*, **2004**, *101*, 9966−9970.

[165] Wang, C.; Hwang, D.; Yu, Z.; Takei, K.; Park, J.; Chen, T.; Ma, B.; Javey, A.; *Nat. Mater.*, **2013**, *12*, 899−904.

[166] Shipway, A. N.; Katz, E.; Willner, I.; *ChemPhysChem*, **2000**,*1*,18-52.

[167] Guo, Q.; Xu, M.; Yuan, Y.; Gu, R.; Yao, J.; *Langmuir* **2016**, *32*, 4530−4537.

[168] Wang, Y.; Kanjanaboos, P.; McBride, S. P.; Barry, E.; Lin, X.-M.; Jaeger, H. M.; *Faraday Discuss.*, **2015**, *181*, 325–338.

[169] Knight, M. W.; Wu, Y.; Britt Lassiter, J.; Nordlander, P.; Halas, N. J.; *Nano Lett.*, **2009**, *9* (5), 2188–2192.

[170] Iler, R. K. J.; *Colloid Interface Sci.*, **1966**, *21*, 569-594.

[171] Wang, Y.; Duan, C.; Peng, L.; Liao, J.; *Scientific Reports*, **2014**, *4*, 7565:1-6.

[172] Black, C. T.; Murray, C. B.; Sandstrom, R. L.; Sun, S.; *Science,* **2000**, *290*, 1131−1134.

[173] Majetich, S. A.; Wen, T.; Booth, R. A.; *ACS Nano,* **2011**, *5*, 6081−6084.

[174] Lou, Y.; Maye, M. M.; Han, L.; Luo, J.; Zhong, C. J.; *Chem. Commun.,* **2001**, 473−474.

[175] Puntes, V. F.; Gorostiza, P.; Aruguete, D. M.; Bastus, N. G.; Alivisatos, A. P.; *Nat. Mater.,* **2004**, *3*, 263−268.

[176] Heath, J. R.; Knobler, C. M.; Leff, D. V.; *J. Phys. Chem. B,* **1997**, *101*, 189−197.

[177] Pileni, M. P.; *Appl. Surf. Sci.,* **2001**, *171*, 1−14.

[178] Schlicke, H.; Battista, D.; Kunze, S.; Schröter, C. J.; Eich, M.; Vossmeyer, T.; *ACS Appl. Mater. Interfaces,* **2015**, *7*, 15123−15128.

[179] Schlicke, H.; Leib, E. W.; Petrov, A.; Schröder, J. H.; Vossmeyer, T.; *J. Phys. Chem. C,* **2014**, *118*, 4386−4395.

[180] Chen, S.; *Anal. Chim. Acta,* **2003**, *496*, 29−37.

[181] Zhang, L.; *Appl. Surf. Sci.,* **2013**, *270*, 292− 294.

[182] Bigioni, T. P.; Lin, X.-M.; Nguyen, T. T.; Corwin, E. I.; Witten, T. A.; Jaeger, H. M.; *Nat. Mater.,* **2006**, *5*, 265−270.

[183] Wen, T.; Majetich, S. A.; *ACS Nano*, **2011**, *5*, 8868−8876.

[184] Chen, M.-C.; Yang, Y.-L.; Chen, S.-W.; Li, J.-H.; Aklilu, M.; Tai, Y.; *ACS Appl. Mater. Interfaces*, **2013**, *5*, 511−517.

[185] Yi, L.; Jiao, W.; Wu, K.; Qian, L.; Yu, X.; Xia, Q.; Mao, K.; Yuan, S.; Wang, S.; Jiang, Y.; *Nano Res.,* **2015**, *8*, 2978−2987.

[186] Jeong, S.; Hu, L.; Lee, H. R.; Garnett, E.; Choi, J. W.; Cui, Y.; *Nano Lett.,* **2010**, *10*, 2989−2994.

[187] Pang, J.; Xiong, S.; Jaeckel, F.; Sun, Z.; Dunphy, D.; Brinker, C. J.; *J. Am. Chem. Soc.*, **2008**, *130*, 3284−3285.

[188] Pradhan, S.; Ghosh, D.; Xu, L.-P.; Chen, S.; *J. Am. Chem. Soc.*, **2007**, *129*, 10622−10623.

[189] Huda, S.; Smoukov, S. K.; Nakanishi, H.; Kowalczyk, B.; Bishop, K.; Grzybowski, B. A.; *ACS Appl. Mater. Interfaces*, **2010**, *2*, 1206−1210.

[190] Mueggenburg, K. E.; Lin, X.-M.; Goldsmith, R. H.; Jaeger, H. M.; *Nat. Mater.*, **2007**, *6*, 656−660.

[191] He, J.; Kanjanaboos, P.; Frazer, N. L.; Weis, A.; Lin, X.-M.; Jaeger, H. M.; *Small*, **2010**, *6*, 1449−1456.

[192] Lee, J.; Bhak, G.; Lee, J.-H.; Park, W.; Lee, M.; Lee, D.; Jeon, N. L.; Jeong, D. H.; Char, K.; Paik, S. R.; *Angew. Chem., Int. Ed.*, **2015**, *54*, 4571−4576.

[193] Jeong, Y.; Chen, Y.-C.; Turksoy, M. K.; Rana, S.; Tonga, G. Y.; Creran, B.; Sanyal, A.; Crosby, A. J.; Rotello, V. M.; *Adv. Mater.*, **2014**, *26*, 5056−5061.

[194] Cheng, W. L.; Campolongo, M. J.; Cha, J. J.; Tan, S. J.; Umbach, C. C.; Muller, D. A.; Luo, D.; *Nat. Mater.*, **2009**, *8*, 519−525.

[195] Xia, H.; Wang, D.; *Adv. Mater.*, **2008**, *20*, 4253−4256.

[196] Craighead, H. G.; *Science*, **2000**, *290*, 1532−1535.

[197] Lin, Y.; Skaff, H.; Böker, A.; Dinsmore, A. D.; Emrick, T.; Russell, T. P.; *J. Am. Chem. Soc.*, **2003**, *125*, 12690−12691.

[198] Sanders, T. A., II; Sauceda, M. N.; Dahl, J. A. Langmuir isotherms of flexible, covalently crosslinked gold nanoparticle networks: Increased collapse pressures of membrane-like structures. Mater. Lett. 2014, 120, 159−162.

[199] Andryszewski, T., Iwan, M., Hołdyński, M., Fiałkowski, M. Chem. Mater. 2016, 28 (15), 5304–5313.

[200] *"Emulsion Formation, Stability, and Rheology*", Tadros, T. F.; **2013**, Wiley- VCH Verlag: Berlin, Germany.

[201] Lin, Y.; Skaff, H.; Emrick, T.; Dinsmore, A. D.; Russell, T. P.; *Science*, **2003**, *299*, 226−229.

[202] Stancik, E. J.; Fuller, G. G.; *Langmuir*, **2004**, *20*, 4805−4808.

[203] Wang, D.; Duan, H.; Mohwald, H.; *Soft Matter*, **2005**, *1*, 412−416.

[204] Reincke, F.; Kegel, W. K.; Zhang, H.; Nolte, M.; Wang, D.; Vanmaekelbergh, D.; Mohwald, H. Understanding the self-assembly of charged nanoparticles at the water/oil interface. Phys. Chem. Chem. Phys. 2006, 8, 3828−3835.

[205] Du, K.; Knutson, C. R.; Glogowski, E.; McCarthy, K. D.; Shenhar, R.; Rotello, V. M.; Tuominen, M. T.; Emrick, T.; Russell, T. P.; Dinsmore, A. D.; *Small*, **2009,** *5*, 1974−1977.

[206] Van Gough, D.; Juhl, A. T.; Braun, P. V.; *Materials today*, **2009**, *12* (6), 28-35.

[207] *"Electromagnetic Mixing Formulas and Applications",* Sihvola, A.; IEEE Electromagnetic Wave Series, IEEE Pub., London, UK, **1999**, vol. 47.

[208] Min, K. D.; Kim, M. Y. Choi, K. Y.; Lee, J. H.; Lee, S. G.; *Polym. Bull.*, **2006**, *57*, 101–108.

[209] Wang, H.; Xu, P.; Zhong, W.; Shen, L.; Du, Q.; *Polym. Degrad. Stab.*, **2005**, *87*, 319–327.

[210] Su, S. J.; Kuramoto, N.; *Synth. Met.*, **2000**, *114*, 147–153.

[211] Taurozzi, J. S.; Arul, H.; Bosak, V. Z.; Burban, A. F.; Voice, T. C.; Bruening, M. L.; Tarabara, V. V.; *J. Membr. Sci.*, **2008**, *325*, 58–68.

[212] Kim, J.; van der Bruggen, B.; *Environ. Pollut.*, **2010**, *158*, 2335–2349.

[213] Lu, C. L.; Yang, B.; *J. Mater. Chem.*, **2009**, *19*, 2884–2901.

[214] El-Sayed, M. A.; *Acc. Chem. Res.*, **2001**, *34*(4), 257–264.

[215] El-Sayed, M. A.; *Acc. Chem. Res.*, **2004**, *37*, 326–333.

[216] Jin, R.; Sun, S.; Yang, Y.; Xing, Y.; Yu, D.; Yu X.; Song, S.; *Dalton Trans.*, **2013**, 7888–7893.

[217] Zhou, X.; Xu, W.; Liu, G.; Panda, D.; Chen, P.; *J. Am. Chem. Soc.*, **2010**, *132*, 138–146.

[218] Li, X.; Wang, L.; Fan, Y.; Feng, Q.; Cui, F. Z.; *J. Nanomater.*, **2012**, *2012*, 548389:1-19.

[219] Reijnders, L.; *Polym. Degrad. Stab.*, **2009**, *94*, 873–876.

[220] Travan, A.; Pelillo, C.; Donati, I.; Marsich, E.; Benincasa, M.; Scarpa, T.; Semeraro, S.; Turco, G.; Gennaro, R.; S. Paoletti, S.; *Biomacromolecules*, **2009**, *10*, 1429–1435.

[221] Kulthong, K.; Srisung, S.; Boonpavanitchakul, K.; Kangwansupamonkon, W.; R. Maniratanachote, R.; *Part. Fibre Toxicol.*, **2010**, *7*, 8:1-9.

[222] Agnihotri, S.; Mukherji, S.; Mukherji, S.; *Nanoscale*, **2013**, *5*, 7328-7340.

[223] Karnik, B. S.; Davies, S. H.; Bauman, M. J.; Masten, S. J.; *Environ. Sci. Technol.*, **2005**, *39*(19), 7656–7661.

[224] Choi, W. I.; Kim, J. Y.; Heo, S. U.; Jeong, Y. Y.; Kim, Y. H.; Tae, G.; *J. Controlled Release*, **2012**, *162*, 267–275.

[225] *"Major Accomplishments in Composite Materials and Sandwich Structures"*, Daniel, I. M.; Gdoutos, E. F.; Rajapakse, Y. D. S.; **2009**, Springer Science & Bussiness Media.

[226] Luo, H.; Gersappe, D.; *Macromolecules*, **2004**, *37*, 5792– 5799.

[227] Ghosh, A.; Patra, C. R.; Mukherjee, P; Sastry, M.; Kumar, R.; *Microporous Mesoporous Mater.*, **2003**, *58*, 201–211.

[228] Roth, P. J.; Theato, P.; *Macromol. Chem. Phys.*, **2012**, *213*, 2550–2556.

[229] Kickelbick, G.; *Prog. Polym. Sci.*, **2003**, *28*, 83–114.

[230] Kim, Y. J.; Kim, J.-H.; Ha, S. W.; Kwon, D.; Lee, J.-K.; *RSC Adv.*, **2014**, *4*, 43371–43377.

[231] Heo, K.; Miesch, C.; Emrick, T.; Hayward, R. C.; *Nano Lett.*, **2013**, *13*, 5297–5302.

[232] Lou, M. J.; Zhao, J. Q.; Tang, W.; Pu, C. S.; *Appl. Surf. Sci.*, **2005**, *249*, 76–84.

[233] Kwak, S. Y.; Kim, S. H.; Kim, S. S,; *Environ. Sci. Technol.*, **2001**, *35*(11), 2388–2394.

[234] Kim, Y. J.; Kim, J.-H.; Ha, S.-W.; Kwon, D.; Lee, J.-K.; *RSC Adv.*, **2014,** *4*, 43371–43377.

[235] Kuo, P. L.; Chen, W. F.; *J. Phys. Chem. B*, **2003**, *107*, 11267– 11272.

[236] Kodama, R. H.; *Journal of Magnetism and Magnetic Materials*,**1999**, *200*, 359-372.

[237] Huang, X.; Tan, C.; Yin, Z.; Zhang, H.; *Adv. Mater.*, **2014**, *26*, 2185–2204.

[238] Shehzad, K.; Xu, Y.; Gaoc, C.; Duanb, X.; *Chem. Soc. Rev.*, **2016**, *45*, 5541-5588.

[239] Su, K.-H.; Wei, Q.-H.; Zhang, X.; *Nano Letters*, **2003**, *3* (8), 1087–1090.

[240] Scheeler, S. P.; Rockstuhl, S. M. C.; Bin Hasan, S.; Ullrich, S.; Neubrech, F.; Kudera, S.; Pacholski, C.; *J. Phys. Chem. C*, **2013**, *117* (36), 18634–18641.

[241] Chen, T.; Pourmand, M.; Feizpour, A.; Cushman, B.; Reinhard, B. M.; *J. Phys. Chem. Lett.*, **2013**, *4* (13), 2147–2152.

[242] Jain, P. K.; Eustis, S.; El-Sayed, M. A.; J. Phys. Chem. B, 2006, 110 (37), pp 18243–18253.

[243] Koole, R.; Liljeroth, P.; Donega, C. D.; Vanmaekelbergh, D.; Meijerink, A.; *J. Am. Chem. Soc.*, **2006**, *128*, 10436–10441.

[244] Chen, N.-T.; Cheng, S.-H.; Liu, C.-P.: Souris, J. S.; Chen, S.-T.; Mou, C.-Y.; Lo, L.-W.; *Int. J. Mol. Sci.*, **2012**, *13*, 16598-16623.

[245] Boisselier, E.; Astruc, D.; *Chem. Soc. Rev.*, **2009**, *38*, 1759–1782.

[246] Zaitseva, N.; Dai, Z. R.; Leon, F. R.;Krol, D.; *J. Am. Chem. Soc.*, **2005**, *127* (29), 10221–10226.

[247] Crooker, S. A.; Hollingsworth, J. A.; Tretiak, S.; Klimov, V. I.; *Phys. Rev. Lett.*, 2002, *89*, 186802:1-4.

[248] Kagan, C. R.; Murray, C. B.; Bawendi, M. G.; *Phys. Rev. B*, **1996**, *54*, 8633-8643.

[249] Lalatonne, Y.; Motte, L.; Russier, V.; Ngo, A. T.; Bonville, P.; Pileni, M. P.; *J. Phys. Chem. B*, **2004**, *108* (6), 1848–1854.

[250] Russier, V.; Petit, C.; Pileni, M. P.; *Journal of Applied Physics*, **2003**, *93*, 10001.

[251] Govorov, A. O.; Bryant, G. W.; Zhang, W.; Skeini, T.; Lee, J.; Kotov, N. A.; Slocik, J. M.; Naik, R. R.; *Nano Lett.*, **2006**, *6*, No. 5, 984-994.

[252] Darbeau, R. W.; *Applied Spectroscopy Reviews*, **2006**, *41*: 401–425.

[253] Hollas, J. M.; "High Resolution Spectroscopy. 2. Electromagnetic radiation and its interaction with atoms and molecules", **2013**, Butterworth-Heinemann.

[254] "UV-VIS Spectroscopy and Its Applications", Heinz-Helmut Perkampus, H.-H.; Springer -Ver lag Berlin Heidelberg New York London Paris Tokyo Hong Kong Barcelona Budapest

[255] *"Basic Concepts of Analytical Chemistry",* Khopkar, S. M.; **1998**, New Age International.

[256] Haiss, W.; Thanh, N. T. K.; Aveyard, J.; Fernig, D. G.; *Anal. Chem.*, **2007**, *79*, 4215-4221.

[257] *"Infrared and Raman Spectroscopy: Principles and Spectral Interpretation",* Peter Larkin, **2011**, Elsevier.

[258] *"Advanced Physical Chemistry",* Raj, G.; **1978**, Krishna Prakashan Media.

[259] *"Transmission Electron Microscopy. A Textbook for Materials Science",* Williams, D. B.; Carter, C. B.; **1996**, Springer Science + Business Media, LLC, New York.

[260] *"Janqeira's Basic Histology, thirteenth edition",* Mescher, A. L.; **2013**, The McGraw-Hill Companies, China

[261] Scanning Transmission Electron Microscopy for Nanostructure Characterization, S. J. Pennycook, A. R. Lupini, M. Varela, A. Y. Borisevich,, Y. Peng, M. P. Oxley, K. van Benthem, M. F. Chisholm

[262] "Practical Scanning Electron Microscopy: Electron and Ion Microprobe Analysis", Goldstein, J.; **2012**, Springer Science & Business Media.

[263] *"Handbook of Charged Particle Optics",* Orloff, J.; **1997**, CRC Press.

[264] *"Scanning Electron Microscopy and X-Ray Microanalysis: A Text for Biologists, Materials Scientists, and Geologists",* Goldstein, J.; Newbury, D. E.; Echlin, P.; Joy, D. C.; Romig Jr., Charles E. Lyman, A. D.; Fiori, C.; Lifshin, E.; **2012**, Springer Science & Business Media.

[265] Islam, A. W.; Kabadi, V. N.; *Chemical and Process Engineering*, **2011**, *32* (2), 101-115.

[266] Fernandes, D.; Conway, W.; Wang, X.; Burns, R.; Lawrance, G.; Maeder, M.; Puxty, G.; *J. Chem. Thermodyn.*, **2012**, *51*, 97−102.

[267] Kalescky, R. J. B.; Shinoda, W.; Moore, P. B.; Nielsen, S. O.; *Langmuir*, **2009**, *25*, 1352−1359.

[268] Du, K.; Glogowski, E.; Emrick, T.; Russell, T. P.; Dinsmore, A. D.; *Langmuir*, **2010**, *26*, 12518−12522.

[269] Fan, H.; Striolo, A.; *Phys. Rev. E*, **2012**, *86*, 051610:1-11.

[270] Jiang, S.; Granick, S.; *J. Chem. Phys.*, **2007**, *127*, 161102:1-4.

[271] Cheung, D. L.; Bon, S. A. F.; *Phys. Rev. Lett.;* **2009**, *102*, 066103:1-4.

[272] Cheung, D. L.; Bon, S. A. F.; *Soft Matter*, **2009**, *5*, 3969−3976.

[273] Sashuk, V.; Hołyst, R.; Wojciechowski, T.; Górecka, E.; Fiałkowski, M.; *Chem. - Eur. J.*, **2012**, *18*, 2235−2238.

[274] Sashuk, V.; Hołyst, R.; Wojciechowski, T.; Fiałkowski, M.; *J. Colloid Interface Sci.*, **2012**, *375*, 180−186.

[275] Andala, D. M.; Shin, S. H. R.; Lee, H. Y.; Bishop, K. J. M.; *ACS Nano*, **2012**, *6*, 1044−1050.

[276] Smoukov, S. K.; Gangwal, S.; Marquez, M.; Velev, O. D. Reconfigurable responsive structures assembled from magnetic Janus particles. Soft Matter 2009, 5, 1285−1292.

[277] Fernandez-Rodriguez, M. A.; Song, Y.; Rodríguez-Valverde, M. Á.; Chen, S.; Cabrerizo-Vilchez, M. A.; Hidalgo-Alvarez, R.; *Langmuir*, **2014**, *30*, 1799−1804.

[278] Xu, L.; Han, G.; Hu, J.; He, Y.; Pan, J.; Li, Y.; Xiang, J.; *Phys. Chem. Chem. Phys.*, **2009**, *11*, 6490−6497.

[279] Iwan, M.; Andryszewski, T.; Wydryszek, M.; Fialkowski, M.; *RSC Adv.*, **2015**, *5*, 70127− 70138.

[280] "pKa Prediction for Organic Acids and Bases", Perrin, D. D.; Dempsey, B.; Serjeant, E. P.; 1981, Chapman & Hall: London.

[281] *"The chemistry of amides",* Zabicky, J.; **1970**, John Wiley & Sons: London.

[282] Wang, Y.; Kanjanaboos, P.; Barry, E.; Mcbride, S.; Lin, X.-M.; Jaeger, H. M.; *Nano Lett.*, **2014**, *14*, 826−830.

[283] Lin, X. M.; Parthasarathy, R.; Jaeger, H. M.; *Appl. Phys. Lett.*, **2001**, *78*, 1915−1917.

[284] Dong, A.; Chen, J.; Vora, P. M.; Kikkawa, J. M.; Murray, C. B.; *Nature*, **2010**, *466*, 474−477.

[285] Ng, K. C.; Udagedara, I. B.; Rukhlenko, I. D.; Chen, Y.; Tang, Y.; Premaratne, M.; Cheng, W.; *ACS Nano*, **2012**, *6*, 925−934.

[286] *"Infrared and Raman characteristic Group Frequencies: tables and charts",* Socrates, G.; **2004**, John & Sons.

[287] *"Introduction to Organic Spectroscopy",* Lambert, J. B.; 1987, Macmillan.

[288] Chiellini, E.; Corti, A.; D'Antone, S.; Solaro, R.; *Prog. Polym. Sci.*, **2003**, *28*, 963–1014.

[289] Kulp, K.; Lorenz, K.; *Cereal Chem.*, **1980**, *58*(1), 46–48.

[290] Xia, B.; Cui, Q.; He, F.; Li, L.; *Langmuir*, **2012**, *28*, 11188–11194.

[291] *"The Thermodynamic Machinery of Life"*, Kurzynski, M.; **2006**, Springer Science & Business Media.

[292] Flegmann, A. W.; Tattersall, R. J.; *Mol. Evol.*, **1979**, *12*, 349– 355.

[293] Montalbetti, C. A. G. N.; Falque, V.; Tetrahedron, **2005**, *61*, 10827-10852.

[294] Ulijn, R. V.; Moore, B. D.; Janssen, A. E. M.; Halling, P. J.; *J. Chem. Soc., Perkin Trans. 2*, **2002**, *2*, 1024–1028.

[295] Valeur, E.; Bradley, M.; *Chem. Soc. Rev.*, **2009**, *38*, 606–631.

[296] Jursic, B. S.; Zdravkovski, Z.; *Synth. Commun.*, **1993**, *23*, 2761–2770.

[297] *"March's advanced organic chemistry. Reactions, mechanism, and structure"*, Smith, M. B.; March, J.; **2007**, John Wiley & Sons, Inc.

[298] *"Chemia Organiczna"*, R. T. Morrison, R. T.; and R. N. Boyd, R. N.; **2009**, Wydawnictwo naukowe PWN, Warszawa, 2009.

[299] Marochkin, I. I.; Dorofeeva, O. V.; *Comput. Theor. Chem.*, **2012**, *991*, 182–191.

[300] *"Comprehensive Handbook of Chemical Bond Energies"*, Luo, Y. R.; **2007**, CRC Press, Boca Raton, Florida.

[301] Kalindjian, S. B.; Dunstone, D. J.; Low, C. M. R.; Pether, M. J.; Roberts, S. P.; Tozer, M. J.; Watt, G. F.; Shankley, N. P.; *J. Med. Chem.*, **2001**, *44*(8), 1125–1133.

[302] Wang, D.; Nap, R. J.; Lagzi, I.; Kowalczyk, B.; Han, S.; Grzybowski, B. A.; Szleifer, I.; *J. Am. Chem. Soc.*, **2011**, *133*, 2192–2197.